UNIVERSITY OF TRENTO

Doctoral School in Civil, Environmental and Mechanical Engineering

Curriculum 3. Modelling and Simulation

Joel Christopher Harrop

Dynamic Instabilities in Structures with Nonholonomic Constraints

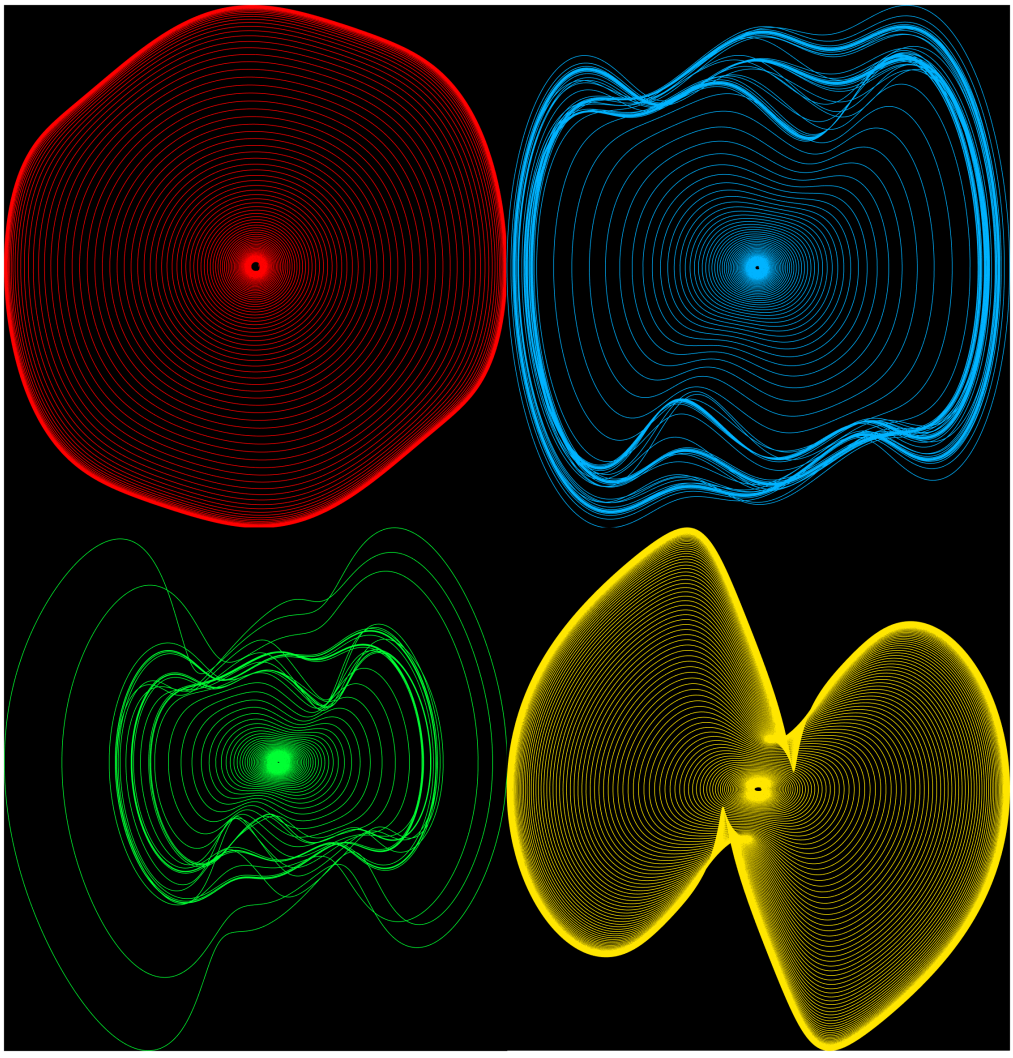

2026 - Doctoral thesis

UNIVERSITY OF TRENTO

Doctoral School in Civil, Environmental and Mechanical Engineering – Modelling and Simulation
XXXVIII cycle 2022/2025

Joel Christopher Harrop

Dynamic Instabilities in Structures with Nonholonomic Constraints

Advisors:

Prof. Davide Bigoni	University of Trento
Prof. Alfio Grillo	Politecnico di Torino
Prof. Andrea Piccolroaz	University of Trento

Trento April 2026

University of Trento
Doctoral School in Civil, Environmental and Mechanical Engineering
http://web.unitn.it/en/dricam
Via Mesiano 77, I-38123 Trento
Tel. +39 0461 282670 / 2611 - *dicamphd@unitn.it*

"Not all treasure is silver and gold, mate."

— Jack Sparrow, Pirates of the Caribbean

Acknowledgments

They say it takes an army to raise a child. In this instance, I believe it has taken an army to raise this PhD student. Being from the Isle of Man, instilled in me is a sense of community. I believe that the community which has formed around me in these recent years has turned into more of an army, without whom I wouldn't be where I am today.

To this end, I must acknowledge my academic army. Davide, Alfio, Andrea, Ozgur, Sasha and Natasha, all who believed in me when I needed it the most, and making lifelong friends in the process.

To my family army. Mother, Father, Lynne, Adrian, Nana and Grandad. My two amazing sisters, their husbands, and wonderful children. You have all supported me in the silly and serious things. From the first instances of going to university, to washing my clothes, to suffering through reading my CV and work, and for giving me a reason to come back home. Thank you.

To my Mesiano army and Cycle 38, It's not easy to remain sane working in a former sanatorium for three years. Without the many coffee breaks, terrace beers, and each other's company, I, for one, wouldn't have made it this far. I look forward to seeing where life takes us all. A special mention must be made to Andrea for his excellent real estate expertise (job number two), and for always going out of his way to see everyone succeed. See you in Palermo for round two.

To my Italian army (Honorary Britalian and AC4), thank you for embracing me. Teaching me to make ragu, how to be passionate (and patient when you always lose in the rugby, UNTIL NOW FORZA GLI AZZURRI), and bringing lakes, mountains, and mountains of Forst into my life. My time in AC4 with you all was a blast. Our time in Scaltetta, Flambards, and Acca a struggle. But nothing i would trade for the world, and i hope to bring a little bit of Italy wherever i go in life.

To my Iranian army. From the day I stepped foot in Italy and met Soroush (my dear friend and very tolerant flatmate). I have had the pleasure to meet and even live with people I never thought would be possible. Enjoying different cultures, food and expanding my limited knowledge of wines. I am very much looking forward to joining you all back home eating Kabab koobideh, and Persian rice with Tahdig.

To my Manx army. I haven't been able to spend as much time with you all as I would have hoped over the past few years. That said, your support has never wavered. And I have never been in doubt of where I could turn if I needed (the whitey with the boys and a couple of Staropramens).

To everyone else whom I've had the pleasure of meeting and forming connections with, even if time and distance have taken us in different directions. I will forever be thankful to all of you for making me the man I am today.

Funding

It is a pleasure to acknowledge financial support from the European Research Council (ERC) under the European Union's Horizon Europe research and innovation programme (Grant agreement No. ERC-ADG-2021-101052956-BEYOND). The methodologies developed in this work fall within the aims of the GNFM(Gruppo Nazionale per la Fisica Matematica) of the INDAM (Istituto Nazionale di Alta Matematica).

Abstract

This thesis delves into the dynamics of structures subject to velocity dependent restrictions, which are known as nonholonomic constraints. These constraints are applied to elastic structures, and their nonlinear dynamics are analyzed within the framework of bifurcation and stability theory. Initially, the stability of Ziegler's double pendulum is analyzed to show its interesting dynamic behavior and capability of flutter via a Hopf bifurcation.

The main contribution of the thesis is the development of models based on a double pendulum equipped with a non-holonomic constraint, which is a variant of Ziegler's double pendulum.

The *first investigation* that has been carried out, is to consider this device to have a charge concentrated at its tip, where the nonholonomic constraint is located. As such, the new device is named the 'charged Ziegler's double pendulum'. This device is then placed within an ideal solenoid so that there is an additional interaction due to Lorentz force coming from the magnetic induction field within the solenoid. After determining the equilibrium of the system, a stability analysis is preformed, and it is shown that the device still undergoes a Hopf bifurcation. This then allows for a post critical study, whereby focus is brought onto the interaction between the Lorentz force and the other forces prescribed to the device. The study is not limited to the case where the device lies inside the solenoid; the case where it is outside is also examined. Within this setting, the Lorentz force induced is solely a property of the electric field as the magnetic induction field outside the solenoid vanishes. This property is known in electromagnetism as the 'Maxwell–Lodge effect'.

The *second investigation* revisits Ziegler's double pendulum under a nonholonomic constraint and examines its interaction with an oscillator, modeled as a plate attached to an axial spring. A linear stability analysis is then carried out on this system, revealing again the possibility of the system to undergo a Hopf bifurcation. However, when in the dynamic regime, the fluttering which is brought on by the Hopf bifurcation, interacts with the movement of the plate leading to a self-induced resonance phenomenon. When the frequency of the self-induced vibrations arising from a Hopf bifurcation approaches the natural frequency of the plate oscillator, both the limit-cycle amplitude and the mean structural velocity diverge. Moreover, instability regions emerge in which the Hopf bifurcation becomes subcritical; within these regions, the structure may exhibit multiple coexisting limit cycles or transition to chaotic dynamics.

These instability mechanisms are of practical importance: resonance between Hopf-induced oscillations and structural modes can severely reduce stability margins and promote fatigue. Conversely, the same mechanisms may be harnessed for controlled amplification and nonlinear sensing applications.

Forthcoming Papers

The results presented in this thesis are the coming together of two manuscripts:

1 Pastore, A., Harrop, J.C., Bigoni, D., Grillo, A., "Dynamics of a charged Ziegler's double pendulum under the joint action of a follower force and Lorentz force" (2026) *Submitted* [1].

2 Harrop, J.C., Pastore, A., Grillo, A., Bigoni, D., "Coupling between flutter instability and resonance in a viscoelastic structure with a nonholonomic constraint" (2026) *To be submitted* [2].

Contents

Introduction

The ability to craft and design a structure with prescribed properties is a task crucial to human innovation which heavily influences our day to day life. Instabilities used to be considered detrimental to a materials structure and so the aim was to design a material without these features. However, there has now been a shift, and the exploitation of instabilities in solids and structures is now being embraced [3]. Motivated by this sentiment, this thesis is based on the stability, or more fitting, the instability, of elastic structures which are subject to non-holonomic constraints. The work lies at the intersection of several theoretical frameworks, including analytical mechanics, electrodynamics, structural stability, and bifurcation theory. These areas are combined providing a framework for understanding how these constraints can fundamentally alter the stability and dynamical behavior of mechanical systems. More specifically, a core theme throughout this work is a variant of Ziegler's double pendulum [4], presented by Cazzoli et al. [5], in which Ziegler's pendulum is subject to a nonholonomic constraint. In this setting, the device can experience dynamic instability even under *conservative* loading. The structure of the thesis is broken down into three separate chapters.

Chapter 1 outlines relevant theories by which the thesis itself should remain self-contained. Starting from a review on the simplest form of Ziegler's double pendulum, its governing equations are presented and subsequently placed into their dimensionless counterparts by which the characteristic polynomial can be computed. An analytical approach is presented to analyze the roots of the characteristic polynomial in the absence of damping. Then, when damping is added, the Routh–Hurwitz stability criterion is employed alongside a direct inspection of the characteristic polynomial. These methods reveal the interesting stability characteristics of Ziegler's double pendulum. Then an adaption of the double pendulum is presented. One that is seen in Cazzoli et al. [5], where one end of the pendulum remains constrained to move horizontally and the tip of the pendulum now features a non holonomic constraint. It's kinematics are shown and dynamic equations derived via the Extended Hamilton principle. Next, a first glimpse into some theories in electrodynamics is presented, concentrating on the paradigmatic problem of an ideal solenoid within the setting of the temporal gauge, to eliminate the scalar potential, ϕ. Allowing for the first introduction of the Maxwell–Lodge effect [6].

Chapter 2 builds upon the theoretical framework introduced in the first, by considering a charged version of the device proposed by Cazzoli et al. [5]. The system is placed within, or in the vicinity of, an ideal solenoid, and the charged is assumed to be concentrated at the skate constraint. A representative example is shown in Fig. 1, where the blue circle indicates the magnetic induction field, while the red region represents the electric field induced by the magnetic field. For this reason, the system is referred to as the *Charged Ziegler's double pendulum*. The dynamic equations are derived again using the Extended Hamilton principle, then the the static equilibrium is determined, by which the stability of the system can be

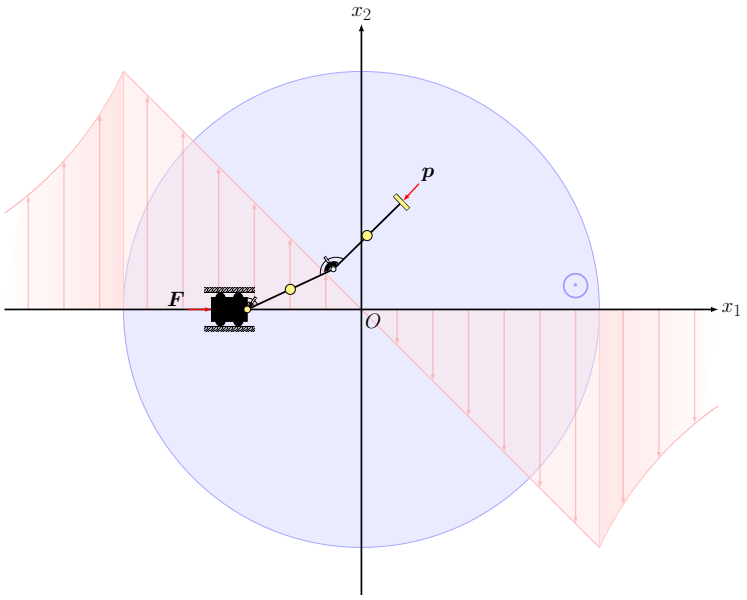

Figure 1: The constrained Ziegler's double pendulum within an ideal solenoid.

explored. This is done to ascertain the impact in which the Lorentz force, stemming from the charged skate being within a magnetic induction field (or outside), has on the overall stability of the system. Moving forward, this chapter is closed with two virtual experiments contextualized for micro-robotics in biological applications. The first experiment sees the device placed within the solenoid.In the second experiment, the device is placed outside the solenoid, where the Maxwell–Lodge effect is observed.

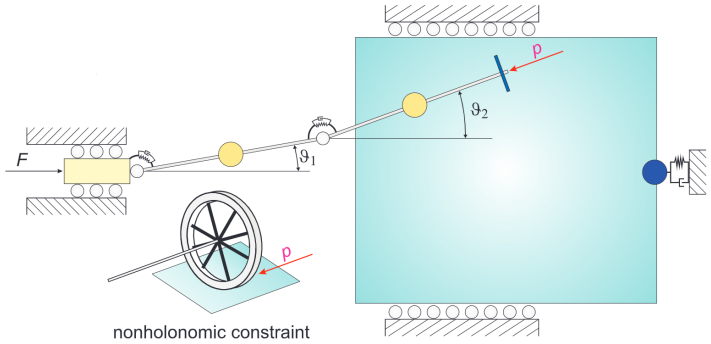

Figure 2: The constrained Ziegler's double pendulum interacting with a moving plate.

Finally, *Chapter 3* follows again an extension of the work presented by Cazzoli et al. [5], where the device can interact with a plate, modeled as a point mass which is connected to an axial spring restricting its movement. This structure is shown in Figure 2. The only interaction between the two systems occurs through the nonholonomic skate constraint. The kinematics of this model is presented, and the equations of motion obtained. An alternative derivation is obtained using a *constrained* version of D'Alembert's principle of virtual work.

Subsequently, a stability analysis is performed about a selected equilibrium configuration, followed by an examination of how the nature of the Hopf bifurcation changes. Finally, the post critical behavior of the system is analyzed. This reveals an interesting resonant phenomenon, where the self induced vibrations which arise from the fluttering of the double pendulum, form an internal resonance with the natural frequency of the plate oscillator. The

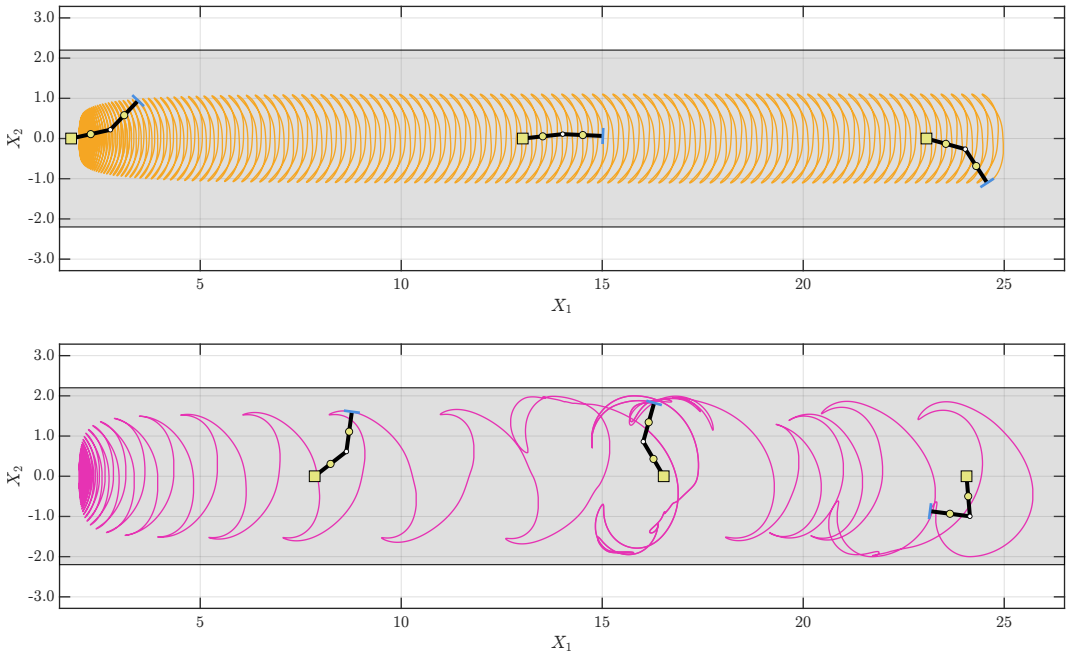

Figure 3: Resonance-driven transition from stable flutter (upper part) to chaotic flutter (lower part).

resonance leads to large-amplitude, potentially divergent responses, as illustrated in Figure 3, where stable periodic motion transitions to chaotic dynamics due to resonant interactions.

Chapter 1

Some consolidated results

In this chapter, The stability of Ziegler's double pendulum is explored, revealing its interesting stability profile. Then, its constrained counterpart is shown, introducing the adaptions to the double pendulum and the nonholonomic constraint. Finally then problem of an ideal solenoid is presented, posulating the existence of a non-null vector potential outside of the solenoid, even when the magnetic induction field is null, known as the '*Maxwell–Lodge effect*' [6]. The text and equations consolidating this chapter are taken from [1].

1.1 Ziegler's double pendulum

Ziegler's double pendulum [4], in its simplest form, is constructed by two homogeneous and rigid bars, of equal length ℓ and equal mass m, connected one to the other via a hinge. The masses of the bars are considered to be concentrated at their midpoints. One of the two bars is hinged on a fixed frame, and the other is subjected to a force, F, directed in parallel with it, known as a follower force. Moreover, the hinges are regarded as viscoelastic, with angular stiffness $k > 0$, and damping $c > 0$. These coefficients lump the viscoelastic properties of the structure into the joints connecting the double pendulum to the fixed frame and the two bars to each other [4, 7]. For reference a diagram of the double pendulum is presented in Figure 1.1. The equations of motion for this system read

$$\begin{aligned}&\frac{5}{4}m\ell^2\,\ddot{\theta}_1+\frac{1}{2}m\ell^2\cos(\theta_1-\theta_2)\ddot{\theta}_2+\frac{1}{2}m\ell^2\sin(\theta_1-\theta_2)\dot{\theta}_2^2\\&=-k(2\theta_1-\theta_2)-c(2\dot{\theta}_1-\dot{\theta}_2)+F\ell\sin(\theta_1-\theta_2),\end{aligned}\tag{1.1a}$$

$$\begin{aligned}&\frac{1}{2}m\ell^2\cos(\theta_1-\theta_2)\ddot{\theta}_1+\frac{1}{4}m\ell^2\ddot{\theta}_2-\frac{1}{2}m\ell^2\sin(\theta_1-\theta_2)\dot{\theta}_1^2\\&=-k(\theta_2-\theta_1)-c(\dot{\theta}_2-\dot{\theta}_1).\end{aligned}\tag{1.1b}$$

By introducing the dimensionless mappings:

$$t\mapsto\frac{t}{\sqrt{m\ell^2/k}},\qquad c\mapsto\frac{c}{\ell\sqrt{mk}},\qquad F\mapsto\frac{F\ell}{k},\tag{1.2}$$

Equations (1.1a) and (1.1b), once linearized about their trivial equilibrium configuration ($\theta_1=\theta_2=0$) hold the form

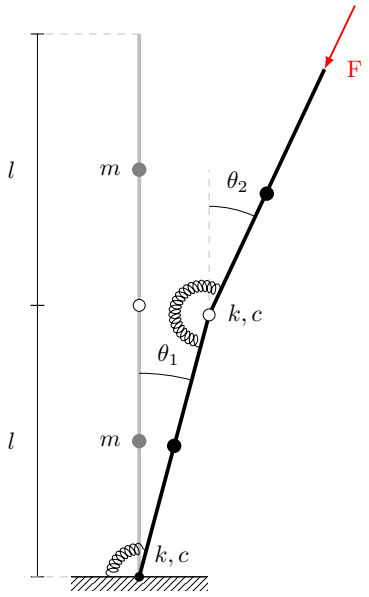

Figure 1.1: Ziegler's double pendulum.

$$\tilde{\mathbf{M}}\ddot{\tilde{\mathsf{q}}} + \tilde{\mathbf{C}}\dot{\tilde{\mathsf{q}}} + (\tilde{\mathbf{K}} + F\tilde{\mathbf{G}})\tilde{\mathsf{q}} = 0. \tag{1.3}$$

Where $\mathsf{q} = [\theta_1 \ \theta_2]^T$, with the superscript dot representing the derivative with respect to the dimensionless time variable, and the explicit notations for the matrices given by,

$$\tilde{\mathbf{M}} = \begin{bmatrix} \frac{5}{4} & \frac{1}{2} \\ \frac{1}{2} & \frac{1}{4} \end{bmatrix}, \qquad \tilde{\mathbf{C}} = \begin{bmatrix} 2c & -c \\ -c & c \end{bmatrix}, \qquad \tilde{\mathbf{K}} = \begin{bmatrix} 2 & -1 \\ -1 & 1 \end{bmatrix}, \qquad \tilde{\mathbf{G}} = \begin{bmatrix} -1 & 1 \\ 0 & 0 \end{bmatrix}. \tag{1.4}$$

Within the theory of small oscillations [8, 9], and in the neighborhood of the equilibrium, θ_1 and θ_2 are assumed to be harmonic functions of time, $\theta_i = A_i \exp^{\lambda t}$ for $i = 1, 2$. Where A_i are (complex) amplitudes, and λ is the complex circular frequency. Substituting these harmonic functions into Equation (1.3) yields a generalized eigenvalue problem for λ^2, which is given by

$$\left[\tilde{\mathbf{M}}\lambda^2 + \tilde{\mathbf{C}}\lambda + \tilde{\mathbf{K}} + F\tilde{\mathbf{G}}\right]\mathbf{A} = 0. \tag{1.5}$$

Computing the determinant of the block-wise matrix on the left-hand side of Equation (1.5) yields a polynomial equation of the fourth order in λ, which can be written as

$$Q(\lambda) \coloneqq a_0\lambda^4 + a_1\lambda^3 + a_2\lambda^2 + a_3\lambda + a_4 = 0, \tag{1.6}$$

with the coefficients a_0, a_1, a_2, a_3, a_4 being all real and given by

$$a_0 = 1, \qquad a_1 = 44\,c, \qquad a_2 = 44 + 16\,c^2 - 12F, \qquad a_3 = 32\,c, \qquad a_4 = 16. \tag{1.7}$$

Although a_0 is equal to unity, a_1 and a_3 depend only on c, and a_2 depends on both c and F, it is convenient to regard all coefficients as *formally* depending on c and F. In particular, as the purpose of this study is to analyze the stability of the system under the follower force F, the coefficients $a_0, a_1, \ldots, a_4$ are regarded as functions of F, parameterized by c.

The polynomial equation (1.6) has in general four complex roots. Since it has real coefficients and is of even grade, its four roots, hereafter denoted as $\lambda_1, \lambda_2, \lambda_3, \lambda_4$, are paired in the sense that, if λ_1 and λ_2 are complex numbers, then $\lambda_4 \equiv \bar{\lambda}_1$ and $\lambda_3 \equiv \bar{\lambda}_2$ We also notice that the roots $\lambda_1, \lambda_2, \lambda_3, \lambda_4$ are functions of F depending parametrically on c.

1.1.1 The case of the undamped double pendulum: symmetric diagram of the roots

If c is set equal to zero, Equation (1.6) simplifies to a biquadratic equation in λ, since the coefficients a_1 and a_3 disappear, (1.7). Hence, by setting $\Delta(F) := [a_2(F)]^2 - 4a_4(F)$, the roots of Equation (1.6) can be solved for λ^2 as

$$\lambda_1^2(F) = -\frac{a_2(F)}{2} - \frac{\sqrt{\Delta(F)}}{2}, \qquad \lambda_2^2(F) = -\frac{a_2(F)}{2} + \frac{\sqrt{\Delta(F)}}{2}, \qquad \text{if } \Delta(F) \geq 0, \tag{1.8a}$$

$$\lambda_1^2(F) = -\frac{a_2(F)}{2} - i\frac{\sqrt{|\Delta(F)|}}{2}, \quad \lambda_2^2(F) = -\frac{a_2(F)}{2} + i\frac{\sqrt{|\Delta(F)|}}{2}, \quad \text{if } \Delta(F) < 0. \tag{1.8b}$$

Note that the form of $\lambda_1^2(F)$ and $\lambda_2^2(F)$ in Equations (1.8a) and (1.8b) depends on the asymmetry of the matrix $\tilde{\mathbf{K}} + F\tilde{\mathbf{G}}$ when $F \neq 0$. Indeed, when this matrix is symmetric, the roots λ are purely imaginary [8].

For the following calculations, it is convenient to introduce the auxiliary quantities

$$H_1(F) := \frac{a_2(F)}{2} + \frac{\sqrt{\Delta(F)}}{2}, \qquad H_2(F) := \frac{a_2(F)}{2} - \frac{\sqrt{\Delta(F)}}{2}, \qquad \text{if } \Delta(F) \geq 0, \tag{1.9a}$$

$$K_1(F) := \frac{a_2(F)}{2} + i\frac{\sqrt{|\Delta(F)|}}{2}, \quad K_2(F) := \frac{a_2(F)}{2} - i\frac{\sqrt{|\Delta(F)|}}{2}, \quad \text{if } \Delta(F) < 0. \tag{1.9b}$$

For notational convenience, we set $K(F) := K_1(F) \equiv \bar{K}_2(F)$ for $\Delta(F) < 0$.

Case #1: $\Delta = 0$ We have $H_1(F) \equiv H_2(F) \equiv H(F) := a_2(F)/2$, and, in terms of the values assumed by a_2 and a_4, the discriminant $\Delta := a_2^2 - 4a_4$ vanishes at the two *critical* values of F:

$$F_1 = 3, \qquad F_2 = \frac{13}{3}. \tag{1.10}$$

For these values, the squared eigenvalues are

$$\lambda_1^2(F_1) = \lambda_2^2(F_1) = -H(F_1) = -\frac{a_2(F_1)}{2} = -4 = i^2 4, \tag{1.11}$$

$$\lambda_1^2(F_2) = \lambda_2^2(F_2) = -H(F_2) = -\frac{a_2(F_2)}{2} = +4, \tag{1.12}$$

leading to

$$\lambda_{1,1}(F_1) = \lambda_{2,1}(F_1) = -i2, \qquad \lambda_{1,2}(F_1) = \lambda_{2,2}(F_1) = +i2, \tag{1.13a}$$

$$\lambda_{1,2}(F_2) = \lambda_{2,1}(F_2) = -2, \qquad \lambda_{1,1}(F_2) = \lambda_{2,2}(F_2) = +2. \tag{1.13b}$$

Case #2: $\Delta > 0$ The discriminant Δ is positive for the values of F:

$$F \in [0, F_1\,[\cup]F_2, +\infty[. \tag{1.14}$$

Two situations occur:

2.1 For $F \in [0, F_1[$, the coefficient $a_2(F)$ is strictly positive. The following two different *real* and *negative* values of λ^2 exist

$$0 > \lambda_1^2(F) = i^2 H_1(F), \qquad H_1(F) > 0 \tag{1.15a}$$
$$0 > \lambda_2^2(F) = i^2 H_2(F), \qquad H_2(F) > 0 \tag{1.15b}$$

Since $\lambda_1^2(F)$ and $\lambda_2^2(F)$ are negative, each of them produces a pair of purely imaginary conjugate roots,

$$\lambda_{1,1}(F) = -i\sqrt{H_1(F)}, \qquad \lambda_{1,2}(F) = +i\sqrt{H_1(F)}, \tag{1.16a}$$
$$\lambda_{2,1}(F) = -i\sqrt{H_2(F)}, \qquad \lambda_{2,2}(F) = +i\sqrt{H_2(F)}. \tag{1.16b}$$

Accordingly, the system linearized about the static equilibrium is *marginally stable* [10]. So, if perturbed from equilibrium, the system oscillates around its equilibrium configuration. We emphasize that the necessary and sufficient condition for stability, which requires the real part of all the roots to be strictly negative [10], is not met in this first case.

2.2 For $F \in]F_2, +\infty[$, the coefficient $a_2(F)$ is strictly negative and the following two *real* and *positive* values for λ^2 exist

$$0 < \lambda_1^2(F) = -H_1(F), \qquad H_1(F) < 0, \tag{1.17a}$$
$$0 < \lambda_2^2(F) = -H_2(F), \qquad H_2(F) < 0, \tag{1.17b}$$

each of which produces one pair of real roots,

$$\lambda_{1,1}(F) = +\sqrt{-H_1(F)}, \qquad \lambda_{1,2}(F) = -\sqrt{-H_1(F)}, \tag{1.18a}$$
$$\lambda_{2,1}(F) = -\sqrt{-H_2(F)}, \qquad \lambda_{2,2}(F) = +\sqrt{-H_2(F)}. \tag{1.18b}$$

Since $\lambda_{1,1}(F)$ and $\lambda_{2,1}(F)$ are real and strictly positive for $F \in]F_2, +\infty[$, the phenomenon of 'blow up', or divergence, is expected to occur in this range of values of F, where the solution is *not* oscillatory.

Case #3: $\Delta < 0$ The discriminant Δ is negative for the following values of F:

$$F \in]F_1, F_2[. \tag{1.19}$$

Two *complex conjugate* values for λ^2 exist,

$$\lambda_1^2(F) = -K_1(F) = -K(F), \tag{1.20a}$$
$$\lambda_2^2(F) = -K_2(F) = -\bar{K}(F), \tag{1.20b}$$

whose roots are given by

$$\lambda_{1,1}(F) = -i\sqrt{\rho(F)}\exp\left(+i\frac{\phi(F)}{2}\right), \qquad \lambda_{1,2}(F) = +i\sqrt{\rho(F)}\exp\left(+i\frac{\phi(F)}{2}\right), \tag{1.21a}$$
$$\lambda_{2,1}(F) = -i\sqrt{\rho(F)}\exp\left(-i\frac{\phi(F)}{2}\right), \qquad \lambda_{2,2}(F) = +i\sqrt{\rho(F)}\exp\left(-i\frac{\phi(F)}{2}\right). \tag{1.21b}$$

where

$$\rho(F) \coloneqq \sqrt{\mathrm{Re}[K(F)]^2 + \mathrm{Im}[K(F)]^2}, \qquad \phi(F) \coloneqq \arctan\left(\frac{\mathrm{Im}[K(F)]}{\mathrm{Re}[K(F)]}\right). \tag{1.22}$$

Note that the following conjugacy relations hold $\lambda_{1,1}(F) = \bar{\lambda}_{2,2}(F)$ and $\lambda_{1,2}(F) = \bar{\lambda}_{2,1}(F)$.

For future reference, we also provide for these roots the equivalent expressions

$$\lambda_{1,1}(F) = \sqrt{\rho(F)}\left(+\sin\frac{\phi(F)}{2} - i\cos\frac{\phi(F)}{2}\right), \quad \lambda_{1,2}(F) = \sqrt{\rho(F)}\left(-\sin\frac{\phi(F)}{2} + i\cos\frac{\phi(F)}{2}\right), \tag{1.23a}$$

$$\lambda_{2,1}(F) = \sqrt{\rho(F)}\left(-\sin\frac{\phi(F)}{2} - i\cos\frac{\phi(F)}{2}\right), \quad \lambda_{2,2}(F) = \sqrt{\rho(F)}\left(+\sin\frac{\phi(F)}{2} + i\cos\frac{\phi(F)}{2}\right). \tag{1.23b}$$

Referring to Figure 1.2a, since the real parts $\mathrm{Re}[\lambda_{1,2}(F)] = \mathrm{Re}[\lambda_{2,1}(F)] < 0$ are negative for all the considered values of $F \in]F_1, F_2[$, the roots $\lambda_{1,2}(F)$ and $\lambda_{2,1}(F)$ yield oscillating solutions with amplitude decreasing to zero as time increases. However, since the real parts $\mathrm{Re}[\lambda_{1,1}(F)] = \mathrm{Re}[\lambda_{2,2}(F)]$ are positive, the roots $\lambda_{1,1}(F)$ and $\lambda_{2,2}(F)$ yield oscillating solutions with amplitudes increasing in time, thereby being responsible for the globally unstable behavior of the system. This phenomenon is known as *flutter instability* [8].

With these cases in mind, the critical values F_1 and F_2 henceforth will be renamed $F^{\mathrm{nd}}_{\mathrm{flu}}$ and $F^{\mathrm{nd}}_{\mathrm{div}}$ to indicate that they specify, in the absence of damping (superscript 'nd'), the values of F delimitating the region of flutter. In particular, for $F > F^{\mathrm{nd}}_{\mathrm{flu}}$ at least one root has positive real part, and, thus, the system passes from the marginally stable region to the first unstable region in which flutter occurs. The second critical value $F^{\mathrm{nd}}_{\mathrm{div}} > F^{\mathrm{nd}}_{\mathrm{flu}}$ marks the end of the flutter regime, and, for $F > F^{\mathrm{nd}}_{\mathrm{div}}$, the region of divergence instability, without oscillatory behaviour. It is worth emphasizing that at $F^{\mathrm{nd}}_{\mathrm{flu}}$ and $F^{\mathrm{nd}}_{\mathrm{div}}$, the real parts of the roots split in different branches, whereas the imaginary parts coalesce. This is illustrated in Figure 1.2a, where the points B_0, B_1, and B_2 highlight the three branching points of the real parts when $c = 0$.

From now on, we adopt the following numbering of the roots, which ensures that both the real and imaginary parts of all roots are continuous functions of F, while preserving pairwise conjugacy (i.e., $\lambda_1(F)$ and $\lambda_4(F)$ are complex conjugate, and $\lambda_2(F)$ and $\lambda_3(F)$ are complex conjugate for $F \in [0, F^{\mathrm{nd}}_{\mathrm{div}}]$):

$$\lambda_1(F) = \begin{cases} \lambda_{1,2}(F) & \text{if } F \in [0, F^{\mathrm{nd}}_{\mathrm{flu}}[\,, \\ \lambda_{1,2}(F) & \text{if } F \in [F^{\mathrm{nd}}_{\mathrm{flu}}, F^{\mathrm{nd}}_{\mathrm{div}}], \\ \lambda_{2,1}(F) & \text{if } F \in]F^{\mathrm{nd}}_{\mathrm{div}}, +\infty[\,. \end{cases} \quad \lambda_2(F) = \begin{cases} \lambda_{2,2}(F) & \text{if } F \in [0, F^{\mathrm{nd}}_{\mathrm{flu}}[\,, \\ \lambda_{2,2}(F) & \text{if } F \in [F^{\mathrm{nd}}_{\mathrm{flu}}, F^{\mathrm{nd}}_{\mathrm{div}}], \\ \lambda_{2,2}(F) & \text{if } F \in]F^{\mathrm{nd}}_{\mathrm{div}}, +\infty[\,. \end{cases} \tag{1.24a}$$

$$\lambda_3(F) = \begin{cases} \lambda_{2,1}(F) & \text{if } F \in [0, F^{\mathrm{nd}}_{\mathrm{flu}}[\,, \\ \lambda_{1,1}(F) & \text{if } F \in [F^{\mathrm{nd}}_{\mathrm{flu}}, F^{\mathrm{nd}}_{\mathrm{div}}], \\ \lambda_{1,1}(F) & \text{if } F \in]F^{\mathrm{nd}}_{\mathrm{div}}, +\infty[\,. \end{cases} \quad \lambda_4(F) = \begin{cases} \lambda_{1,1}(F) & \text{if } F \in [0, F^{\mathrm{nd}}_{\mathrm{flu}}[\,, \\ \lambda_{2,1}(F) & \text{if } F \in [F_1, F^{\mathrm{nd}}_{\mathrm{div}}], \\ \lambda_{1,2}(F) & \text{if } F \in]F^{\mathrm{nd}}_{\mathrm{div}}, +\infty[\,. \end{cases} \tag{1.24b}$$

1.1.2 The case of the damped double pendulum: asymmetric diagram of the roots

In this section we extract the critical loads of flutter and divergence for $c > 0$. We use one method to determine the critical load of flutter and another method for the critical load of divergence, now seen as depending on c via the notation $F_{\mathrm{flu}}(c)$ and $F_{\mathrm{div}}(c)$. The first method

is the Routh–Hurwitz stability criterion [10, 4] and provides an explicit expression for $F_{\text{flu}}(c)$. The second method relies on the direct inspection of the characteristic polynomial provided in Equation (1.6), whereby we compute numerically $F_{\text{div}}(c)$ for given values of $c > 0$.

Critical load of flutter The Routh–Hurwitz criterion is a direct test done on the coefficients of a polynomial to determine if all of its roots lie on the left half of the complex plane, i.e., if they all have negative real parts. For our purposes, we apply this criterion to the characteristic equation (1.6) to determine sufficient and necessary conditions on F to guarantee that the roots $\lambda_1, \lambda_2, \lambda_3, \lambda_4$ all have negative real part. This yields the threshold value, $F_{\text{flu}}(c)$, approached from the left, i.e., in the limit $F \to [F_{\text{flu}}(c)]^-$, with the force range $[0, F_{\text{flu}}(c)[$ corresponding to the region, in the undamped case, in which all the roots have zero real part (see Figure 1.2a for $F \in [0, F^{\text{nd}}_{\text{flu}}[$.)

The Hurwitz matrix associated with the characteristic polynomial in (1.6) is constructed as

$$\mathsf{H}_4 = \begin{bmatrix} a_1 & a_0 & 0 & 0 \\ a_3 & a_2 & a_1 & a_0 \\ 0 & a_4 & a_3 & a_2 \\ 0 & 0 & 0 & a_4 \end{bmatrix}. \tag{1.25}$$

Considering now all the principle minors which are generated by H_4, the condition to guarantee stability of the system is that *all* of these principle minors must not vanish and be positive. To this end, we find that the following relations must hold true for stability,

$$0 < a_1, \tag{1.26a}$$
$$0 < a_1 a_2 - a_0 a_3, \tag{1.26b}$$
$$0 < a_3(a_1 a_2 - a_0 a_3) - a_1^2 a_4, \tag{1.26c}$$
$$0 < (a_3(a_1 a_2 - a_0 a_3) - a_1^2 a_4) a_4. \tag{1.26d}$$

Since $a_1 = 44c$ (see Equation $(1.7)_2$), the inequality (1.26a) is identically satisfied, as we consider strictly positive damping coefficients. Further to this, we notice that the condition (1.26d) is the condition (1.26c) multiplied by a_4, which, again, is positive (see Equation $(1.7)_4$, in which $a_4 = 16$). Hence, the inequality (1.26d) is satisfied automatically if the condition (1.26c) is fulfilled. We can thus concentrate on the inequalities (1.26b) and (1.26c). By solving them, we obtain the threshold value of F, $F_{\text{flu}}(c)$, below which all the roots have negative real part. Such condition reads [8]

$$F < F_{\text{flu}}(c), \qquad F_{\text{flu}}(c) = \frac{39}{22} + \frac{4c^2}{3}. \tag{1.27}$$

Therefore, the system is stable for $F < F_{\text{flu}}(c)$, and it experiences flutter or divergence instability otherwise. More in detail, $F_{\text{flu}}(c)$ defines, for varying damping coefficient $c > 0$, the onset of *flutter* when damping is present.

Critical load of divergence As mentioned earlier, the critical load of divergence is obtained by directly examining the discriminant of the characteristic polynomial (1.6). The general formula for the discriminant of a polynomial $Q(\lambda)$ of grade n is given by [11]

$$D[Q] = (-1)^{n(n-1)/2} a_0^{-1} \text{Res}[Q, Q'], \quad Q(\lambda) = a_0\lambda^n + a_1\lambda^{n-1} + \cdots + a_{n-1}\lambda + a_n, \tag{1.28}$$

where $Q'(\lambda)$ is the derivative of $Q(\lambda)$ with respect to λ, and $\mathrm{Res}[Q, Q']$ is the 'resultant' of the polynomials $Q(\lambda)$ and $Q'(\lambda)$. Since, for the problem at hand, the grade n is equal to 4, $\mathrm{Res}[Q, Q']$ can be computed as the determinant of the Sylvester matrix $\mathsf{S}_n \equiv \mathsf{S}_4$ formed by the polynomials $Q(\lambda)$ and $Q'(\lambda)$, which reads [12, 13]

$$\mathrm{Res}[Q, Q'] := \det(\mathsf{S}_4) = \begin{vmatrix} a_0 & a_1 & a_2 & a_3 & a_4 & 0 & 0 \\ 0 & a_0 & a_1 & a_2 & a_3 & a_4 & 0 \\ 0 & 0 & a_0 & a_1 & a_2 & a_3 & a_4 \\ 4a_0 & 3a_1 & 2a_2 & a_3 & 0 & 0 & 0 \\ 0 & 4a_0 & 3a_1 & 2a_2 & a_3 & 0 & 0 \\ 0 & 0 & 4a_0 & 3a_1 & 2a_2 & a_3 & 0 \\ 0 & 0 & 0 & 4a_0 & 3a_1 & 2a_2 & a_3 \end{vmatrix}. \tag{1.29}$$

Note that, in our case, $a_0 = 1$. We emphasize that, for $c \neq 0$, we use the general formula $D[Q]$ because, even though we have $n = 4$, $Q(\lambda)$ does not reduce now to a polynomial of grade two in λ^2, as is the case for $c = 0$. Thus, Equation $(1.28)_1$ becomes

$$\begin{aligned} D[Q] = {} & 256a_4^3 - 192a_1a_3a_4^2 - 128a_2^2a_4^2 + 144a_2a_3^2a_4 - 27a_3^4 + 144a_1^2a_2a_4^2 \\ & - 6a_1^2a_3^2a_4 - 80a_1a_2^2a_3a_4 + 18a_1a_2a_3^3 + 16a_2^4a_4 - 4a_2^3a_3^2 \\ & - 27a_1^4a_4^2 + 18a_1^3a_2a_3a_4 - 4a_1^3a_3^3 - 4a_1^2a_2^3a_4 + a_1^2a_2^2a_3^2. \end{aligned} \tag{1.30}$$

Since a_1, a_2, a_3 and a_4 can be formally expressed as functions of F, although, in fact, only a_2 depends on F (see Equation (1.7)), we can write $D[Q] \equiv P(F)$, where $P(F)$ is a quartic polynomial in F, having coefficients depending parametrically on $c > 0$. Since the expression of $P(F)$ is too long, we omit reporting it in this work, and we solve numerically the equation $P(F) = 0$ yielding the values of F that, for fixed $c > 0$, entail the vanishing of the discriminant (1.30). These values of F are those which change the nature of the roots $\lambda_1, \lambda_2, \lambda_3, \lambda_4$ of $Q(\lambda)$ in the original polynomial. Specifically, two of the four solutions to $P(F) = 0$ are complex and conjugate, and can thus be disregarded since the force F should be represented by real numbers only. The two remaining solutions of $P(F) = 0$ are real numbers corresponding to the branching points of the real parts of the roots of $Q(\lambda)$ in Equation (1.6) (see the points marked as B_1 and B_2 in Figure 1.2b). With respect to Figure 1.2b, referring to the case $c = 0.1$, the largest of these two (real) solutions to $P(F) = 0$ identifies the branching point B_2 and is the one above which all the roots of $Q(\lambda)$ have zero imaginary part. In particular, two of them have negative real part, and the other two have positive real part, thereby leading to blow-up, or divergence (without oscillations), of the solutions θ_1 and θ_2 of the double pendulum.

By using the Routh–Hurwitz criterion (see Equation (1.27)) and determining the zeros of $P(F)$ e.g. for $c = 0.1$, we find the threshold values of F

$$F_{\mathrm{flu}}(c = 0.1) = 1.7861, \qquad F_{\mathrm{div}}(c = 0.1) = 5.1623, \tag{1.31}$$

corresponding to the onset of the flutter and divergence instabilities, respectively, in the presence of damping. The λ-F diagram for $c = 0.1$ is presented in Figure 1.2b.

Remark 1 (Ziegler's paradox [8, 14, 15])**.** *If one assumes $c = 0$, the results presented in Section 1.1.1 must be recovered. Indeed, one obtains $D[Q] \equiv P(F) \equiv 16\, a_4(F)[\Delta(F)]^2$ and, thus, the vanishing of $P(F)$ yields the two real and positive values $F = F_{\mathrm{flu}}^{\mathrm{nd}} = 3$ and $F = F_{\mathrm{div}}^{\mathrm{nd}} = 13/3$, but both with multiplicity two. Indeed, in this case, in which c is set equal to zero, there are no dissipative mechanisms in the double pendulum subsystem that*

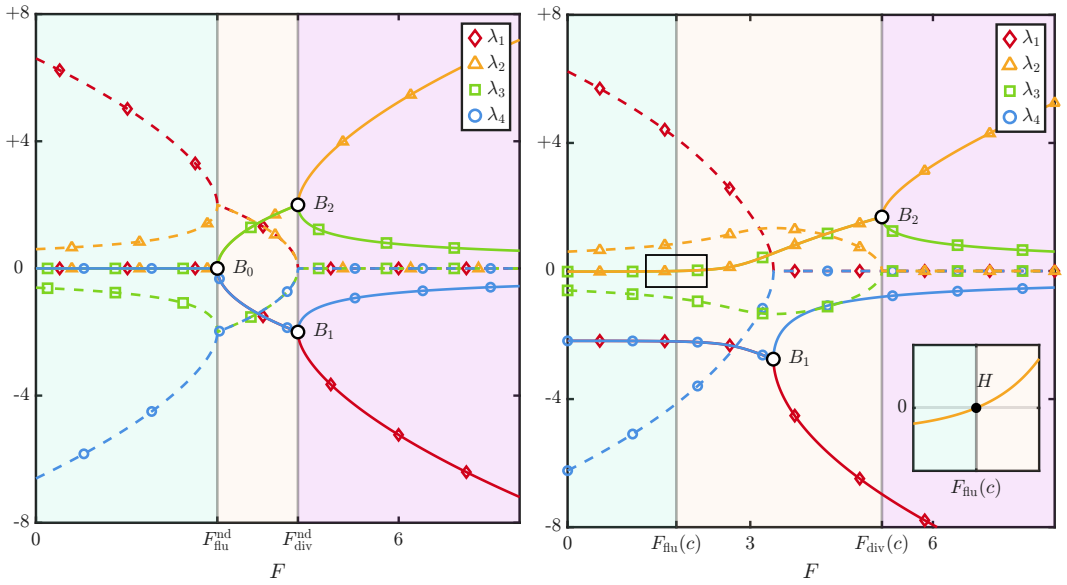

(a) Case $c = 0$ (symmetric diagram of the roots). **(b)** Case $c = 0.1$ (asymmetric diagram of the roots).

Figure 1.2: λ-F diagrams of the roots of $Q(\lambda; F)$ in Equation (1.6) for $c = 0$ and $c = 0.1$.

can produce limit cycles in the fluttering regime. However, as predicted by Ziegler's paradox *(see [8, 14, 15]),* $F_{\text{flu}}^{\text{nd}} = 3$ *is greater than the infimum of* $F_{\text{flu}}(c)$ *for* $c \in]0, +\infty[$*, as computed via the Routh–Hurwitz criterion in Equation (1.27), i.e.,*

$$F_{\text{flu}}^{\text{nd}} = 3 > F_{\text{flu}}^{(0)} := \lim_{c \to 0^+} F_{\text{flu}}(c) = 39/22 \simeq 1.7727. \tag{1.32}$$

Thus, for $F \in]F_{\text{flu}}^{(0)}, F_{\text{flu}}^{\text{nd}}]$*, the roots of* $Q(\lambda)$ *may take on non-negative values. Hence, one may find damping coefficients* $c > 0$ *such that for* F *compliant with* $F_{\text{flu}}^{(0)} < F_{\text{flu}}(c) \leq F \leq F_{\text{flu}}^{\text{nd}}$*, the roots of* $Q(\lambda)$ *can have non-negative real part and non-zero imaginary part, so that flutter occurs.*

Remark 2 (Symmetry breaking of the λ-F diagram due to the presence of damping)**.** *It is interesting to see how the branching and merging points of the real and imaginary parts of the roots of* $Q(\lambda)$ *change from Figure 1.2a to Figure 1.2b when switching from zero damping to nonzero damping (in this case,* $c = 0.1$*). Specifically, the value* $F = F_{\text{flu}}^{\text{nd}} = 3$ *corresponds to the branching point* B_0 *in the* λ-F *diagram in the case with no damping (see Figure 1.2a), whereas no branching occurs at* $F = F_{\text{flu}}(c = 0.1)$ *for the case with damping (see Figure 1.2b, Point H of the magnified region). Note that the onset of the flutter region has to do only with the exceeding of the threshold force* $F_{\text{flu}}(c = 0.1)$*, not with the presence of a branching point in* λ-F *diagram of the roots. In addition, we notice that, in the case with damping, the real parts of the roots* $\lambda_1(F)$ *(solid line with diamond) and* $\lambda_4(F)$ *(solid line with circles) overlap from* $F = 0$ *until the abscissa of* B_1*. The same applies also to* $\lambda_2(F)$ *(solid line with triangles) and* $\lambda_3(F)$ *(solid line with squares) from* $F = 0$ *until the abscissa of* B_2*. Moreover, another consequence of damping is that the (real) solutions of* $P(F) = 0$ *given by the abscissae of the points* B_1 *and* B_2 *in Figure 1.2b experience a mutual increase in distance as* c *increases. Finally, for* $c \neq 0$*, the roots* $\lambda_1(F)$*,* $\lambda_2(F)$*,* $\lambda_3(F)$ *and* $\lambda_4(F)$ *can*

be defined similarly to the roots in Equations (1.24a) *and* (1.24b)*, with* $F_{\text{flu}}^{\text{nd}}$ *and* $F_{\text{div}}^{\text{nd}}$ *being replaced by* $F_{\text{flu}}(c)$ *and* $F_{\text{div}}(c)$*, respectively.*

With this in mind, and with reference to Figures 1.2a and 1.2b, we can comment on the type of bifurcation which is experienced in each of the cases. When addressing the case without damping (Figure 1.2a), Ziegler's double pendulum is depicted as a Hamiltonian system, and we observe the occurrence of a Hamiltonian Hopf bifurcation [16, 17]. Such a bifurcation occurs when the roots of the characteristic polynomial $Q(\lambda)$ behave as follows (see Figure 1.3 for a graphical representation of points a., b., and c., below):

a. For $F \in [0, F_{\text{flu}}^{\text{nd}}[$, the four roots of $Q(\lambda)$ are purely imaginary and occur in two complex-conjugate pairs, all distinct from one another. Two of them have strictly positive imaginary part, while the other two have strictly negative imaginary part (see the four distinct curves on the left-hand side of Figure 1.2a).

b. As the control parameter increases and reaches the critical value $F \equiv F_{\text{flu}}^{\text{nd}}$, the two roots with strictly positive imaginary part coalesce into a single purely imaginary root with positive imaginary part and zero real part. The two roots with strictly negative imaginary part undergo an analogous coalescence, merging into a purely imaginary root with negative imaginary part. The two resulting roots still form a complex-conjugate pair.

c. For $F \in]F_{\text{flu}}^{\text{nd}}, F_{\text{div}}^{\text{nd}}[$ (the flutter region), the two coalesced pairs split and acquire nonzero real parts: one with positive real part and the other with negative real part. The corresponding roots are symmetric with respect to the real axis in the λ-F diagram, but they are no longer complex conjugates of one another.

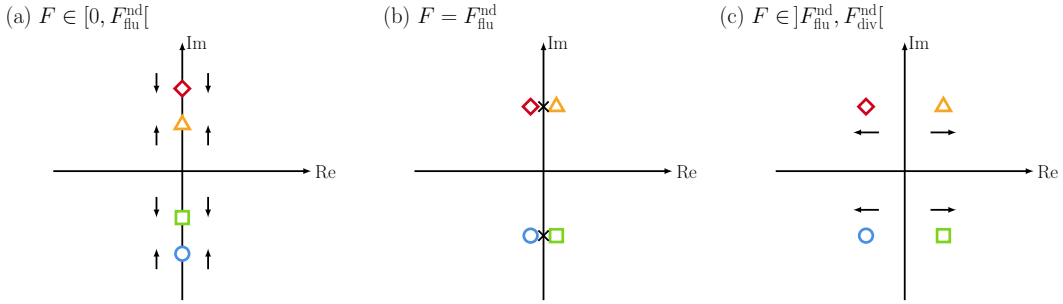

Figure 1.3: Graphical representation of the behavior of the roots in the case of the Hamiltonian Hopf bifurcation.

When addressing the case without damping (Figure 1.2b), Ziegler's double pendulum is no longer depicted as a Hamiltonian system, and in this case we observe the occurrence of a Hopf bifurcation [15]. This comes about when the following three conditions are met:

1. At the onset of flutter, $\mathsf{q} = [0\ 0]^T$ is an equilibrium state of equations (1.1a) and (1.1b). This condition is trivially satisfied.

2. At $F = F_{\text{flu}}(\tilde{c})$, *only* one pair of purely imaginary and complex conjugate eigenvalues exist, $\lambda_2(F)$ and $\lambda_3(F) \equiv \bar{\lambda}_2(F)$, each of which has unitary algebraic multiplicity, while the remaining ones have nonzero real part (negative in our case).

3. The eigenvalues $\lambda_2(F)$ and $\lambda_3(F) \equiv \bar{\lambda}_2(F)$ that, at $F = F_{\text{flu}}(c)$, form the aforementioned pair of conjugate imaginary eigenvalues must depend on F in such a way that their real part be differentiable at $F_{\text{flu}}(c)$ and compliant with the condition

$$\frac{\mathrm{d}\,\mathrm{Re}[\lambda_{2,3}]}{\mathrm{d}F}(F_{\text{flu}}(c)) \neq 0. \tag{1.33}$$

In summary, Ziegler's double pendulum is capable of complex dynamics which is brought on via a destabilization due to a follower load once it has crossed a certain threshold value. In the absence of dissipation, this destabilization is materialized with a Hamiltonian Hopf bifurcation. However, there are no dissipative mechanisms to bind the oscillations which arise, so fluttering occurs without bound. Whereas, when dissipation is considered, a Hopf bifurcation occurs, and the fluttering motion can be bounded. This result is carried through this work and forms a central part of this thesis when investigating the bifurcations of analogous systems.

1.2 Ziegler's pendulum subject to a nonholonomic constraint

This variant of Ziegler's double pendulum introduced by Cazzolli et al. [5], and it used in throughout this thesis. It consists of two homogeneous and rigid bars, denoted by $\mathscr{B}_1$ and $\mathscr{B}_2$, each of length ℓ and mass m, connected by a hinge that links the right end of $\mathscr{B}_1$ to left end of $\mathscr{B}_2$. The left end of the bar $\mathscr{B}_1$ is hinged on a cart, which is free to move along a straight line on a fixed plane. A wheel is mounted at the end of bar $\mathscr{B}_2$, the bar acting as its axle, and rolls without slipping on a fixed plane. The non-slipping wheel is the realization of a non-holonomic constraint of the 'skate' type. Overall, the device may experience only planar motions, parallel to the fixed plane, Figure 1.4.

In a fixed Cartesian reference frame with origin O and axes aligned with the orthonormal vectors $\boldsymbol{e}_1$, $\boldsymbol{e}_2$, and $\boldsymbol{e}_3$, the motion of the device is confined to the plane spanned by $\boldsymbol{e}_1$ and $\boldsymbol{e}_2$. Angles θ_1 and θ_2 measure the time-dependent inclinations of the bars $\mathscr{B}_1$ and $\mathscr{B}_2$ with the axis parallel with $\boldsymbol{e}_1$, respectively. Moreover, X_{c} denotes the instantaneous position, measured from O along $\boldsymbol{e}_1$, of the point of the cart to which $\mathscr{B}_1$ is hinged, Figure 1.4. The Lagrangian parameters θ_1, θ_2, and X_{c}, together with their velocities and accelerations, are collected in the vectors $q := (\theta_1, \theta_2, X_{\text{c}})$, $\dot{q} := (\dot{\theta}_1, \dot{\theta}_2, \dot{X}_{\text{c}})$, and $\ddot{q} := (\ddot{\theta}_1, \ddot{\theta}_2, \ddot{X}_{\text{c}})$. Moreover, we introduce the following points of interest, whose spatial positions are expressed as functions of the Lagrangian coordinates:

$$x_A = \hat{x}_A(q) = (X_{\text{c}}, 0, 0), \tag{1.34a}$$

$$x_B = \hat{x}_B(q) = (X_{\text{c}} + \frac{1}{2}\ell\cos\theta_1, \frac{1}{2}\ell\sin\theta_1, 0), \tag{1.34b}$$

$$x_M = \hat{x}_M(q) = (X_{\text{c}} + \ell\cos\theta_1, \ell\sin\theta_1, 0), \tag{1.34c}$$

$$x_C = \hat{x}_C(q) = (X_{\text{c}} + \ell\cos\theta_1 + \frac{1}{2}\ell\cos\theta_2, \ell\sin\theta_1 + \frac{1}{2}\ell\sin\theta_2, 0), \tag{1.34d}$$

$$x_D = \hat{x}_D(q) = (X_{\text{c}} + \ell\cos\theta_1 + \ell\cos\theta_2, \ell\sin\theta_1 + \ell\sin\theta_2, 0), \tag{1.34e}$$

which represent, in order: the position of the cart (point A); the midpoint of $\mathscr{B}_1$ (point B); the hinge connecting $\mathscr{B}_1$ to $\mathscr{B}_2$ (point M); the midpoint of $\mathscr{B}_2$ (point C); and the position

of the massless wheel (point D). Accordingly, the instantaneous orientations of the bars $\mathscr{B}_1$ and $\mathscr{B}_2$ are given by the unit vectors

$$\boldsymbol{n}_1 \equiv \hat{\boldsymbol{n}}_1(q) = (\cos\theta_1)\boldsymbol{e}_1 + (\sin\theta_1)\boldsymbol{e}_2, \qquad \boldsymbol{n}_2 \equiv \hat{\boldsymbol{n}}_2(q) = (\cos\theta_2)\boldsymbol{e}_1 + (\sin\theta_2)\boldsymbol{e}_2, \tag{1.35}$$

while the velocities of the points of interest are

$$\boldsymbol{v}_A = \hat{\boldsymbol{v}}_A(q,\dot{q}) = \dot{X}_\mathrm{c}\,\boldsymbol{e}_1, \tag{1.36a}$$

$$\boldsymbol{v}_B = \hat{\boldsymbol{v}}_B(q,\dot{q}) = [\dot{X}_\mathrm{c} - \frac{1}{2}\ell\,\dot{\theta}_1\sin\theta_1]\,\boldsymbol{e}_1 + [\frac{1}{2}\ell\dot{\theta}_1\cos\theta_1]\,\boldsymbol{e}_2, \tag{1.36b}$$

$$\boldsymbol{v}_M = \hat{\boldsymbol{v}}_M(q,\dot{q}) = [\dot{X}_\mathrm{c} - \ell\,\dot{\theta}_1\sin\theta_1]\,\boldsymbol{e}_1 + [\ell\,\dot{\theta}_1\cos\theta_1]\,\boldsymbol{e}_2, \tag{1.36c}$$

$$\boldsymbol{v}_C = \hat{\boldsymbol{v}}_C(q,\dot{q}) = [\dot{X}_\mathrm{c} - \ell\,\dot{\theta}_1\sin\theta_1 - \frac{1}{2}\ell\,\dot{\theta}_2\sin\theta_2]\,\boldsymbol{e}_1 + [\ell\dot{\theta}_1\cos\theta_1 + \frac{1}{2}\ell\,\dot{\theta}_2\cos\theta_2]\,\boldsymbol{e}_2, \tag{1.36d}$$

$$\boldsymbol{v}_D = \hat{\boldsymbol{v}}_D(q,\dot{q}) = [\dot{X}_\mathrm{c} - \ell\,\dot{\theta}_1\sin\theta_1 - \ell\,\dot{\theta}_2\sin\theta_2]\,\boldsymbol{e}_1 + [\ell\,\dot{\theta}_1\cos\theta_1 + \ell\,\dot{\theta}_2\cos\theta_2]\,\boldsymbol{e}_2. \tag{1.36e}$$

The presence of the wheel and the postulate on its motion impose a *nonholonomic constraint*: the velocity $\boldsymbol{v}_D$ of the end-point of $\mathscr{B}_2$ connected to the wheel is compelled to be at all times orthogonal to $\mathscr{B}_2$ (see [5] for details). In the considered reference frame, this constraint is described by the relation $\ell\,\boldsymbol{n}_2\cdot\boldsymbol{v}_D = 0$, which, in terms of the Lagrangian parameters, reads

$$\mathcal{C} \equiv \hat{\mathcal{C}}(q,\dot{q}) = \dot{\theta}_1\ell\sin(\theta_1-\theta_2) - \dot{X}_\mathrm{c}\cos\theta_2 = 0, \tag{1.37}$$

and is referred to as *"skate' constraint'* [5].

To simplify the analysis of the dynamics of the considered device, we prescribe that the mass of each bar is concentrated at its midpoint, that the cart can be modeled as a material point of mass m_c, and that the wheel's mass is negligible (*'massless wheel'* [5]). Moreover, we assume that the cart and $\mathscr{B}_1$ as well as $\mathscr{B}_1$ and $\mathscr{B}_2$ are connected to each other by means of viscoelastic spring-like elements of angular stiffness $k > 0$ and damping coefficient $c > 0$. Finally, a constant force of magnitude $F > 0$ (*'dead load'* [5]) is applied to the cart, while a *'follower force'* [5], generated by the nonholonomic constraint, acts on the skate parallel with the bar $\mathscr{B}_2$, as shown in Figure 1.4.

Under the assumptions above, the system admits the Lagrangian function [5]

$$\begin{aligned}\mathcal{L}_\mathrm{o} \equiv \hat{\mathcal{L}}_\mathrm{o}(q,\dot{q}) =& \frac{1}{2}[\frac{5}{4}m\ell^2\dot{\theta}_1^2 + \frac{1}{4}m\ell^2\dot{\theta}_2^2 + (2m+m_\mathrm{c})\dot{X}_\mathrm{c}^2] \\ &+ \frac{1}{2}m\ell^2\,\dot{\theta}_1\dot{\theta}_2\cos(\theta_2-\theta_1) - \frac{3}{2}m\ell\,\dot{\theta}_1\dot{X}_\mathrm{c}\sin\theta_1 - \frac{1}{2}m\ell\,\dot{\theta}_2\dot{X}_\mathrm{c}\sin\theta_2 \\ &- \frac{1}{2}k\,\theta_1^2 - \frac{1}{2}k(\theta_2-\theta_1)^2 + F\,X_\mathrm{c},\end{aligned} \tag{1.38}$$

which accounts for all interactions to which the system is subjected, with the exception of the damping and of the nonholonomic constraint (1.37). Following [5], damping is described through the Rayleigh dissipation function

$$\mathcal{R} = \hat{\mathcal{R}}(\dot{q}) = \frac{1}{2}c\,\dot{\theta}_1^2 + \frac{1}{2}c(\dot{\theta}_2-\dot{\theta}_1)^2, \tag{1.39}$$

which yields the dissipative forces

$$-\frac{\partial\hat{\mathcal{R}}}{\partial\dot{\theta}_1}(\dot{q}) = -c(2\dot{\theta}_1-\dot{\theta}_2), \qquad -\frac{\partial\hat{\mathcal{R}}}{\partial\dot{\theta}_2}(\dot{q}) = -c(\dot{\theta}_2-\dot{\theta}_1), \qquad -\frac{\partial\hat{\mathcal{R}}}{\partial\dot{X}_\mathrm{c}}(\dot{q}) = 0. \tag{1.40}$$

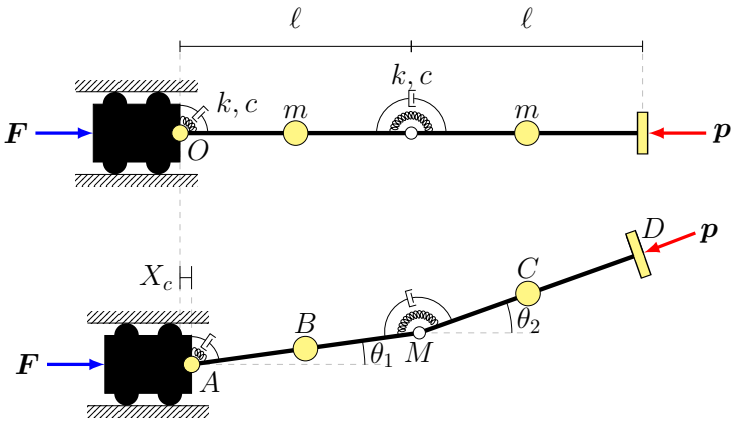

Figure 1.4: Sketch of the device introduced by Cazzolli et al. [5]. Upper part: the straight configuration ($\theta_1 = \theta_2 = 0$) with the cart located on the origin O, so that $X_\mathrm{c} = 0$. Lower part: a deformed configuration ($\theta_1 \neq 0, \theta_2 \neq 0$), with the cart positioned at a point differing from the origin ($X_\mathrm{c} \neq 0$). The hinges are characterized by an elastic stiffness $k > 0$ and a viscous damping coefficient $c > 0$. The reaction force $\boldsymbol{p}$ associated with the nonholonomic constraint (the 'wheel' or the 'skate') is directed along the axis of the bar $\mathscr{B}_2$.

The Lagrangian function $\mathcal{L}_\mathrm{o}$ defined by Equation (1.38) describes, up to the dissipative terms, the 'original' device (whence the subscript 'o') as it was conceived by Cazzolli et al. [5]. Thus, it features the external potential FX_c, but it does not depend explicitly on time.

To determine the equations of motion for the considered system, we apply the *Extended Hamilton Method*, following Lanczos [18],

$$\delta \int_{t_\mathrm{in}}^{t_\mathrm{fin}} \hat{\mathcal{L}}_\mathrm{o}(q,\dot{q})\,\mathrm{d}t = \int_{t_\mathrm{in}}^{t_\mathrm{fin}} \left(\sum_{\alpha=1}^{3} \frac{\partial \hat{\mathcal{R}}}{\partial \dot{q}_\alpha}(\dot{q}) \delta q_\alpha - \sum_{\alpha=1}^{3} \mu \frac{\partial \hat{\mathcal{C}}}{\partial \dot{q}_\alpha}(q,\dot{q})\,\delta q_\alpha \right) \mathrm{d}t, \tag{1.41}$$

where the integral on the left-hand side is referred to as *action functional*, t_in and t_fin denote an initial and a final instant of time, and the function of time μ on the right-hand side is a Lagrange multiplier introduced to account for the nonholonomic constraint (1.37), see [9, 18, 19, 20] for details.

The variation of the action functional, performed as predicted by Hamilton's Principle, and under the hypothesis $\delta q_\alpha(t_\mathrm{in}) = \delta q_\alpha(t_\mathrm{fin}) = 0$ for $k = 1, 2, 3$, leads to

$$\delta \int_{t_\mathrm{in}}^{t_\mathrm{fin}} \hat{\mathcal{L}}_\mathrm{o}(q,\dot{q})\,\mathrm{d}t = \int_{t_\mathrm{in}}^{t_\mathrm{fin}} \sum_{\alpha=1}^{3} (\mathcal{E}_\alpha \hat{\mathcal{L}}_\mathrm{o})\,\delta q_\alpha\,\mathrm{d}t, \tag{1.42}$$

with $\mathcal{E}_\alpha \hat{\mathcal{L}}_\mathrm{o}$ being the Euler–Lagrange operator applied to $\hat{\mathcal{L}}_\mathrm{o}$,

$$\mathcal{E}_\alpha \hat{\mathcal{L}}_\mathrm{o} \coloneqq \frac{\partial \hat{\mathcal{L}}_\mathrm{o}}{\partial q_\alpha}(q,\dot{q}) - \frac{\mathrm{d}}{\mathrm{d}t}\left(\frac{\partial \hat{\mathcal{L}}_\mathrm{o}}{\partial \dot{q}_\alpha}(q,\dot{q}) \right), \qquad \alpha = 1,2,3. \tag{1.43}$$

Then, the local form of Equation (1.41) reads

$$\mathcal{E}_\alpha \hat{\mathcal{L}}_\mathrm{o} - \frac{\partial \hat{\mathcal{R}}}{\partial \dot{q}_\alpha}(\dot{q}) + \mu \frac{\partial \hat{\mathcal{C}}}{\partial \dot{q}_\alpha}(q,\dot{q}) = 0, \qquad \alpha = 1,2,3. \tag{1.44}$$

The third term on the left-hand side of Equation (1.44) identifies, for $k = 1, 2, 3$, the Lagrangian components of the reaction force due to the constraint, which are given by

$$\mu \frac{\partial \hat{\mathcal{C}}}{\partial \dot{\theta}_1}(q, \dot{q}) = \mu \ell \sin(\theta_1 - \theta_2) \equiv \{\ell \hat{\boldsymbol{n}}_1(q) \times \hat{\boldsymbol{p}}(q)\} \cdot \boldsymbol{e}_3, \tag{1.45a}$$

$$\mu \frac{\partial \hat{\mathcal{C}}}{\partial \dot{\theta}_2}(q, \dot{q}) \equiv \{\ell \hat{\boldsymbol{n}}_2(q) \times \hat{\boldsymbol{p}}(q)\} \cdot \boldsymbol{e}_3 = 0, \tag{1.45b}$$

$$\mu \frac{\partial \hat{\mathcal{C}}}{\partial \dot{X}_\mathrm{c}}(q, \dot{q}) = -\mu \cos\theta_2 \equiv \hat{\boldsymbol{p}}(q) \cdot \boldsymbol{e}_1, \tag{1.45c}$$

where '$\times$' denotes the cross product and $\boldsymbol{p} = \hat{\boldsymbol{p}}(q) = -\mu \boldsymbol{n}_2$ is referred to as a *follower force* [5]. We notice that, in a generic configuration of the device, Equation (1.45a) is the (scalar) torque that the follower force exerts on $\mathscr{B}_1$ around the instantaneous position x_A of the point A. Similarly, Equation (1.45b) is the *null* (scalar) torque that $\boldsymbol{p}$ exerts on $\mathscr{B}_2$, since $\boldsymbol{p}$ is parallel to $\mathscr{B}_2$ by design. Moreover, Equation (1.45c) provides the $\boldsymbol{e}_1$-component of $\boldsymbol{p}$ acting on the cart.

1.3 The paradigmatic solenoid problem and the Maxwell–Lodge effect

The solenoid $\mathscr{S}$ has virtually infinite height, axis parallel with $\boldsymbol{e}_3$, and circular cross section $\mathscr{C}$ of radius R_s. An electric current flowing in the wire constituting the solenoid generates a magnetic field $\boldsymbol{H}$, which, given the magnetic permeability of the vacuum μ_0, yields the magnetic induction field $\boldsymbol{B} = \mu_0 \boldsymbol{H}$.

Assuming appropriate regularity, the magnetic induction field $\boldsymbol{B}$ and the electric field $\boldsymbol{E}$ must fulfill the equations

$$\mathrm{div}\boldsymbol{B} = 0 \qquad \text{and} \qquad \mathrm{curl}\boldsymbol{E} = -\partial_t \boldsymbol{B}, \tag{1.46}$$

which constitute two of the four Maxwell equations written in local form. These conditions permit to express $\boldsymbol{B}$ and $\boldsymbol{E}$ in terms of a vector potential $\boldsymbol{A}$ and of a scalar potential Φ —both at least of class C^2— through the relations $\boldsymbol{B} = \mathrm{curl}\boldsymbol{A}$ and $\boldsymbol{E} = -\mathrm{grad}\,\Phi - \partial_t \boldsymbol{A}$ (see, [21]). Because of the differential structure of these relations, the potentials $\boldsymbol{A}$ and Φ are not unique. Indeed, for any scalar field χ at least of class C^2, $\boldsymbol{B}$ and $\boldsymbol{E}$ remain invariant under transformations of the type

$$\boldsymbol{A} \mapsto \tilde{\boldsymbol{A}} = \boldsymbol{A} + \mathrm{grad}\,\chi, \qquad \Phi \mapsto \tilde{\Phi} = \Phi - \partial_t \chi, \tag{1.47}$$

known as *gauge transformations* [21]. The field χ is the *generator* of the gauge transformations and allows for obtaining new forms of the vector potential and of the scalar potential, therefore also referred to as *gauge potentials*. Although the ideal solenoid considered in this section constitutes a paradigmatic and widely studied physical problem, we review it to contextualize it within the mechanical framework of the device presented in Chapter 2. The solenoid problem is grounded on the fundamental hypothesis that the magnetic induction field $\boldsymbol{B}$ is non-null and homogeneous in the interior of $\mathscr{S}$ and identically null outside it, whence

$$\boldsymbol{B}(x,t) = B_\mathrm{h}(t)\,\boldsymbol{e}_3, \quad \text{for } x \in \mathrm{Int}(\mathscr{S}) \quad \text{and} \quad \boldsymbol{B}(x,t) = \boldsymbol{0}, \quad \text{for } x \in \mathbb{R}^3 \setminus \mathscr{S}, \tag{1.48}$$

where x is a spatial point of Cartesian coordinates (x_1, x_2, x_3), enumerated consistently with $\boldsymbol{e}_1$, $\boldsymbol{e}_2$, and $\boldsymbol{e}_3$, while $B_\mathrm{h}(t)$ is a prescribed function of time t [21].

We notice that the vanishing of $\boldsymbol{B}$ in the exterior of the solenoid is exact *'in the stationary regime'* [6], although it can be maintained also under the hypothesis that the current flowing in the solenoid *'varies slowly in time'* [6]. The latter condition is fundamental when introducing the Maxwell–Lodge effect

Within the so-called *temporal gauge* [22], which prescribes a vanishing scalar potential, the distribution of $\boldsymbol{B}$ given in Equation (1.48) and the relation $\boldsymbol{B} = \mathrm{curl}\boldsymbol{A}$ imply [21]

$$\boldsymbol{A}(x,t) = -\frac{1}{2}B_\mathrm{h}(t)x_2\,\boldsymbol{e}_1 + \frac{1}{2}B_\mathrm{h}(t)x_1\,\boldsymbol{e}_2, \qquad \Phi(x,t) = 0, \quad \text{in } \mathrm{Int}(\mathscr{S}), \tag{1.49a}$$

$$\boldsymbol{A}(x,t) = -\frac{1}{2}B_\mathrm{h}(t)R_\mathrm{s}^2\frac{x_2}{x_1^2+x_2^2}\,\boldsymbol{e}_1 + \frac{1}{2}B_\mathrm{h}(t)R_\mathrm{s}^2\frac{x_1}{x_1^2+x_2^2}\,\boldsymbol{e}_2, \quad \Phi(x,t) = 0, \quad \text{in } \mathbb{R}^3\setminus\mathscr{S}. \tag{1.49b}$$

Therefore, $\boldsymbol{A}$ is continuous on $\partial\mathscr{S}$. Moreover, it is divergence free both in the interior and in the exterior of the solenoid, since the equality $\mathrm{div}\boldsymbol{A} = 0$ is identically satisfied both in $\mathrm{Int}(\mathscr{S})$ and in $\mathbb{R}^3\setminus\mathscr{S}$, and it is irrotational outside the solenoid, since $\mathrm{curl}\boldsymbol{A} = \boldsymbol{0}$ in $\mathbb{R}^3\setminus\mathscr{S}$.

It is worth recalling that the Euclidean norm of $\boldsymbol{A}(x,t)$ reads

$$\|\boldsymbol{A}(x,t)\| = \frac{1}{2}|B_\mathrm{h}(t)|\sqrt{x_1^2+x_2^2} = \frac{1}{2}|B_\mathrm{h}(t)|\,\|\boldsymbol{r}(x)\|, \qquad \text{in } \mathrm{Int}(\mathscr{S}), \tag{1.50a}$$

$$\|\boldsymbol{A}(x,t)\| = \frac{1}{2}|B_\mathrm{h}(t)|R_\mathrm{s}^2\frac{1}{\sqrt{x_1^2+x_2^2}} = \frac{1}{2}|B_\mathrm{h}(t)|\frac{R_\mathrm{s}^2}{\|\boldsymbol{r}(x)\|}, \qquad \text{in } \mathbb{R}^3\setminus\mathscr{S}, \tag{1.50b}$$

with $\boldsymbol{r}(x) = x_1\boldsymbol{e}_1 + x_2\boldsymbol{e}_2$, thereby increasing linearly with $\varrho = \|\boldsymbol{r}(x)\|$ until $\varrho = R_\mathrm{s}$, and then decreasing asymptotically towards zero as ϱ^{-1} for $\varrho > R_\mathrm{s}$ [21, 6].

According to Equations (1.48), (1.49a), and (1.49b), for any open surface Σ with piecewise regular contour $\partial\Sigma$ lying on a plane that intersects transversely the solenoid, and either containing the cross section $\mathscr{C}$ of the solenoid or being equal to $\mathscr{C}$, the magnetic flux is

$$\Phi_\mathrm{M}(\Sigma;t) = \int_\Sigma \boldsymbol{B}(x,t)\cdot\boldsymbol{e}_3\,\mathrm{d}a(x) = \int_{\partial\Sigma}\boldsymbol{A}(x,t)\cdot\boldsymbol{\tau}(x)\,\mathrm{d}s(x) = B_\mathrm{h}(t)\pi R_\mathrm{s}^2, \tag{1.51}$$

where $\boldsymbol{\tau}(x)$ is the unit vector tangent to $\partial\Sigma$ at x. When Σ contains $\mathscr{C}$, the magnetic induction field $\boldsymbol{B}$ is null in $\Sigma\setminus\mathscr{C}$ and the first integral in Equation (1.51) reduces to a surface integral over $\mathscr{C}$, whence $\Phi_\mathrm{M}(\Sigma;t) = B_\mathrm{h}(t)\pi R_\mathrm{s}^2$, with $\pi R_\mathrm{s}^2 = \mathrm{Area}(\mathscr{C})$. Since $\Phi_\mathrm{M}(\Sigma;t)$ must be independent of $\Sigma \supseteq \mathscr{C}$, the magnetic flux can be obtained by directly computing the contour integral in Equation (1.51), with $\boldsymbol{A}$ given by Equation (1.49b) [21].

By employing Equations (1.49a) and (1.49b) for the calculation of the electric field within the *temporal gauge* ($\Phi = 0$), which implies $\boldsymbol{E} = -\mathrm{grad}\Phi - \partial_t\boldsymbol{A} = -\partial_t\boldsymbol{A}$, we obtain

$$\boldsymbol{E}(x,t) = \frac{1}{2}\dot{B}_\mathrm{h}(t)x_2\,\boldsymbol{e}_1 - \frac{1}{2}\dot{B}_\mathrm{h}(t)x_1\,\boldsymbol{e}_2, \qquad \text{in } \mathrm{Int}(\mathscr{S}), \tag{1.52a}$$

$$\boldsymbol{E}(x,t) = \frac{1}{2}\dot{B}_\mathrm{h}(t)R_\mathrm{s}^2\frac{x_2}{x_1^2+x_2^2}\,\boldsymbol{e}_1 - \frac{1}{2}\dot{B}_\mathrm{h}(t)R_\mathrm{s}^2\frac{x_1}{x_1^2+x_2^2}\,\boldsymbol{e}_2, \qquad \text{in } \mathbb{R}^3\setminus\mathscr{S}. \tag{1.52b}$$

Remark 3 (The Maxwell–Lodge effect)**.**
Equations (1.49b) *and* (1.52b) *evidence that the vector potential* $\boldsymbol{A}$ *and the electric field* $\boldsymbol{E} = -\partial_t\boldsymbol{A}$ *are non-null also outside the solenoid, where the magnetic induction field* $\boldsymbol{B}$

is null. This result has many important physical consequences, one of which is known as Maxwell–Lodge effect *[23]: by positioning a coil of given electric conductivity around the solenoid, but not in contact with it, an electric current flowing in this coil is observed in response to the electromotive force generated by the negative of the time derivative of the magnetic flux* $B_\mathrm{h}(t)\pi R_\mathrm{s}^2$*, due to* $\boldsymbol{B}$ *inside the solenoid [6]. While this result is exactly the Faraday–Neumann–Lenz law, with the electromotive force being* $\mathscr{E}(t) \coloneqq \int_{\partial\Sigma} \boldsymbol{E}(x,t) \cdot \boldsymbol{\tau}(x)\,\mathrm{d}s(x) = -\dot{B}_\mathrm{h}(t)\pi R_\mathrm{s}^2$*, and* $\partial\Sigma$ *representing the coil —assumed filiform—, the fact that the current in the coil occurs in the region of space in which the magnetic flux is null (but* $\boldsymbol{E} = -\partial_t \boldsymbol{A}$ *is non-null) constitutes the essence of the Maxwell–Lodge effect. This has generated considerable debate aiming at clarifying the role and intrinsic meaning of the vector potential* $\boldsymbol{A}$ *in classical physics.*

On the basis of well documented results on the gauge transformations presented in Equation (1.47) [21], one can choose the generators

$$\chi(x,t) = \frac{1}{2} B_\mathrm{h}(t) x_1 x_2, \qquad \text{in } \mathrm{Int}(\mathscr{S}), \tag{1.53a}$$

$$\chi(x,t) = \frac{1}{2} B_\mathrm{h}(t) R_\mathrm{s}^2 \arctan(x_1/x_2), \qquad \text{in } \mathbb{R}^3 \setminus \mathscr{S} \text{ and for } x_2 \neq 0, \tag{1.53b}$$

thereby moving out from the temporal gauge and switching to the transformed gauge potentials

$$\tilde{\boldsymbol{A}}(x,t) = B_\mathrm{h}(t) x_1\, \boldsymbol{e}_2, \quad \tilde{\Phi}(x,t) = -\frac{1}{2}\dot{B}_\mathrm{h}(t) x_1 x_2, \qquad \text{in } \mathrm{Int}(\mathscr{S}), \tag{1.54a}$$

$$\tilde{\boldsymbol{A}}(x,t) = \boldsymbol{0}, \qquad \tilde{\Phi}(x,t) = -\frac{1}{2}\dot{B}_\mathrm{h}(t) R_\mathrm{s}^2 \arctan(x_1/x_2), \quad \text{in } \mathbb{R}^3 \setminus \mathscr{S} \text{ and for } x_2 \neq 0 \tag{1.54b}$$

(note that χ has null Laplacian in the region in which it is defined). The new gauge potentials, however, yield exactly the same Lorentz forces as those reported in Equations (2.1) and (2.2), with the only (irrelevant) technical difference being that $\boldsymbol{B}$ and $\boldsymbol{E}$ are now to be computed as $\boldsymbol{B} = \mathrm{curl}\tilde{\boldsymbol{A}}$ and $\boldsymbol{E} = -\mathrm{grad}\,\tilde{\Phi} - \partial_t \tilde{\boldsymbol{A}}$. In particular, outside the solenoid, $\boldsymbol{E} = -\mathrm{grad}\,\tilde{\Phi}$ holds at all points $x \in \mathbb{R}^3 \setminus \mathscr{S}$ such that $x_2 \neq 0$. Therefore, for any open surface $\Sigma \supset \mathscr{C}$ having piecewise regular contour $\partial\Sigma$, $\boldsymbol{E}$ is undefined at both points in which $\partial\Sigma$ intersects the x_1-axis. However, since these two points constitute a set of null measure, the electromotive force $\mathscr{E}(t) = -\int_{\partial\Sigma} \mathrm{grad}\,\tilde{\Phi}(x,t) \cdot \boldsymbol{\tau}(x)\,\mathrm{d}s(x)$ remains unchanged and delivers $-\dot{B}_\mathrm{h}(t)\pi R_\mathrm{s}^2$, as is the case of the temporal gauge.

Chapter 2

Charged Ziegler's double pendulum

In this chapter, the constrained version of Ziegler's double pendulum is considered, and placed both inside and outside an ideal solenoid. The static equilibrium is determined and a bifurcation analysis is performed. The post-critical behavior of the system is then examined in the context of soft-bodied micro-robotic applications in biology. The text and equations consolidating this chapter are taken from [1]

2.1 Introduction

The double pendulum is a mechanical device that, because of its simplicity, is often employed to exemplify more complicated structures, which appear in various mechanical contexts, ranging from different branches of engineering [24, 25] to robotics [5, 26], and biomechanics [27].

One variant of the double pendulum is Ziegler's double pendulum [4], constructed by two homogeneous and rigid bars, of equal length ℓ and equal mass m, connected one to the other via a hinge. The masses of the bars are considered to be concentrated at their midpoints. One of the two bars is hinged on a fixed frame, and the other is subjected to a force directed in parallel to it, known as a follower force. Moreover, the hinges are regarded as viscoelastic, with angular stiffness $k > 0$, and damping $c > 0$. These coefficients lump the viscoelastic properties of the structure into the joints connecting the double pendulum to the fixed frame and the two bars to each other [7, 4]. An important feature of Ziegler's double pendulum is that it can exhibit flutter instability due to the non-conservative nature of the follower force [4, 8, 14, 15, 25].

Cazzolli et al. [5] introduced a modification of Ziegler's double pendulum that reproduces the same bifurcation and instability landscape as the original structure, but *under a conservative load*. In particular, one end of the first bar is pinned to a moving cart (Figure 1.4); at the tip of the second bar, a nonholonomic constraint enforces orthogonality between the tip velocity and the bar. This system is designed in a way that it can allow a translational motion of the cart, when the latter is loaded with a dead force, possible through an oscillatory motion of the arms of the pendulum, a dynamics resembling those of a certain family of microrobots or micro-structures used in biomechanics [27, 28, 29, 30, 31]. One example of these microrobots is provided by a *'magnetic flexible filament attached to a red blood cell'*,

as presented by Dreyfus et al. [32], where the dead load plays the role of the propulsion thrust in aqueous environment at low Reynolds numbers. This device prompted the present investigation of analogous systems in microrobotics through a generalization of the loads considered in [5].

Microrobots for biomedical or biomechanical applications are often susceptible to electromagnetic interactions, because they feature magnetized [29, 30, 32] or electrically polarized parts [33]. Therefore, also Lorentz-type forces contribute to determine the overall dynamics of such devices in addition to self-propulsion [28] or other stimuli [27].

Despite its fundamental role in physics, certain foundational aspects of electromagnetism have remained the subject of debate until recently. This applies, for instance, to the true role and *'physical meaning'* [6] within classical electromagnetism of the vector potential $\boldsymbol{A}$, by which the magnetic induction field $\boldsymbol{B}$ is expressed as $\boldsymbol{B} = \mathrm{curl}\boldsymbol{A}$. Indeed, whereas the electric and the magnetic fields both have 'tangible' meaning, the vector potential works 'behind the scenes' of the classical theory of electromagnetism. This issue has been thoroughly investigated in a work by Rousseaux et al. [6], who conclude that there exist effects which cannot be understood *'without the intervention of'* $\boldsymbol{A}$ [6]. As an example for pursuing their goals, Rousseaux et al. [6] took the paradigmatic problem of the ideal solenoid to unveil the Maxwell–Lodge effect [23]. This phenomenon predicts that a current is generated in a wire wound around the solenoid in response to the electric field induced outside it by the variation in time of the vector potential (not of the magnetic induction field, which is zero outside the ideal solenoid). Although the purpose of this work is not to address the intricacies of the debate surrounding the vector potential, we embrace the viewpoint of Rousseaux et al. [6] and apply it to our mechanical device.

In light of the above considerations, the device investigated here can be regarded as a model of an electrically charged microrobot, with dimensions comparable to those of eukaryotic cells. It consists of a continuous viscoelastic rod attached to a small mass and is subjected to the Lorentz force generated by a solenoid [27, 28, 29, 30, 31]. The rod is idealized as a viscoelastic double pendulum, following the approach of Cazzolli et al. [5]. Compared to that approach, two substantial differences are introduced: (i) the dead load is interpreted as a self-propulsion force; (ii) the device carries a concentrated electric charge located in the structural element imposing the nonholonomic constraint (similar problems were formulated by Maruskin et al. [34] and Pastore et al. [35]).

Within this setting, the main objectives of our work are twofold:

1. We aim to assess the extent to which the Lorentz force modifies the results reported by Cazzolli et al. [5] concerning stability, the onset of a Hopf bifurcation, and the overall dynamical behavior of the device.

2. We revisit the Maxwell–Lodge effect [6] by placing it in the mechanical context of the device under study. More specifically, we show that our theoretical framework predicts a Lorentz force on the charged structural element, even when it is located outside the solenoid. This result is achieved by placing the device first inside and then outside the solenoid. This may provide a potential–albeit presently theoretical–experimental setup to detect the Maxwell–Lodge effect, based on microrobotics and serving as an alternative to the experiment by Rousseaux et al. [6].

2.2 Charged Ziegler's double-pendulum interacting with Lorentz force

With reference to the mechanical system described in section 1.2 of the previous chapter and, in particular, to the Lagrangian function reported in Equation (1.38), we introduce here two *major modifications*:

(1) The massless wheel, concentrated at the geometric point D (see Figure 1.4), carries *electric charge* $\mathfrak{e} \neq 0$ (it will be assumed $\mathfrak{e} > 0$ in the following);

(2) A solenoid $\mathscr{S}$ as described in detail in Section 1.3, with radius much larger than ℓ, is considered. Two separate cases are then analyzed: the device is placed in the interior of the solenoid (*Case I*); the device is placed in the exterior of the solenoid (*Case II*).

The reader is referred to Figure 2.1 for a graphical representation device in the presence of the solenoid, where (1.52a) and (1.52b) then permit to exert a Lorentz force on the charged skate placed at the end-point D of the bar $\mathscr{B}_2$ of the device. This Lorentz force reads differently for when the device is considered to be inside or outside the solenoid, and it can be evaluated for each of the cases as follows:

Case I: Device inside the solenoid If the cross section of the solenoid is big enough to host the device, and if it is assumed that the motion of the device remains confined to this cross section, so that the skate does not transit through the lateral boundary of the solenoid, then the Lorentz force acting on the skate in $\mathrm{Int}(\mathscr{S})$ reads

$$\begin{aligned}\boldsymbol{F}_{\mathrm{L}}(x_D(t),t) =& \mathfrak{e}\left[\boldsymbol{E}(x_D(t),t) + \boldsymbol{v}_D(t) \times \boldsymbol{B}(x_D(t),t)\right] \\ =& \left(\frac{\mathfrak{e}\dot{B}_{\mathrm{h}}(t)}{2}\, x_{D2}(t) + \mathfrak{e}B_{\mathrm{h}}(t)\dot{x}_{D2}(t)\right)\boldsymbol{e}_1 - \left(\frac{\mathfrak{e}\dot{B}_{\mathrm{h}}(t)}{2}\, x_{D1}(t) + \mathfrak{e}B_{\mathrm{h}}(t)\dot{x}_{D1}(t)\right)\boldsymbol{e}_2,\end{aligned} \tag{2.1}$$

meaning that it consists both of an electric and of a magnetic contribution. Note that the fields $\boldsymbol{E}$ and $\boldsymbol{B}$ are defined at all spatial points, and, consequently, they couple dynamically with the system through their evaluation at time t and at the spatial point $x = x_D(t)$ occupied by the material point D at the same time.

For this reason, the Lorentz force is evaluated at $x = x_D(t)$, with velocity $\boldsymbol{v}_D(t)$ at time t. The same considerations apply to the vector potential $\boldsymbol{A}$.

Case II: Device outside the solenoid The nontrivial electric field present also in the exterior of the solenoid, as given by Equation (1.52b), generates a Lorentz force acting on the charged skate, even in the case in which the skate is located outside the solenoid. In this setting, the Lorentz force in $\mathbb{R}^3 \setminus \mathscr{S}$ reads

$$\begin{aligned}\boldsymbol{F}_{\mathrm{L}}(x_D(t),t) &= \mathfrak{e}\,\boldsymbol{E}(x_D(t),t) \\ &= \frac{\mathfrak{e}\dot{B}_{\mathrm{h}}(t)R_{\mathrm{s}}^2}{2}\frac{x_{D2}(t)}{[x_{D1}(t)]^2 + [x_{D2}(t)]^2}\,\boldsymbol{e}_1 - \frac{\mathfrak{e}\dot{B}_{\mathrm{h}}(t)R_{\mathrm{s}}^2}{2}\frac{x_{D1}(t)}{[x_{D1}(t)]^2 + [x_{D2}(t)]^2}\,\boldsymbol{e}_2.\end{aligned} \tag{2.2}$$

Here the Maxwell–Lodge effect manifests itself also in the dynamics of the charged Ziegler double pendulum in Case II, when the pendulum is placed outside the solenoid. Indeed, because of the electric charge $\mathfrak{e}$ is concentrated at the point D of the device, this point is

subject to the Lorentz force $\boldsymbol{F}_{\mathrm{L}}(x_D(t),t)$ as prescribed by Equation (2.2) when the device is in $\mathbb{R}^3 \setminus \mathscr{S}$. In turn, $\boldsymbol{F}_{\mathrm{L}}(x_D(t),t)$ influences the dynamics of the device and interacts with the dead load F applied to the cart, at least until the device exceeds a certain distance from the solenoid's boundary, beyond which the amplitude of $\boldsymbol{F}_{\mathrm{L}}(x_D(t),t)$, decreasing radially as $\{[x_{D1}(t)]^2 + [x_{D2}(t)]^2\}^{-1/2}$, becomes negligible compared to the dead load F.

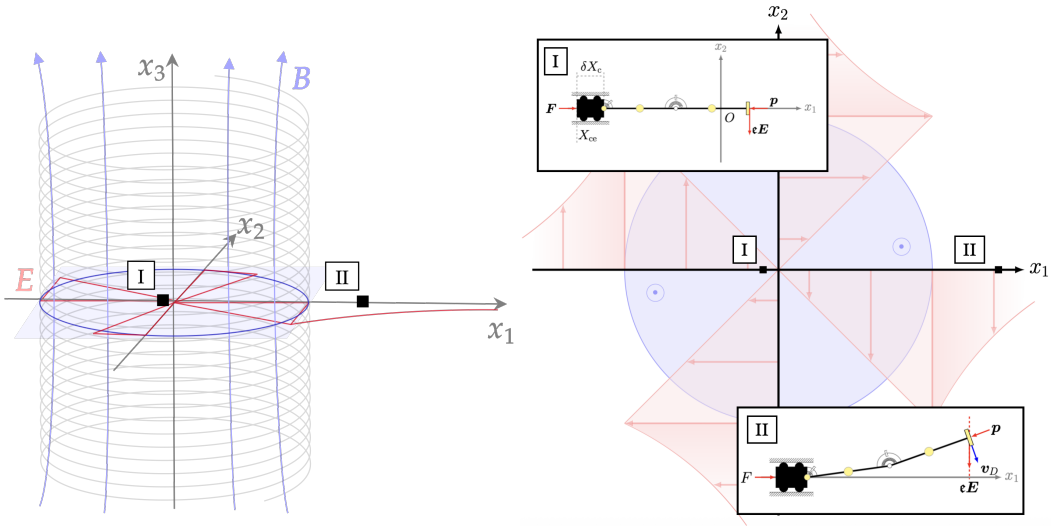

Figure 2.1: Sketch of the solenoid, illustrating the electric field $\boldsymbol{E}$ (red) and the magnetic induction field $\boldsymbol{B}$ (blue). The system is shown both in a three-dimensional perspective and in a vertical cross-section, with the device positions for Case I and Case II indicated in both views. In the position referring to Case I, $\Delta X_{\mathrm{c}} := X_{\mathrm{c}0} - X_{\mathrm{ce}}$, with $X_{\mathrm{c}0}$ being the initial position of the cart. The images correspond to assuming $B_{\mathrm{h}}(t) > 0$ and $\dot{B}_{\mathrm{h}}(t) > 0$. In the zoomed-in image referring to Case II, $\mathfrak{e}\boldsymbol{E}$ is directed tangentially to the circumference centered in O and passing through D, but it can be regarded as approximately parallel to the x_2-axis because the device is placed at a relatively long distance from O.

2.2.1 The Lagrangian function of the charged Ziegler double pendulum

The Lagrangian function of the device subjected to the additional magnetic interaction is obtained from the Lagrangian function $\mathcal{L}_{\mathrm{o}}$ in Equation (1.38) by adding the generalized, velocity-dependent potential $\mathfrak{e}\boldsymbol{A}(x_D(t),t)\cdot\boldsymbol{v}_D(t)$, in which $\boldsymbol{A}$ is evaluated at time t and at the spatial point $x_D(t)$ that is instantaneously occupied by the moving charge at time t [21, 35]. In terms of the system's Lagrangian parameters and generalized velocities, this yields (see also [34] for the case of the *'knife edge with a dipole moment in a magnetic field'*)

$$\mathcal{L} \equiv \hat{\mathcal{L}}(q,\dot{q},t) = \hat{\mathcal{L}}_{\mathrm{o}}(q,\dot{q}) + \mathfrak{e}[\mathcal{A}_1(q,t)\dot{\theta}_1 + \mathcal{A}_2(q,t)\dot{\theta}_2 + \mathcal{A}_3(q,t)\dot{X}_{\mathrm{c}}], \tag{2.3}$$

where, for $\beta = 1, 2, 3$, the functions $\mathcal{A}_\beta(q,t) = \frac{1}{2} B_\mathrm{h}(t) \mathcal{U}_\beta(q) \ell^2$ express explicitly how the device interacts with the vector potential and are defined by the auxiliary quantities

$$\mathcal{U}_1(q) \coloneqq \begin{cases} 1 + \cos(\theta_2 - \theta_1) + (X_\mathrm{c}/\ell)\cos\theta_1 & \text{Case I} \\ \dfrac{R_\mathrm{s}^2}{\ell^2} \dfrac{1 + \cos(\theta_2 - \theta_1) + (X_\mathrm{c}/\ell)\cos\theta_1}{[\cos\theta_1 + \cos\theta_2 + (X_\mathrm{c}/\ell)]^2 + [\sin\theta_1 + \sin\theta_2]^2} & \text{Case II} \end{cases} \tag{2.4a}$$

$$\mathcal{U}_2(q) \coloneqq \begin{cases} 1 + \cos(\theta_2 - \theta_1) + (X_\mathrm{c}/\ell)\cos\theta_2 & \text{Case I} \\ \dfrac{R_\mathrm{s}^2}{\ell^2} \dfrac{1 + \cos(\theta_2 - \theta_1) + (X_\mathrm{c}/\ell)\cos\theta_2}{[\cos\theta_1 + \cos\theta_2 + (X_\mathrm{c}/\ell)]^2 + [\sin\theta_1 + \sin\theta_2]^2} & \text{Case II} \end{cases} \tag{2.4b}$$

$$\mathcal{U}_3(q) \coloneqq \begin{cases} -\dfrac{\sin\theta_1 + \sin\theta_2}{\ell} & \text{Case I} \\ -\dfrac{R_\mathrm{s}^2}{\ell^3} \dfrac{\sin\theta_1 + \sin\theta_2}{[\cos\theta_1 + \cos\theta_2 + (X_\mathrm{c}/\ell)]^2 + [\sin\theta_1 + \sin\theta_2]^2} & \text{Case II} \end{cases} \tag{2.4c}$$

More in detail, it can be shown that, both in Case I and in Case II, the following identifications apply:

$$\mathcal{A}_1(q(t),t) = [\ell \boldsymbol{n}_1(t) \times \boldsymbol{A}(x_D(t),t)] \cdot \boldsymbol{e}_3, \tag{2.5a}$$
$$\mathcal{A}_2(q(t),t) = [\ell \boldsymbol{n}_2(t) \times \boldsymbol{A}(x_D(t),t)] \cdot \boldsymbol{e}_3, \tag{2.5b}$$
$$\mathcal{A}_3(q(t),t) = \boldsymbol{A}(x_D(t),t) \cdot \boldsymbol{e}_1. \tag{2.5c}$$

We remark that the vector potential $\boldsymbol{A}$, although having only two nonzero components, generates the three nonzero components $\mathcal{A}_1$, $\mathcal{A}_2$, and $\mathcal{A}_3$, with the first two being conjugate to the angular velocities of the bars $\dot\theta_1$ of $\dot\theta_2$, and the last one being conjugate to the linear velocity $\dot X_\mathrm{c}$ of the cart along the $\boldsymbol{e}_1$-axis. In addition, functions $\mathcal{A}_1$, $\mathcal{A}_2$, and $\mathcal{A}_3$, defined in Equations (2.4a)–(2.4c) and further explained in Equations (2.5a)–(2.5c), describe how the vector potential couples at each instant of time t with the configuration $q(t)$ assumed by the system as a whole at time t.

We emphasize that, the charge of the skate is assumed to be sufficiently weak so that the magnetic and the electric fields that it generates can be neglected.

A major difference with respect to the work by Cazzolli et al. [5] is that, in addition to the dead load applied to the cart, the system is also subjected to the *Lorentz force* $\boldsymbol{F}_\mathrm{L}(x_D(t),t)$, which assumes the expression given in Equation (2.1) or in Equation (2.2), depending on whether the device is inside or outside the solenoid, respectively.

In Case I, and when $\boldsymbol{A}$ does not depend explicitly on time, the Lorentz force reduces to $\boldsymbol{F}_\mathrm{L}(x_D(t),t) = \mathfrak{e}\, \boldsymbol{v}_D(t) \times \boldsymbol{B}(x_D(t))$ and, because of the constraint (1.37), it remains parallel with the bar $\mathscr{B}_2$, and thus with the follower force $\boldsymbol{p} = -\mu \boldsymbol{n}_2$, at all times. In addition, the Lorentz force vanishes whenever $\boldsymbol{v}_D(t)$ is null.

In Case II, the Lorentz force features solely the purely electric contribution, which is due to the explicit time dependence of $\boldsymbol{A}$, that is, $\boldsymbol{F}_\mathrm{L}(x_D(t),t) = \mathfrak{e}\boldsymbol{E}(x_D(t),t) = -\mathfrak{e}\, \partial_t \boldsymbol{A}(x_D(t),t)$. Therefore, if $\boldsymbol{A}$ is assumed to not be explicitly dependent on time, then the Lorentz force vanishes identically.

2.2.2 Dynamic equations

If the dynamic equations (1.44), featuring the Lagrangian function $\hat{\mathcal{L}}_{\mathrm{o}}$, are written explicitly, they lead to the set of equations presented by Cazzolli et al. [5]. In our framework, however, since electromagnetic interactions are considered, the dynamic equations follow from the Lagrangian function $\hat{\mathcal{L}}$ expressed in Equation (2.3). They read

$$\mathscr{E}_\alpha \hat{\mathcal{L}} - \frac{\partial \hat{\mathcal{R}}}{\partial \dot{q}_\alpha}(\dot{q}) + \mu \frac{\partial \hat{\mathcal{C}}}{\partial \dot{q}_\alpha}(q, \dot{q}) = 0, \qquad \alpha = 1, 2, 3, \tag{2.6}$$

where, as in Equation (1.44), the contributions $-\partial_{\dot{q}_\alpha} \hat{\mathcal{R}}(\dot{q})$ and $\mu\, \partial_{\dot{q}_\alpha} \hat{\mathcal{C}}(q, \dot{q})$ identify the dissipative generalized forces associated with damping and the reaction forces due to the nonholonomic *'skate constraint'* [5], respectively.

Before deriving the new Euler–Lagrange equations, we notice that the Euler–Lagrange operator applied to $\hat{\mathcal{L}}$ produces

$$\mathscr{E}_\alpha \hat{\mathcal{L}} = \mathscr{E}_\alpha \hat{\mathcal{L}}_{\mathrm{o}} + \mathfrak{e} \sum_{\beta=1}^{3} \mathcal{F}_{\alpha\beta}\, \dot{q}_\beta + \mathfrak{e}\, \mathcal{E}_\alpha, \qquad \alpha = 1, 2, 3, \tag{2.7}$$

where the quantities $\mathcal{F}_{\alpha\beta}$ and $\mathcal{E}_\alpha$ are defined as

$$\mathcal{F}_{\alpha\beta} \coloneqq \frac{\partial \mathcal{A}_\beta}{\partial q_\alpha} - \frac{\partial \mathcal{A}_\alpha}{\partial q_\beta}, \qquad \mathcal{E}_\alpha \coloneqq -\frac{\partial \mathcal{A}_\alpha}{\partial t} \qquad \alpha, \beta = 1, 2, 3, \tag{2.8}$$

and represent, in terms of the Lagrangian parameters selected, the components of the *generalized Faraday tensor* and of the *generalized electric field*, respectively. From the discussion in Section 1.3, in which the electric and the magnetic contributions of the Lorentz force have been analyzed in Cartesian coordinates, it follows that the magnetic contribution is active only in the interior of the solenoid. Accordingly, the equations of motion either include or exclude the magnetic contribution of the Lorentz force, depending on whether the device is located inside or outside the solenoid (Case I and Case II, respectively). Since this result must be consistently described when the device is analyzed in terms of the components of the generalized Faraday tensor and of the generalized electric field, defined by Equation (2.7), the quantities $\mathcal{F}_{\alpha\beta}$ must vanish identically in Case II, when the device moves outside the solenoid.

Specifically, the generalized Faraday tensor has components

$$\mathcal{F}_{12} = -\ell^2 B_{\mathrm{h}}(t) \sin(\theta_1 - \theta_2), \quad \mathcal{F}_{13} = -\ell B_{\mathrm{h}}(t) \cos\theta_1, \quad \mathcal{F}_{23} = -\ell B_{\mathrm{h}}(t) \cos\theta_2, \quad \text{Case I} \tag{2.9a}$$

$$\mathcal{F}_{12} = 0, \qquad \mathcal{F}_{13} = 0, \qquad \mathcal{F}_{23} = 0, \qquad \text{Case II} \tag{2.9b}$$

with $\mathcal{F}_{\alpha\beta} = -\mathcal{F}_{\beta\alpha}$ for $\alpha, \beta = 1, 2, 3$, while the generalized electric field has components

$$\mathcal{E}_\alpha \equiv -\partial_t \mathcal{A}_\alpha = -\frac{1}{2} \dot{B}_{\mathrm{h}}(t) \mathcal{U}_\alpha(q) \ell^2, \quad \alpha = 1, 2, 3, \tag{2.10}$$

where functions $\mathcal{U}_\alpha(q)$ are given in Equations (2.4a)–(2.4c), depending on whether Case I or Case II is considered.

Finally, upon introducing the components of the generalized Lorentz force

$$\mathfrak{F}_{\mathrm{L}\alpha} \coloneqq \mathfrak{e} \sum_{\beta=1}^{3} \mathcal{F}_{\alpha\beta}\, \dot{q}_\beta + \mathfrak{e}\, \mathcal{E}_\alpha, \quad \alpha = 1, 2, 3, \tag{2.11}$$

the dynamic equations (2.6) read

$$\mathscr{E}_\alpha \hat{\mathcal{L}}_{\mathrm{o}} - \frac{\partial \hat{\mathcal{R}}}{\partial \dot{q}_\alpha}(\dot{q}) + \mu \frac{\partial \hat{\mathcal{C}}}{\partial \dot{q}_\alpha}(q, \dot{q}) + \mathfrak{F}_{\mathrm{L}\alpha} = 0, \qquad \alpha = 1, 2, 3, \tag{2.12}$$

and, in explicit form, they become

$$\begin{aligned} &\frac{5}{4} m\ell^2 \ddot{\theta}_1 + \frac{1}{2} m\ell^2 \cos(\theta_1 - \theta_2)\ddot{\theta}_2 - \frac{3}{2} m\ell(\sin\theta_1)\ddot{X}_{\mathrm{c}} + \frac{1}{2} m\ell^2 \sin(\theta_1 - \theta_2)\dot{\theta}_2^2 \\ &= -k(2\theta_1 - \theta_2) - c(2\dot{\theta}_1 - \dot{\theta}_2) + \mu\ell \sin(\theta_1 - \theta_2) + \mathfrak{F}_{\mathrm{L}1}, \end{aligned} \tag{2.13a}$$

$$\begin{aligned} &\frac{1}{2} m\ell^2 \cos(\theta_1 - \theta_2)\ddot{\theta}_1 + \frac{1}{4} m\ell^2 \ddot{\theta}_2 - \frac{1}{2} m\ell(\sin\theta_2)\ddot{X}_{\mathrm{c}} - \frac{1}{2} m\ell^2 \sin(\theta_1 - \theta_2)\dot{\theta}_1^2 \\ &= -k(\theta_2 - \theta_1) - c(\dot{\theta}_2 - \dot{\theta}_1) + \mathfrak{F}_{\mathrm{L}2}, \end{aligned} \tag{2.13b}$$

$$\begin{aligned} &-\frac{3}{2} m\ell(\sin\theta_1)\ddot{\theta}_1 - \frac{1}{2} m\ell(\sin\theta_2)\ddot{\theta}_2 + M\ddot{X}_{\mathrm{c}} - \frac{3}{2} m\ell(\cos\theta_1)\dot{\theta}_1^2 - \frac{1}{2} m\ell(\cos\theta_2)\dot{\theta}_2^2 \\ &= -\mu\cos\theta_2 + F + \mathfrak{F}_{\mathrm{L}3}. \end{aligned} \tag{2.13c}$$

where, together with the total mass $M \coloneqq 2m + m_{\mathrm{c}}$, the explicit expressions for the generalized components of the Lorentz force are introduced:

$$\mathfrak{F}_{\mathrm{L}1} = \begin{cases} -\frac{1}{2}\mathfrak{e}\dot{B}_{\mathrm{h}}(t)\mathcal{U}_1(q)\ell^2 - \mathfrak{e}B_{\mathrm{h}}(t)[\sin(\theta_1 - \theta_2)\dot{\theta}_2 + (\cos\theta_1)(\dot{X}_{\mathrm{c}}/\ell)]\ell^2 & \text{Case I} \\ -\frac{1}{2}\mathfrak{e}\dot{B}_{\mathrm{h}}(t)\mathcal{U}_1(q)\ell^2 & \text{Case II,} \end{cases} \tag{2.14a}$$

$$\mathfrak{F}_{\mathrm{L}2} = \begin{cases} -\frac{1}{2}\mathfrak{e}\dot{B}_{\mathrm{h}}(t)\mathcal{U}_2(q)\ell^2 + \mathfrak{e}B_{\mathrm{h}}(t)[\sin(\theta_1 - \theta_2)\dot{\theta}_1 - (\cos\theta_2)(\dot{X}_{\mathrm{c}}/\ell)]\ell^2 & \text{Case I} \\ -\frac{1}{2}\mathfrak{e}\dot{B}_{\mathrm{h}}(t)\mathcal{U}_2(q)\ell^2 & \text{Case II,} \end{cases} \tag{2.14b}$$

$$\mathfrak{F}_{\mathrm{L}3} = \begin{cases} -\frac{1}{2}\mathfrak{e}\dot{B}_{\mathrm{h}}(t)\mathcal{U}_3(q)\ell^2 + \mathfrak{e}B_{\mathrm{h}}(t)[(\cos\theta_1)\dot{\theta}_1 + (\cos\theta_2)\dot{\theta}_2]\ell & \text{Case I} \\ -\frac{1}{2}\mathfrak{e}\dot{B}_{\mathrm{h}}(t)\mathcal{U}_3(q)\ell^2 & \text{Case II.} \end{cases} \tag{2.14c}$$

We emphasize that the magnetic part of the generalized force component in Equation (2.14b) is zero also in Case I since the terms in square brackets return the constraint (1.37). This is because the magnetic part of the Lorentz force $\mathfrak{e}[\boldsymbol{v}_D \times \boldsymbol{B}]$ is parallel with the bar of unit vector $\boldsymbol{n}_2$ and also with the follower force, as explained at the end of Section 1.2.

Equations (2.13a)–(2.13c) are to be solved together with the constraint (1.37), which we differentiate with respect to time and turn into the second-order differential equation

$$-\ell\sin(\theta_1 - \theta_2)\ddot{\theta}_1 + (\cos\theta_2)\ddot{X}_{\mathrm{c}} = \dot{\theta}_2\dot{X}_{\mathrm{c}}\sin\theta_2 + \ell\dot{\theta}_1\cos(\theta_1 - \theta_2)(\dot{\theta}_1 - \dot{\theta}_2). \tag{2.15}$$

Equation (2.15), obtained by changing sign to the time derivative of Equation (1.37), is necessary to apply Schur's complement technique to the system (2.13a)–(2.13c) and (2.15) (see [35, 36] for details; the sign change is motivated by convenience in the construction of the Schur matrix).

Alongside the elastic and viscous forces featuring in the right-hand sides of Equations (2.13a)–(2.13c), the additional generalized Lorentz forces $\mathfrak{F}_{\mathrm{L}1}$, $\mathfrak{F}_{\mathrm{L}2}$ and $\mathfrak{F}_{\mathrm{L}3}$ are present, and,

coherently with Equations (1.45a)–(1.45c), the following identifications apply

$$\mathfrak{F}_{\mathrm{L}1} = [\ell \boldsymbol{n}_1(t) \times \boldsymbol{F}_{\mathrm{L}}(x_D(t), t)] \cdot \boldsymbol{e}_3, \tag{2.16a}$$

$$\mathfrak{F}_{\mathrm{L}2} = [\ell \boldsymbol{n}_2(t) \times \boldsymbol{F}_{\mathrm{L}}(x_D(t), t)] \cdot \boldsymbol{e}_3, \tag{2.16b}$$

$$\mathfrak{F}_{\mathrm{L}3} = \boldsymbol{F}_{\mathrm{L}}(x_D(q), t) \cdot \boldsymbol{e}_1. \tag{2.16c}$$

Equations (2.16a) and (2.16b) are the torques generated by the Lorentz force acting on the bars $\mathscr{B}_1$ and $\mathscr{B}_2$, respectively, while Equation (2.16c) is the component of the Lorentz force acting on the cart.

2.2.3 Determination of static equilibrium

To study the static equilibrium of the system, we consider an initial instant of time t_0 at which the system occupies the configuration $q(t_0) = q_0$, with null velocity $\dot{q}(t_0)$, and, for $t > t_0$, we look for solutions to Equations (2.13a)–(2.13c) of the type $q(t) = q_{\mathrm{e}} := (\theta_{1\mathrm{e}}, \theta_{2\mathrm{e}}, X_{\mathrm{ce}}) \equiv q_0$, satisfying $\dot{q}(t) = (0, 0, 0)$ and

$$-\mu_{\mathrm{e}} \ell \sin(\theta_{1\mathrm{e}} - \theta_{2\mathrm{e}}) = -\frac{1}{2} \mathfrak{e} \dot{B}_{\mathrm{h}}(t) \mathcal{U}_1(q_{\mathrm{e}}) \ell^2 - k(2\theta_{1\mathrm{e}} - \theta_{2\mathrm{e}}), \tag{2.17a}$$

$$0 = -\frac{1}{2} \mathfrak{e} \dot{B}_{\mathrm{h}}(t) \mathcal{U}_2(q_{\mathrm{e}}) \ell^2 - k(\theta_{2\mathrm{e}} - \theta_{1\mathrm{e}}), \tag{2.17b}$$

$$\mu_{\mathrm{e}} \cos\theta_{2\mathrm{e}} = -\frac{1}{2} \mathfrak{e} \dot{B}_{\mathrm{h}}(t) \mathcal{U}_3(q_{\mathrm{e}}) \ell^2 + F, \tag{2.17c}$$

where μ_{e} is the (for the moment unknown) Lagrange multiplier at equilibrium [19, p. 25].

Note that the nonholonomic constraint (1.37) is trivially satisfied when the generalized velocities are all set equal to zero. For this reason, the number of equations characterizing equilibrium reduces to the three force balances (2.17a)–(2.17c), which, however, still feature the four unknowns $\theta_{1\mathrm{e}}$, $\theta_{2\mathrm{e}}$, X_{ce}, and μ_{e}. We also notice that the torques due to the magnetic part of the Lorentz force are not present in Equations (2.17a)–(2.17c) because the velocities are set equal to zero.

Assuming $\theta_{1\mathrm{e}} = \theta_{1\mathrm{e}} = \theta_{\mathrm{e}}$, Equations (2.17a)–(2.17c) become

$$0 = -\frac{1}{2} \mathfrak{e} \dot{B}_{\mathrm{h}}(t) \mathcal{U}_1(q_{\mathrm{e}}) \ell^2 - k\theta_{\mathrm{e}}, \tag{2.18a}$$

$$0 = -\frac{1}{2} \mathfrak{e} \dot{B}_{\mathrm{h}}(t) \mathcal{U}_2(q_{\mathrm{e}}) \ell^2, \tag{2.18b}$$

$$\mu_{\mathrm{e}} \cos\theta_{\mathrm{e}} = -\frac{1}{2} \mathfrak{e} \dot{B}_{\mathrm{h}}(t) \mathcal{U}_3(q_{\mathrm{e}}) \ell^2 + F, \tag{2.18c}$$

with $\mathcal{U}_1(q_{\mathrm{e}}) = \mathcal{U}_2(q_{\mathrm{e}})$. Thus, equilibrium in the general case where $\dot{B}_{\mathrm{h}}(t)$ is different from zero requires from Equation (2.18b) that $\mathcal{U}_2(q_{\mathrm{e}}) = 0$, which may hold true only in Case I. Hence, we find

$$\mathcal{U}_2(q_{\mathrm{e}}) = 0 \qquad \Rightarrow \qquad 2 + \frac{X_{\mathrm{ce}}}{\ell} \cos\theta_{\mathrm{e}} = 0 \qquad \Rightarrow \qquad X_{\mathrm{ce}} = -\frac{2\ell}{\cos\theta_{\mathrm{e}}}. \tag{2.19}$$

Moreover, since $\mathcal{U}_1(q_{\mathrm{e}})$ vanishes too, Equation (2.18a) yields the more stringent condition

$$\theta_{\mathrm{e}} = 0. \tag{2.20}$$

This implies that $\mathcal{U}_3(q_\mathrm{e})$ also vanishes identically, thereby yielding the force balance

$$\mu_\mathrm{e} = F. \tag{2.21}$$

By gathering the results (2.19)–(2.21), we find

$$q_\mathrm{e} = (\theta_{1\mathrm{e}}, \theta_{2\mathrm{e}}, X_\mathrm{ce}) = (0, 0, -2\ell), \qquad \mu_\mathrm{e} = F. \tag{2.22}$$

The condition $\mathcal{U}_1(q_\mathrm{e}) = \mathcal{U}_2(q_\mathrm{e}) = 0$ for nonzero $\dot{B}_\mathrm{h}(t)$ amounts to placing the device in a configuration in which the electric part $\mathfrak{e}\boldsymbol{E}$ of the Lorentz force acting on the massless wheel is null (see Figure 2.2). Indeed, given the expression $\mathfrak{e}\boldsymbol{E}(\hat{x}_D(q_\mathrm{e}), t) = -\frac{1}{2}\mathfrak{e}\dot{B}_\mathrm{h}(t)(X_\mathrm{ce} + 2\ell)\boldsymbol{e}_2$, the requirement of the vanishing of this force means that the skate has to occupy the origin of the considered reference frame, where $\hat{x}_D(q_\mathrm{e}) = 0$ and, thus, $X_\mathrm{ce} = -2\ell$.

We note that no equilibrium configuration exists in Case II, since, when the device is outside the solenoid, Equation (2.18b) cannot be satisfied unless the trivial condition of time independent B_h is considered. On the other hand, if $\dot{B}_\mathrm{h}(t) = 0$ for all $t \geq t_0$, every triple $(\theta_1(t), \theta_2(t), X_\mathrm{c}(t)) = (0, 0, X_\mathrm{ce})$, with arbitrary $X_\mathrm{ce} > R_\mathrm{s}$, satisfies the equilibrium conditions.

See Fig. 2.2 for a graphical depiction of the device in the four configurations of interest inside the solenoid (Case I).

Remark 4 (One static equilibrium configuration extracted from the manifold in [5])**.** *The configuration q_e determined in Equation (2.22) is* one *particular configuration of the manifold $\{(0, 0, X_\mathrm{ce}) \colon X_\mathrm{ce} \in \mathbb{R}\}$ of equilibrium configurations obtained in [5] in the absence of magnetic interactions. This constitutes an important difference from the work by Cazzolli et al. [5]. In our setting, indeed, X_c cannot be arbitrary, since the equilibrium configuration is obtained by imposing the additional condition of null electric part of the Lorentz force acting on the skate. However, we retrieve the same equilibrium manifold as Cazzolli et al. [5] if we assume that B_h is independent of time, which implies $\dot{B}_\mathrm{h}(t) = 0$ at all times. Indeed, under the hypothesis of time-independent B_h, Equation (2.18a) returns $\theta_\mathrm{e} = 0$, Equation (2.18b) is trivially satisfied (thus, there is no counterpart of Equation (2.19) to determine X_ce, which remains unprescribed), and Equation (2.18c) reduces to $\mu_\mathrm{e} = F$.*

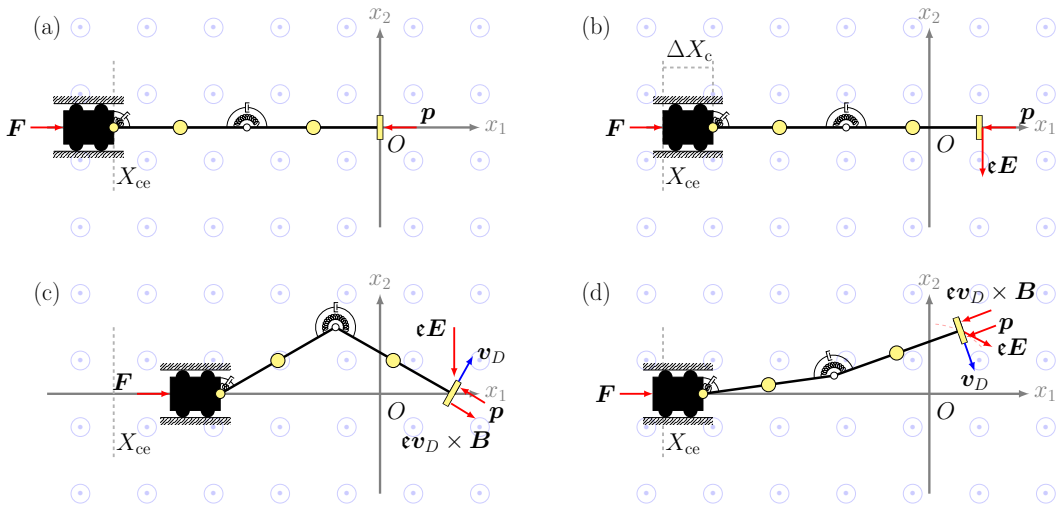

Figure 2.2: Body diagram showing the forces acting on the device in the case in which the radius $R_{\mathrm{s}} > 2\ell$ of the solenoid is sufficiently large to fully host the device and its motion (Case I). Four scenarios are depicted: (a) the device is in the static equilibrium configuration determined in Equation (2.22); (b) although the device is in a configuration with initial null velocities, such configuration is not of equilibrium because the Lorentz force, composed only by its electric contribution, produces a non-zero torque, thereby triggering the motion; (c and d) in each case the device is in a deformed configuration with nonzero velocities and, thus, the magnetic part of the Lorentz force acts on the device in addition to the electric part. In particular, we emphasize that, while $\mathfrak{e}\,\boldsymbol{v}_D \times \boldsymbol{B}$ is parallel to $\boldsymbol{n}_2$ by construction, $\mathfrak{e}\boldsymbol{E}$ has to be tangential to the circumference instantaneously centered in the origin and passing through $x_D(t)$ (indeed, $\boldsymbol{E}(x_D(t), t)$ is proportional to $\boldsymbol{e}_3 \times \boldsymbol{r}(x_D(t))$, with $\boldsymbol{r}(x_D(t)) = x_{D1}(t)\,\boldsymbol{e}_1 + x_{D2}(t)\,\boldsymbol{e}_2$).

2.3 Stability analysis: flutter instability and bifurcations in Case I

In this section, we carry out a comprehensive stability analysis of the system described by Equations (2.13a)–(2.13c) and (2.15). To this end, since we need to perturb the system from a static equilibrium configuration, we restrict our study to Case I only. For the methodologies used hereafter, we refer to [4, 5, 9, 37].

Before proceeding with the stability analysis, we notice that Equations (2.13a)–(2.13c) feature together six physical parameters to which we add the magnitude F of the dead load applied to the cart and the $\boldsymbol{e}_3$-component $B_{\mathrm{h}}(t)$ of the magnetic induction field:

$$\mathcal{P} := \{m_{\mathrm{c}};\ m, c, k, \ell;\ \mathfrak{e};\ F, B_{\mathrm{M}}\}, \tag{2.23}$$

with $B_{\mathrm{M}} := \max_t |B_{\mathrm{h}}(t)|$.

Dimensionless quantities are introduced via the mappings

$$X_{\mathrm{c}} \mapsto \frac{X_{\mathrm{c}}}{\ell}, \qquad t \mapsto \frac{t}{\sqrt{m\ell^2/k}}, \qquad \mu \mapsto \frac{\mu\ell}{k}, \qquad F \mapsto \frac{F\ell}{k}, \qquad B_{\mathrm{M}} \mapsto \frac{\mathfrak{e}B_{\mathrm{M}}\ell}{\sqrt{mk}}, \tag{2.24a}$$

$$M \mapsto \frac{M}{m}, \qquad c \mapsto \frac{c}{\ell\sqrt{mk}}. \tag{2.24b}$$

For simplicity, we do not introduce additional notation to indicate the dimensionless quantities in Equations (2.24a) and (2.24b). Rather, from here on, we simply rename them as X_{c}, t, μ, F, B_{M}, M, and c, and we differentiate with respect to the dimensionless time variable.

We emphasize that dimensionless variables are used throughout Section 2.3, and physical dimensions are restored in Section 2.4 to contextualize the numerical results.

2.3.1 Linearization of the equations governing the dynamics of the structure

To perform the stability analysis in a neighborhood of the pair $(q_\mathrm{e};\mu_\mathrm{e}) = (0,0,-2;F)$, we consider small *perturbations* around q_e and μ_e. This is achieved by introducing the homotopies $\tilde{q}$ and $\tilde{\mu}$, which define the perturbed configuration $\tilde{q}(t,\varepsilon)$ and the perturbed Lagrange multiplier $\tilde{\mu}(t,\varepsilon)$, with ε being a smallness parameter, and by requiring them to comply with the conditions $\tilde{q}(t,0) = q_\mathrm{e}$ and $\tilde{\mu}(t,0) = \mu_\mathrm{e}$. We assume $\tilde{q}$ and $\tilde{\mu}$ to be at least C^2 functions of their arguments.

The first-order expansions of $\tilde{q}$ and $\tilde{\mu}$ around $\varepsilon = 0$ and for all t can be written as:

$$\tilde{q}(t,\varepsilon) = q_\mathrm{e} + \eta(t)\varepsilon + o(\varepsilon), \quad \varepsilon \to 0, \tag{2.25a}$$

$$\tilde{\mu}(t,\varepsilon) = \mu_\mathrm{e} + \varrho(t)\varepsilon + o(\varepsilon), \quad \varepsilon \to 0, \tag{2.25b}$$

with $\eta(t) \coloneqq \partial_\varepsilon \tilde{q}(t,0)$ and $\varrho(t) \coloneqq \partial_\varepsilon \tilde{\mu}(t,0)$. In the following, we set $\eta \coloneqq (\vartheta_1, \vartheta_2, x_\mathrm{c})$.

By substituting Equations (2.25a) and (2.25b) into the dimensionless form of Equations (2.13a)–(2.13c) and (2.15), and dropping all terms of order higher than the first in ε, we obtain the dynamic equations linearized around q_e and μ_e:

$$\frac{5}{4}\ddot{\vartheta}_1 + \frac{1}{2}\ddot{\vartheta}_2 + c\,(2\dot{\vartheta}_1 - \dot{\vartheta}_2) + (2\vartheta_1 - \vartheta_2) - F(\vartheta_1 - \vartheta_2) + B_\mathrm{h}(t)\dot{x}_\mathrm{c} + \frac{1}{2}\dot{B}_\mathrm{h}(t)x_\mathrm{c} = 0, \tag{2.26a}$$

$$\frac{1}{2}\ddot{\vartheta}_1 + \frac{1}{4}\ddot{\vartheta}_2 + c\,(\dot{\vartheta}_2 - \dot{\vartheta}_1) + (\vartheta_2 - \vartheta_1) + B_\mathrm{h}(t)\dot{x}_\mathrm{c} + \frac{1}{2}\dot{B}_\mathrm{h}(t)x_\mathrm{c} = 0, \tag{2.26b}$$

$$M\ddot{x}_\mathrm{c} + \varrho - B_\mathrm{h}(t)(\dot{\vartheta}_1 + \dot{\vartheta}_2) - \frac{1}{2}\dot{B}_\mathrm{h}(t)(\vartheta_1 + \vartheta_2) = 0, \tag{2.26c}$$

$$\ddot{x}_\mathrm{c} = 0, \tag{2.26d}$$

where $B_\mathrm{h}(t)$ and $\dot{B}_\mathrm{h}(t)$ are dimensionless functions of dimensionless time. Accordingly, the dimensionless characteristic amplitude B_M of the magnetic induction field, as shown in Equation $(2.24a)_5$, is understood as $\max_t |B_\mathrm{h}(t)| = B_\mathrm{M}$.

Remark 5 (Lorentz force couples the translational and the rotational degrees of freedom)**.** *In the linearized dynamic equations (2.26a)–(2.26c), $B_\mathrm{h}(t)$ and $\dot{B}_\mathrm{h}(t)$ make it impossible to decouple x_c from ϑ_1 and ϑ_2. This holds true even in the case in which the condition $\dot{x}_\mathrm{c} = 0$ (representing the linearization of the constraint (1.37)) is substituted in (2.26a)–(2.26c), because the terms involving $\dot{B}_\mathrm{h}(t)$ do not cancel, as they represent the electric part of the Lorentz force. The linear coupling seen here, differs from the work studied by Cazzolli et al. [5] in which the absence of the Lorentz force allows for decoupling the dynamics of the cart from the dynamics of the double-pendulum.*

Following Neimark and Fufaev [9], upon introducing the 3×1 array $\mathsf{\eta} = \{\vartheta_1\ \vartheta_2\ x_\mathrm{c}\}^\mathrm{T}$ and the 1×1 array $\mathsf{\rho} = \{\varrho\}$, Equations (2.26a)–(2.26d) can be recast in matrix formalism as

$$\mathsf{M}_\mathrm{e}\ddot{\mathsf{\eta}} + [\mathsf{C}_\mathrm{e} + B_\mathrm{h}\mathsf{L}_\mathrm{e}]\,\dot{\mathsf{\eta}} + [\mathsf{K}_\mathrm{e} + F\mathsf{G}_\mathrm{e} + \frac{1}{2}\dot{B}_\mathrm{h}\mathsf{L}_\mathrm{e}]\,\mathsf{\eta} + \mathsf{A}_\mathrm{e}^\mathrm{T}\mathsf{\rho} = 0, \tag{2.27a}$$

$$\mathsf{A}_\mathrm{e}\,\ddot{\mathsf{\eta}} = 0, \tag{2.27b}$$

where M_e, K_e, and C_e represent the mass, stiffness, and damping matrices, respectively, G_e is an auxiliary (singular) matrix introduced to account for the force F, A_e is the constraint matrix, while L_e is the matrix accounting for the contributions due to the Lorentz force. These matrices read

$$\mathsf{M}_\mathrm{e} \coloneqq \begin{bmatrix} \frac{5}{4} & \frac{1}{2} & 0 \\ \frac{1}{2} & \frac{1}{4} & 0 \\ 0 & 0 & M \end{bmatrix}, \qquad \mathsf{K}_\mathrm{e} \coloneqq \begin{bmatrix} 2 & -1 & 0 \\ -1 & 1 & 0 \\ 0 & 0 & 0 \end{bmatrix}, \qquad \mathsf{C}_\mathrm{e} \coloneqq \begin{bmatrix} 2c & -c & 0 \\ -c & c & 0 \\ 0 & 0 & 0 \end{bmatrix}, \tag{2.28a}$$

$$\mathsf{G}_\mathrm{e} \coloneqq \begin{bmatrix} -1 & 1 & 0 \\ 0 & 0 & 0 \\ 0 & 0 & 0 \end{bmatrix}, \qquad \mathsf{A}_\mathrm{e} \coloneqq \begin{bmatrix} 0 & 0 & 1 \end{bmatrix}, \qquad \mathsf{L}_\mathrm{e} \coloneqq \begin{bmatrix} 0 & 0 & 1 \\ 0 & 0 & 1 \\ -1 & -1 & 0 \end{bmatrix}. \tag{2.28b}$$

Remark 6 (Faraday tensor in matrix formalism and its coupling with C_e, K_e, and $F\mathsf{G}_\mathrm{e}$)**.** *In the linearized setting, the dead load F, although being applied to the cart, influences the double pendulum through the introduction of the 'apparent' stiffness matrix $F\mathsf{G}_\mathrm{e}$, referred to as* 'geometric stiffness matrix' *in the literature [8] and adding to the elastic stiffness matrix K_e. Similarly, B_h and $\dot{B}_\mathrm{h}$ yield the 'apparent' damping matrix $B_\mathrm{h}\mathsf{L}_\mathrm{e}$ and the additional 'apparent' stiffness matrix $\frac{1}{2}\dot{B}_\mathrm{h}\mathsf{L}_\mathrm{e}$, both due to the linearization of the Lorentz force. It is worth noticing that $B_\mathrm{h}\mathsf{L}_\mathrm{e}$ is the matrix associated with the generalized Faraday tensor, evaluated at the equilibrium configuration q_e in dimensionless form and in the case in which the device is inside the solenoid (cfr. Equation (2.9a)). Analogously, $\frac{1}{2}\dot{B}_\mathrm{h}\mathsf{L}_\mathrm{e}$ is the matrix associated with the electric contribution $\frac{1}{2}\dot{B}_\mathrm{h}\mathsf{L}_\mathrm{e}\eta$ of the Lorentz force. We emphasize that the terms $B_\mathrm{h}\mathsf{L}_\mathrm{e}$ and $\frac{1}{2}\dot{B}_\mathrm{h}\mathsf{L}_\mathrm{e}$ constitute another relevant difference from the work by Cazzolli et al. [5] and add to the damping matrix C_e and to the stiffness matrix K_e, respectively.*

To solve Equation (2.27a) and (2.27b), we follow standard methods [9], and we enforce the *ansatz*

$$\eta(t) = \mathsf{H}\,\mathrm{e}^{\lambda t}, \quad \rho(t) = \mathsf{R}\,\mathrm{e}^{\lambda t}, \qquad \lambda \in \mathbb{C}, \tag{2.29}$$

where H and R are two column vectors of constant amplitudes, having sizes 3×1 and 1×1, respectively, and λ is a complex number. Substitution of Equation (2.29) into (2.27a) and (2.27b) yields

$$\left[\begin{array}{c|c} \lambda^2\mathsf{M}_\mathrm{e} + \lambda[\mathsf{C}_\mathrm{e} + B_\mathrm{h}\mathsf{L}_\mathrm{e}] + [\mathsf{K}_\mathrm{e} + F\mathsf{G}_\mathrm{e} + \frac{1}{2}\dot{B}_\mathrm{h}\mathsf{L}_\mathrm{e}] & \mathsf{A}_\mathrm{e}^\mathrm{T} \\ \hline \lambda^2\mathsf{A}_\mathrm{e} & 0 \end{array}\right] \begin{Bmatrix} \mathsf{H} \\ \mathsf{R} \end{Bmatrix} = \begin{Bmatrix} 0 \\ 0 \end{Bmatrix}, \tag{2.30}$$

where 0 denotes here the 3×1 null array.

To find nontrivial solutions to Equation (2.30), we impose that the determinant of the block-wise matrix on the left-hand side of Equation (2.30) vanish. Before proceeding, we remark that the term $\lambda^2\mathsf{A}_\mathrm{e}$ in the block-wise matrix of Equation (2.30) would lead to a sixth-grade characteristic polynomial in λ featuring a factor λ^2. This corresponds to a vanishing root of algebraic multiplicity two, which, as explained by Neimark and Fufaev [9, p. 265–267], does not affect the overall stability properties of the system. Hence, we introduce the alternative system

$$\left[\begin{array}{c|c} \lambda^2\mathsf{M}_\mathrm{e} + \lambda[\mathsf{C}_\mathrm{e} + B_\mathrm{h}\mathsf{L}_\mathrm{e}] + [\mathsf{K}_\mathrm{e} + F\mathsf{G}_\mathrm{e} + \frac{1}{2}\dot{B}_\mathrm{h}\mathsf{L}_\mathrm{e}] & \mathsf{A}_\mathrm{e}^\mathrm{T} \\ \hline \mathsf{A}_\mathrm{e} & 0 \end{array}\right] \begin{Bmatrix} \mathsf{H} \\ \mathsf{R} \end{Bmatrix} = \begin{Bmatrix} 0 \\ 0 \end{Bmatrix}. \tag{2.31}$$

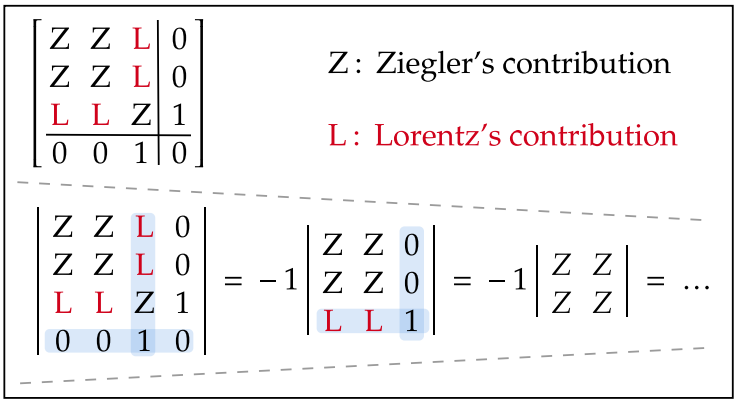

Figure 2.3: Sketch of the proof that the determinant of the block-wise matrix on the left-hand side of Equation (2.31) depends on neither $B_{\mathrm{h}}(t)$ nor $\dot{B}_{\mathrm{h}}(t)$.

Computing the determinant of the block-wise matrix on the left-hand side of Equation (2.31) yields a polynomial equation of the fourth-grade in λ, which can be written as

$$Q(\lambda) \coloneqq a_0\lambda^4 + a_1\lambda^3 + a_2\lambda^2 + a_3\lambda + a_4 = 0, \tag{2.32}$$

with the coefficients a_0, a_1, a_2, a_3, a_4 being all real and given by

$$a_0 = 1, \qquad a_1 = 44\,c, \qquad a_2 = 44 + 16\,c^2 - 12F, \qquad a_3 = 32\,c, \qquad a_4 = 16. \tag{2.33}$$

This resulting polynomial equation in fact, is identical to that which is seen in Chapter 1, Section 1.1. Thus, the linear stability analysis falls back to that of Ziegler's double pendulum,[4, 5, 8]. It should be noted that F here, is representative as the dead load which is applied to the cart of the device seen in Figure 1.4. Its magnitude is synonymous with the follower load in Section 1.1, thus the same notation can be used. The reader can be referred back to this section for a comprehensive look into the study of the roots of this polynomial, and in turn the eigenvalue analysis. To also see why this result holds true from the algebraic point of view, we report in Figure 2.3 a sketch of the structure of the block-wise matrix in Equation (2.31).

2.3.2 Investigation of Hopf bifurcation: from Schur's complement technique to dynamical systems

The Schur's complement technique [35, 36] is used in this Section to decouple the computation of the Lagrange multiplier μ from the determination of θ_1, θ_2, and X_{c}. To this end, Equations (2.13a)–(2.13c) and (2.15) are rewritten in matrix form, isolating the array $\ddot{\mathsf{q}}$ collecting the second-order derivatives $\ddot{q} \equiv (\ddot{\theta}_1, \ddot{\theta}_2, \ddot{X}_{\mathrm{c}})$ together with the Lagrange multiplier μ. We then reformulate the problem in the *state-variable formalism* and apply dynamical-systems techniques to investigate the stability of the device.

In matrix form, Equations (2.13a)–(2.13c) and (2.15) read as

$$\begin{bmatrix} \hat{\mathsf{M}}(\mathsf{q}) & -[\hat{\mathsf{A}}(\mathsf{q})]^{\mathrm{T}} \\ -\hat{\mathsf{A}}(\mathsf{q}) & \mathsf{O} \end{bmatrix} \begin{Bmatrix} \ddot{\mathsf{q}} \\ \mu \end{Bmatrix} = \begin{Bmatrix} \hat{\mathsf{b}}_{\mathsf{q}}(\mathsf{q}, \dot{\mathsf{q}}, t) \\ \hat{\mathsf{b}}_{\mathsf{c}}(\mathsf{q}, \dot{\mathsf{q}}) \end{Bmatrix}, \tag{2.34}$$

where $\hat{\mathsf{M}}(\mathsf{q})$ denotes the 3×3 mass matrix; $\hat{\mathsf{A}}(\mathsf{q})$ is the 1×3 constraint matrix; O is the 1×1 null matrix; $\hat{\mathsf{b}}_{\mathsf{q}}(\mathsf{q}, \dot{\mathsf{q}}, t)$ is a 3×1 array collecting all the terms appearing in Equations (2.13a)–(2.13c) that involve neither the generalized accelerations $\ddot{\theta}_1$, $\ddot{\theta}_2$, and $\ddot{X}_{\mathrm{c}}$, nor the Lagrange multiplier μ; $\hat{\mathsf{b}}_{\mathsf{c}}(\mathsf{q}, \dot{\mathsf{q}})$ is the 1×1 array representing the right-hand side of Equation (2.15). Note that $\hat{\mathsf{b}}_{\mathsf{q}}(q, \dot{q}, t)$ depends explicitly on time through $B_{\mathrm{h}}(t)$ and $\dot{B}_{\mathrm{h}}(t)$. The explicit expressions for $\hat{\mathsf{M}}(\mathsf{q})$, $\hat{\mathsf{A}}(\mathsf{q})$, $\hat{\mathsf{b}}_{\mathsf{q}}(\mathsf{q}, \dot{\mathsf{q}})$, and $\hat{\mathsf{b}}_{\mathsf{c}}(\mathsf{q}, \dot{\mathsf{q}})$ are

$$\mathsf{M} \equiv \hat{\mathsf{M}}(\mathsf{q}) \coloneqq \begin{bmatrix} \frac{5}{4} & \frac{1}{2}\cos(\theta_1 - \theta_2) & -\frac{3}{2}\sin\theta_1 \\ \frac{1}{2}\cos(\theta_1 - \theta_2) & \frac{1}{4} & -\frac{1}{2}\sin\theta_2 \\ -\frac{3}{2}\sin\theta_1 & -\frac{1}{2}\sin\theta_2 & M \end{bmatrix}, \tag{2.35a}$$

$$\mathsf{b}_{\mathsf{q}} \equiv \hat{\mathsf{b}}_{\mathsf{q}}(\mathsf{q}, \dot{\mathsf{q}}) \coloneqq \begin{Bmatrix} -\frac{1}{2}\sin(\theta_1 - \theta_2)\,\dot{\theta}_2^2 - c(2\dot{\theta}_1 - \dot{\theta}_2) - (2\theta_1 - \theta_2) \\ \frac{1}{2}\sin(\theta_1 - \theta_2)\dot{\theta}_1^2 - c(\dot{\theta}_2 - \dot{\theta}_1) - (\theta_2 - \theta_1) \\ \frac{3}{2}(\cos\theta_1)\dot{\theta}_1^2 + \frac{1}{2}(\cos\theta_2)\dot{\theta}_2^2 + F \end{Bmatrix} + \begin{Bmatrix} \mathfrak{F}_{\mathrm{L}1} \\ \mathfrak{F}_{\mathrm{L}2} \\ \mathfrak{F}_{\mathrm{L}3} \end{Bmatrix}, \tag{2.35b}$$

$$\mathsf{b}_{\mathsf{c}} \equiv \hat{\mathsf{b}}_{\mathsf{c}}(\mathsf{q}, \dot{\mathsf{q}}) \coloneqq \left\{(\sin\theta_2)\dot{X}_{\mathrm{c}}\dot{\theta}_2 + \cos(\theta_1 - \theta_2)(\dot{\theta}_1 - \dot{\theta}_2)\dot{\theta}_1\right\}, \tag{2.35c}$$

$$\mathsf{A} \equiv \hat{\mathsf{A}}(\mathsf{q}) \coloneqq \begin{bmatrix} \sin(\theta_1 - \theta_2) & 0 & -\cos\theta_2 \end{bmatrix}. \tag{2.35d}$$

Since $\hat{\mathsf{M}}(\mathsf{q})$ is an invertible matrix for all values of q, we can apply the Schur complement technique [35, 36, 38] to rewrite system (2.34) in normal form and, upon introducing the Schur complement $\mathsf{S} \coloneqq \mathsf{A}\mathsf{M}^{-1}\mathsf{A}^{\mathrm{T}}$ of M, we obtain

$$\ddot{\mathsf{q}} = [\mathsf{M}^{-1} - (\mathsf{M}^{-1}\mathsf{A}^{\mathrm{T}})\mathsf{S}^{-1}(\mathsf{A}\mathsf{M}^{-1})]\mathsf{b}_{\mathsf{q}} - (\mathsf{M}^{-1}\mathsf{A}^{\mathrm{T}})\mathsf{S}^{-1}\mathsf{b}_{\mathsf{c}}, \tag{2.36a}$$

$$\mu = -\mathsf{S}^{-1}[(\mathsf{A}\mathsf{M}^{-1})\mathsf{b}_{\mathsf{q}} + \mathsf{b}_{\mathsf{c}}]. \tag{2.36b}$$

Equation (2.36a) unfolds three scalar equations for the three unknowns collected in q, and, once these are computed, Equation (2.36b) determines the Lagrange multiplier μ.

A further step beyond Equation (2.36a) consists in introducing the *state-variable formalism*, which allows us to recast (2.36a) as a system of six first-order scalar ordinary differential equations. In fact, by setting $Y_1 \coloneqq \theta_1$, $Y_2 \coloneqq \theta_2$, $Y_3 \coloneqq X_{\mathrm{c}}$, $Y_4 \coloneqq \dot{\theta}_1$, $Y_5 \coloneqq \dot{\theta}_2$, $Y_6 \coloneqq \dot{X}_{\mathrm{c}}$, and introducing the 6×1 arrays $\mathsf{Y} = \{Y_1 \cdots Y_6\}^{\mathrm{T}}$ and $\dot{\mathsf{Y}} = \{\dot{Y}_1 \cdots \dot{Y}_6\}^{\mathrm{T}}$, Equation (2.36a) is equivalent to

$$\dot{\mathsf{Y}} = \mathsf{f}(\mathsf{Y}, t; F), \tag{2.37}$$

where, for $k = 1, 2, 3$, $f_k(\mathsf{Y}, t; F) = Y_{k+3}$, while $f_4(\mathsf{Y}, t; F)$, $f_5(\mathsf{Y}, t; F)$, and $f_6(\mathsf{Y}, t; F)$ are the three components of the right-hand side of Equation (2.36a), written in the state variable formalism.

In Equation (2.37), the vector field $\mathsf{f}(\mathsf{Y}, t; F)$ inherits its explicit time dependence from $\hat{\mathsf{b}}_{\mathsf{q}}(\mathsf{q}, \dot{\mathsf{q}}, t)$. However, this dependence appears only in the components $f_4(\mathsf{Y}, t; F)$, $f_5(\mathsf{Y}, t; F)$, and $f_6(\mathsf{Y}, t; F)$. We also emphasize that we have expressed the functions as parametrically dependent on the dead load F, which plays the role of the bifurcation parameter. Although the characteristic magnetic induction B_{M} may, in principle, influence the stability of the device [27], it is treated here as a fixed parameter for simplicity, and F is taken as the sole bifurcation parameter of the study.

We now investigate the stability of the equilibrium configuration q_{e}, given in Equation (2.22), following standard dynamical-systems procedures. In particular, we refer to the

dynamical system described by Equation (2.37). Our aim is to assess whether or not the system undergoes a Hopf bifurcation at $F = F_{\text{flu}}(c)$. To this end, we analyze the eigenvalues of the Jacobian matrix of the map f in Equation (2.37), evaluated at the equilibrium point $\mathsf{Y} = \mathsf{Ye} = \{0; 0; -2; 0; 0; 0\}^{\mathrm{T}}$. This corresponds to expressing qe in the state-variable formalism of Section 2.3.2, with $X_{\text{ce}} = -2$.

We start considering the first-order Taylor expansion of f at Y_{e} and for a generic value of F. Hence, for $j = 1, \dots, 6$, and in the limit $\|\mathsf{Y} - \mathsf{Y}_{\text{e}}\|_2 \to 0$, we write

$$[\mathsf{f}(\mathsf{Y}; F)]_j = \underbrace{[\mathsf{f}(\mathsf{Y}_{\text{e}}; F)]_j}_{=0} + \sum_{k=1}^{6} \underbrace{\left[\frac{\partial f_j}{\partial Y_k}(\mathsf{Y}_{\text{e}}; F)\right]}_{=: [\mathsf{J}_{\text{e}}]_{jk}} [Y_k - (Y_{\text{e}})_k] + o(\|\mathsf{Y} - \mathsf{Y}_{\text{e}}\|_2), \tag{2.38}$$

where $\|\mathsf{p}\|_2 := \sqrt{\mathsf{p}^{\mathrm{T}}\mathsf{p}}$ denotes the 2-norm of a generic (column) array p. The 6×6 Jacobian matrix $\mathsf{J}_{\text{e}} \equiv \hat{\mathsf{J}}\,(\mathsf{Y}_{\text{e}}; F)$ features six eigenvalues given by the roots of the characteristic equation

$$P(\omega; F) = \det(\mathsf{J}_{\text{e}} - \omega \mathsf{I}_6) = \frac{1}{M} Q(\omega; F)\, \omega^2 = 0, \tag{2.39}$$

where $Q(\omega; F)$ is a rewriting of the fourth-grade characteristic polynomial in Equation (1.6), associated to the double pendulum, with ω replacing λ and the dependence on F made explicit. The roots of $P(\omega; F)$ define the eigenvalues $\omega_1, \dots, \omega_6$ as functions of F, so that we may write $\omega_j = \hat{\omega}_j(F)$, for $j = 1, \dots, 6$.

As noticed in Section 2.3.1 and sketched in Figure 2.3, the characteristic polynomial $Q(\omega; F)$ remains unchanged regardless of whether or not the Lorentz force is considered, and the same applies to $P(\omega; F)$. Hence, $P(\omega; F)$ and its roots can be used to analyze the occurrence of a Hopf bifurcation as if the Lorentz force were absent, in which case the dynamical system would behave as autonomous.

Although the characteristic equation (2.39) describes the device as a whole—including the skate, which contributes the factor ω^2 arising from the constraint—the decoupling, in terms of the eigenvalues, between the double pendulum and the cart in the linearized analysis of Section 2.3 is manifested in the factorization shown in Equation (2.39). Indeed, the characteristic polynomial features two distinct factors: one of grade four for the double pendulum, $Q(\omega; F)$; another of grade two, ω^2, related to the nonholonomic constraint. The presence of the latter can be related to the linearized constraint, and thus to the acceleration of the cart $\ddot{x}_{\text{c}}$ in Equation (2.26d).

When Equation (2.39) is evaluated at $F = F_{\text{flu}}(c)$, the polynomial $Q(\omega; F)$ becomes

$$Q(\omega; F_{\text{flu}}(c)) = (22 + 44\, c\, \omega + \omega^2)(8/11 + \omega^2) = 0, \tag{2.40}$$

and the eigenvalues of $\mathsf{J}_{\text{e}} \equiv \hat{\mathsf{J}}\,(\mathsf{Y}_{\text{e}}; F_{\text{flu}}(c))$ are the roots of the characteristic equation

$$P(\omega; F_{\text{flu}}(c)) = \frac{1}{M}(22 + 44\, c\, \omega + \omega^2)(8/11 + \omega^2)\omega^2 = 0, \tag{2.41}$$

which read

$$\underbrace{\omega_{1,4} = -22c \pm \sqrt{-22 + (22c)^2}, \quad \omega_{2,3} = \pm i\sqrt{8/11}}_{\text{double pendulum}}, \qquad \underbrace{\omega_{5,6} = 0.}_{\text{constraint}} \tag{2.42}$$

Moreover, the eigenvalues $\omega_{1,4} \equiv \hat{\omega}_{1,4}(F_{\text{flu}}(c))$ depend parametrically on c both through $F_{\text{flu}}(c)$ and through the coefficients of $Q(\omega; F)$, as shown in Equation (2.40).

The first four roots obtained from Equation (2.41), ω_1, ω_2, ω_3 and ω_4, are also roots of Equation (2.40), and refer to the double pendulum, which experiences flutter instability. In particular, the eigenvalues ω_1 and ω_4 are complex conjugate for $c \in]0, 1/\sqrt{22}[$, while they are purely real for $c > 1/\sqrt{22}$, and are coincident for $c = 1/\sqrt{22}$. In all these cases, $\mathrm{Re}[\omega_1]$ and $\mathrm{Re}[\omega_4]$ are negative for all $c > 0$. Hence, ω_1, ω_2, ω_3, and ω_4 characterize the onset of flutter through a Hopf bifurcation [5]. In particular, a Hopf bifurcation at the equilibrium Y_e, occurring at $F \equiv F_\mathrm{flu}(c)$, arises if the following three conditions are satisfied [39]:

1. At the onset of flutter, Y_e is an equilibrium state, $\mathsf{f}(\mathsf{Y}_\mathrm{e}; F_\mathrm{flu}(c)) = \mathsf{0}$;
2. At $F = F_\mathrm{flu}(c)$, exactly one pair of purely imaginary complex-conjugate eigenvalues exists, each of algebraic multiplicity one, while all remaining eigenvalues have nonzero real part (in our case, negative real part).
3. The eigenvalues $\omega_2(F)$ and $\omega_3(F) \equiv \bar{\omega}_2(F)$ that, at $F = F_\mathrm{flu}(c)$, form to the aforementioned pair of conjugate imaginary eigenvalues must depend on F in such a way that their real part be differentiable at $F_\mathrm{flu}(c)$ and compliant with the condition

$$\frac{\mathrm{d}\,\mathrm{Re}[\omega_{2,3}]}{\mathrm{d}F}(F_\mathrm{flu}(c)) \neq 0. \tag{2.43}$$

The fulfillment of these conditions is highlighted in Figure 1.2b within the previous Chapter.

Remark 7 (Lorentz force does not affect the onset of the Hopf bifurcation for $F = F_\mathrm{flu}(c)$)**.** *It has been shown that, despite the inclusion of the Lorentz force in the model studied by Cazzolli et al. [5], the system still undergoes a Hopf bifurcation under the same conditions, namely when the dead load F reaches the critical flutter load $F_\mathrm{flu}(c)$.*

We conclude by noting that a Hopf bifurcation occurs even though the eigenvalues ω_5 and ω_6 vanish and, strictly speaking, do not satisfy the second Hopf condition. Moreover, they make the Jacobian matrix J_e singular and preclude the possibility of computing the first Lyapunov coefficient for the problem as is currently formulated. However, as recalled in Section 2.3, ω_5 and ω_6 can be disregarded from the study of stability and, thus, of the bifurcations [9]. This argument is grounded in the same reasoning used to derive Equation (2.31) from Equation (2.30) in the stability analysis.

2.4 Post-critical behavior: the Lorentz force can influence the flutter instability

In this section, the aim is to assess how the Lorentz force can influence the post-critical behavior of the device both in Case I and in Case II. As anticipated in the preamble of Section 2.3, the physical dimensions of the problem are now restored to give context to the following benchmark tests.

2.4.1 The scenario of a soft bodied micro-robot for biological applications

Among the various designs that are often employed in micro-robotics [40], we model our micro-robot as a continuous rod (discretized by the double-pendulum), attached to a small mass (the cart), having both viscous and elastic material properties (the viscoelastic hinges),

and a concentrated electric charge at one end (the point charge $\mathfrak{e}$ in D). Specifically, we assume the rod to be made of an idealized rubber-like material with density $\rho = 10^3\,\mathrm{kg/m^3}$ and Young modulus $E_\mathrm{Y} = 10^6\,\mathrm{Pa}$, [29].

The device's geometry is characterized by slender bars, with length $\ell = 10\,\mu\mathrm{m}$, width $w = 1\,\mu\mathrm{m}$, and thickness $\tau = 0.1\,\mu\mathrm{m}$, so that their volumes and moments of inertia read $V = \ell w \tau$ and $J = (1/12)\tau^3 w$, respectively (the aspect ratio of the bars and the notation are taken from [27]). Consequently, the mass of one bar reads $m = \rho V$, while the stiffness coefficient k is computed as $k = E_\mathrm{Y} J/\ell$ [27]. Once k is obtained, the damping coefficient c (modeling the overall viscous behavior of the robot) is selected coherently with the work by Cazzolli et al. [5]. Hence, c is chosen in such a way that the dimensionless damping coefficient of Equation (2.24b)$_2$ is $c/(\ell\sqrt{mk}) = 0.1$ (cfr. Section 2.3).

The value of the dead load F is in line with the typical thrust and propulsion forces reported for microrobots in biological applications [31]. Specifically, we choose the value $F = 1.6\,\mathrm{pN}$, for which flutter can occur, since $F \simeq 1.1, F_\mathrm{flu}(c)$.

The solenoid is assumed to be sufficiently long, with height at least four times its diameter [6], and radius $R_\mathrm{s} = 5\,\mathrm{cm}$, and capable of generating a magnetic induction field of maximum amplitude $B_\mathrm{M} = 1\,\mathrm{T}$. We emphasize that this value of B_M is higher than those typically used to study, for instance, the motility of micro- or nano-robots in biological environments (usually around the order of magnitude of $10^{-3}\,\mathrm{T}$, [31]). Although the value $B_\mathrm{M} = 1\,\mathrm{T}$ may be considered extreme, we adopt it to make the Lorentz force comparable to the propulsion forces (dead load) considered in [31] and to the follower force. Solenoids with relatively small diameters can nevertheless reach MRI-level magnetic induction fields [41, 42] and can be used for micro-motility applications [43]. However, we remark that if lower values of the dead load (corresponding to a weaker propulsion) and lower values of B_M are considered, the springs have to be less stiff than those used here.

The magnetic induction field is assumed to be sinusoidal in time by setting

$$B_\mathrm{h}(t) = B_\mathrm{M}\sin(\Omega\, t), \qquad \text{so that} \qquad \dot{B}_\mathrm{h}(t) = B_\mathrm{M}\Omega\cos(\Omega\, t), \tag{2.44}$$

with Ω being the its frequency of oscillation. In the following sections, we examine the cases $\Omega = 5, \mathrm{kHz}$ and $\Omega = 10, \mathrm{kHz}$, consistent with the frequency range adopted by Rousseaux et al. [6] to justify the low-frequency approximation for the vector potential $\boldsymbol{A}$. We restrict the analysis to a parametric study of ω, while all the other parameters are kept fixed.

The point charge concentrated at the skate is in agreement with the effective net charge of micro-metric entities in aqueous media, as documented in electrokinetic studies, [28]. We select $\mathfrak{e} = 0.03\,\mathrm{pC}$ rather than the more natural value $\mathfrak{e} = 0.01\,\mathrm{pC}$ to amplify the influence of the Lorentz force, without allowing the magnetic field amplitude to exceed 1 T.

Remark 8 (Implementation details)**.**
The simulations are obtained by numerically solving the Cauchy problem defined by Equation (2.37), together with the the array of initial conditions $\mathsf{Y}_0 = \{0\ 0\ X_{\mathrm{c}0}\ 0\ 0\ 0\}^\mathrm{T}$. *In Case I,* $X_{\mathrm{c}0}$ *is chosen as a small deviation from* X_ce *in Equation (2.22), while in Case II it is* $X_{\mathrm{c}0} > R_\mathrm{s}$. *Null initial velocities are assumed. Numerical simulations are performed in MATLAB [44] using the adaptive Runge–Kutta (4,5) scheme implemented in the* `ode45` *function for time integration [45].*

2.4.2 Case I: the Lorentz force triggers the fluttering motion and can 'stop' the device

We consider the case in which the device is fully contained within the solenoid and the cart is initially positioned at $X_{\mathrm{c}0} = -1.5\ell$. For this configuration, corresponding to Figure 2.2b,

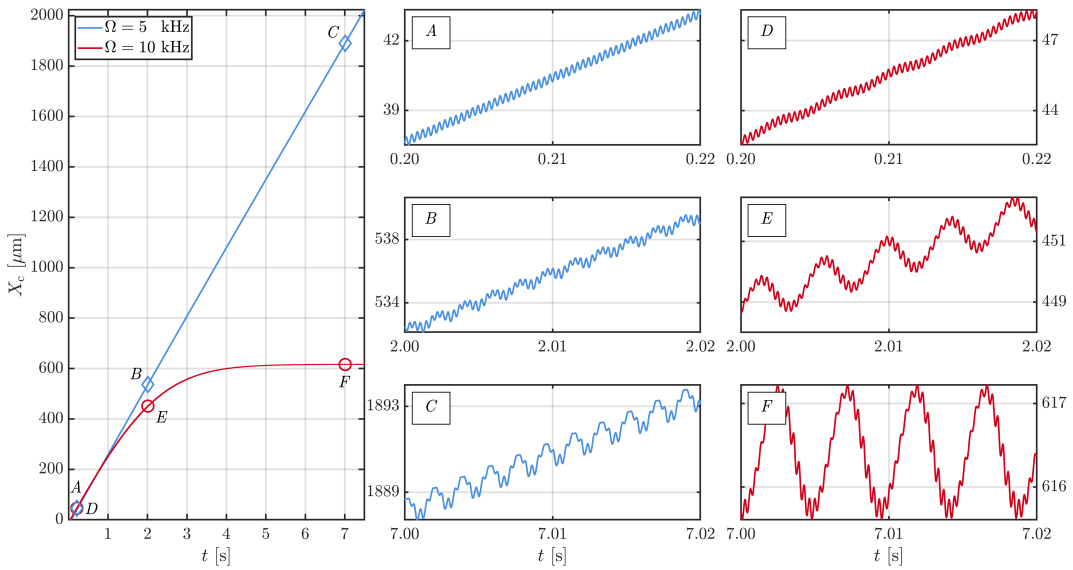

(a) Time trend of X_c for $\Omega = 5\,\text{kHz}$ (blue line with diamonds) and for $\Omega = 10\,\text{kHz}$ (red line with circles).

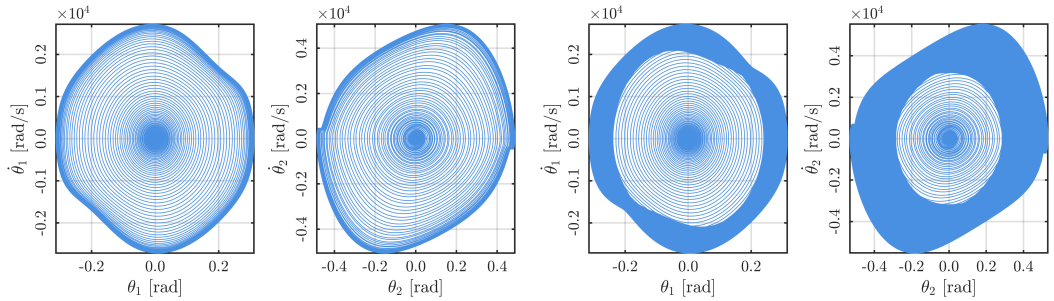

(b) Phase portraits of θ_1 and θ_2, for $\Omega = 5\text{kHz}$, over the interval $[0\,\text{s}, 0.1\,\text{s}]$, terminating at A.

(c) Phase portraits of θ_1 and θ_2, for $\Omega = 5\,\text{kHz}$, over the interval $[0\,\text{s}, 7\,\text{s}]$, terminating at C.

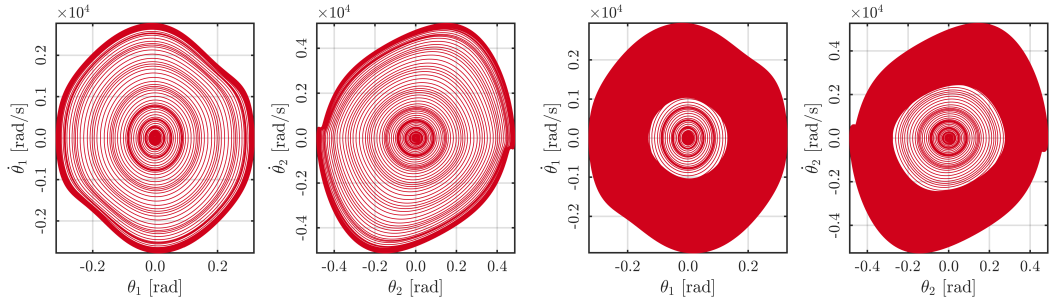

(d) Phase portraits of θ_1 and θ_2, for $\Omega = 10\,\text{kHz}$, over the interval $[0\,\text{s}, 0.1\,\text{s}]$, terminating at D.

(e) Phase portraits of θ_1 and θ_2 for $\Omega = 10\text{kHz}$ over the interval $[0\,\text{s}, 7\,\text{s}]$, terminating at F.

Figure 2.4: Time trend of X_c and phase portraits of θ_1 and θ_2 concerning the parametric study conducted for Case I and representing the dynamic motion induced by flutter instability on a movable double pendulum with nonholonomic constraint and embedded in a magnetic field.

Parameter	Symbol	Value	Unit	Ref.
Length of each bar	ℓ	10	μm	[30, 31]
Mass of each bar	m	0.001	ng	[29]
Mass of the cart	m_{c}	0.01	ng	–
Spring stiffness	k	10	pN μm	[27]
Damping coefficient	c	0.0001	pN μm s^{-1}	[5]
Dead load	F	1.6	pN	[31]
Electric charge	$\mathfrak{e}$	0.03	pC	[28]
Solenoid radius	R_{s}	5	cm	[41, 42]
Magnetic amplitude	B_{M}	1	T	[43, 42]
Magnetic frequency	Ω	$\{5, 10\}$	kHz	[6]

Table 2.1: Numerical values used for the simulations.

with $|X_{\mathrm{c0}} - X_{\mathrm{ce}}| = 0.5\ell$, flutter occurs as induced by the nonzero torque exerted by the electric part of the Lorentz force. This phenomenon does not arise in the problem studied by Cazzolli et al. [5], where flutter is triggered only by perturbations of the angles θ_1 or θ_2, or of their associated angular velocities.

We begin with the case $\Omega = 5\,\mathrm{kHz}$, represented in Figure 2.4 by the solid blue line marked with diamonds. Figure 2.4a shows that for $\Omega = 5\,\mathrm{kHz}$ the motion of the cart, described by X_{c}, exhibits oscillations around a *main, roughly linear, trend*. In spite of the different setting considered in our work, this result is similar to what was found in the paper by Cazzolli et al. [5], in which the cart advances on a large scale with a mean velocity, but it experiences oscillations around such mean velocity on a smaller scale (see the top left panel of Figure 12 of [5]). Regarding the large scale motion, the Lorentz force seems not to affect significantly the dynamics of the cart: the cart moves away from the solenoid center with a comparatively large and approximately constant mean velocity of about $260\,\mu\mathrm{m\,s}^{-1}$, thereby covering about 13 body lengths (2ℓ) per second. However, while the cart's small scale oscillations in our work and in [5] are comparable to each other in the first instants of our simulation (see the zoomed-in region labeled with 'A' in Figure 2.4a), they are modified by the Lorentz force over time, as the device advances into regions in which the Lorentz force is stronger (see the zoomed-in regions A, B, and C of Figure 2.4a).

Figures 2.4b and 2.4c show the phase portraits of θ_1 and θ_2 for the case $\Omega = 5\,\mathrm{kHz}$ and over the time windows $[0\,\mathrm{s}, 0.1\,\mathrm{s}]$ and $[0\,\mathrm{s}, 7\,\mathrm{s}]$, respectively. For brevity, the phase portraits corresponding to the intermediate time interval $[0\,\mathrm{s}, 2\,\mathrm{s}]$ are not shown.

The increasing amplitude of the oscillations of X_{c} should be compared with the phase plots of θ_1 and θ_2 in Figures 2.4b and 2.4c, and, in particular, with the progressive clustering of the orbits, as time goes by, from Figure 2.4b (corresponding to the region A) to Figure 2.4c (corresponding to the region C). Our conclusion is that the Hopf bifurcation, rather than resulting into a stable limit cycle, is characterized by an almost chaotic behavior.

A different situation occurs for $\Omega = 10\,\mathrm{kHz}$. At this frequency, and with reference to the solid red line marked with circles in Figure 2.4a, the device no longer experiences a motion similar to that reported by Cazzolli et al. [5]. Indeed, although the cart initially advances as in the case $\Omega = 5\,\mathrm{kHz}$ (and thus as predicted in [5]), exhibiting micro-oscillations in the evolution of X_{c} (see the zoomed-in regions D, E, and F of Figure 2.4a), the increasing Lorentz force eventually causes a qualitative change in the motion. The zoomed-in regions D, E, and F in Figure 2.4a show that X_{c} oscillates around a *non-linear trend* and that, in this case, the oscillations gain a much more marked two-scale character with increasing time

(from D to F). For $t \geq 7\,\mathrm{s}$, the cart swings in a bounded region of space, without appreciable further advancement, thereby suggesting an average-in-time balance among the dead load, the follower force and the Lorentz force. Also in this case, the oscillations of the cart are to be compared with the progressive thickening of the clusters of orbits reported in Figures 2.4d and 2.4e, which show the phase portraits of θ_1 and θ_2 for the case $\Omega = 10\,\mathrm{kHz}$ and over the time windows $[0\,\mathrm{s}, 0.1\,\mathrm{s}]$ and $[0\,\mathrm{s}, 7\,\mathrm{s}]$, respectively. Again, the agglomeration of orbits seems to indicate the tendency of the system towards chaos rather than towards stable limit cycles, with a quasi-periodic behavior.

The increasing impact of the Lorentz force on the flutter instability is also reflected in the phase diagrams of θ_1 and θ_2. Figures 2.4c and 2.4e show that the phase portraits of θ_1 and θ_2 do not converge to single closed orbits corresponding to stable limit cycles, in contrast to the behavior reported by Cazzolli et al. [5]. As time progresses, the simulations predict the formation of progressively larger regions, or 'bands', of trajectories in the corresponding phase spaces. This behavior is likely due to the modulations induced by the Lorentz force (see Figures 2.4c and 2.4e),and is more pronounced in the case with 10 kHz, since the oscillations of the cart around the main trend are stronger than for $\Omega = 5\,\mathrm{kHz}$.

Lastly, we find it worth mentioning that, both for $\Omega = 5\,\mathrm{kHz}$ (region C, corresponding to $t = 7\,\mathrm{s}$) and for $\Omega = 10\,\mathrm{kHz}$ (regions D, E, and F) the Lorentz force seems to induce three-scale dynamics: a main trend, which is linear for $\Omega = 5\,\mathrm{kHz}$ and nonlinear for $\Omega = 10\,\mathrm{kHz}$, 'slow' oscillations, and 'fast' oscillations. The regions C and E of Figure 2.4a are those in which this phenomenon is best displayed.

2.4.3 Case II: the Maxwell–Lodge effect in the dynamics of the micro-robot

We now consider Case II, in which the device is located outside the solenoid. To characterize its overall motion, we examine the time evolution of the cart position. Owing to the geometric symmetry of the configuration, we analyze two initial placements: one to the left of the solenoid and one to the right, both equidistant from the origin.

Figure 2.5a illustrates the case in which the cart is positioned to the left of the solenoid. Each of the branches in Figure 2.5a represents the motion of the cart for different initial conditions X_{c0}, with the upper branch (marked with circles) associated with $X_{c0} = -13.20\,\mathrm{cm}$ and the lower branch (marked with squares) corresponding to $X_{c0} = -13.60\,\mathrm{cm}$. We recall that outside the solenoid any initial position X_{c0} of the cart is of non-equilibrium and therefore Figure 2.5a shows how the cart evolves, either moving away from the solenoid's boundary (curve marked with circles) or moving towards it (curve marked with squares). Moreover, even if the device is initially in a straight configuration, with $\theta_1(0) = \theta_2(0) = 0$ and $\dot{\theta}_1(0) = \dot{\theta}_2(0) = 0$, the Lorentz force acting on the skate generates an unbalanced torque that induces angular motion of the bars, ultimately leading to flutter, as discussed in Section 2.3.1. The observed dynamic behavior is argued to be a consequence of the Maxwell–Lodge effect, according to which, even in the absence of the magnetic induction field (see Remark 3 and Equations (1.49b) and (1.52b)), the Lorentz force acting on the skate remains nonzero. In the configuration considered here, this force is parallel to the x_2-axis and therefore orthogonal to the device (see the zoomed-in region for Case II in Figure 2.1).

In addition, both mean positions of the cart—one with initial position at $-13.20\,\mathrm{cm}$ (circles) and the other at $-13.60\,\mathrm{cm}$ (squares)—tend asymptotically toward a position at approximately $-13.38\,\mathrm{cm}$, about which they oscillate. In view of this behavior, and with a slight abuse of terminology, we refer to the point $(-13.38\,\mathrm{cm}, 0)$ as an 'attractor'. Complementary to the trajectories of the cart X_c converging to the attractor, Figures 2.5d and 2.5e

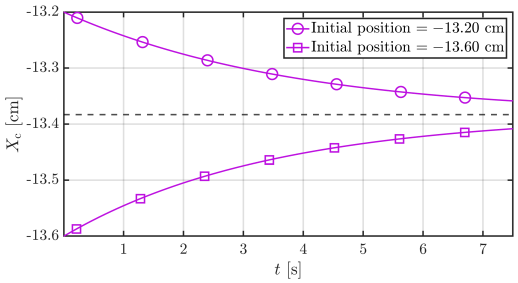

(a) Time trend of X_c for $\Omega = 10$ kHz, when the cart is placed outside of the solenoid on its left, at a position of -13.2 cm (circles) and -13.6 cm (squares).

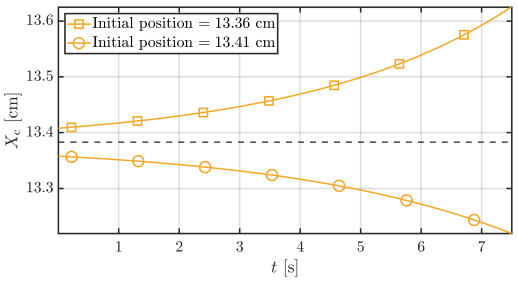

(b) Time trend of X_c for $\Omega = 10$ kHz, when the cart is placed outside of the solenoid on its right, at a position of 13.36 cm (circles) and 13.41 cm (squares).

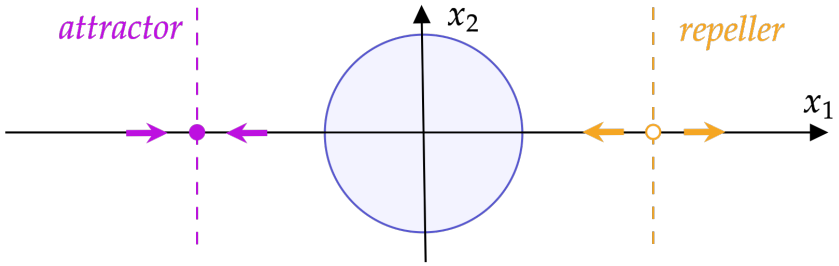

(c) Graphical depiction of the 'attractor' point and 'repeller' point. The picture is not in scale.

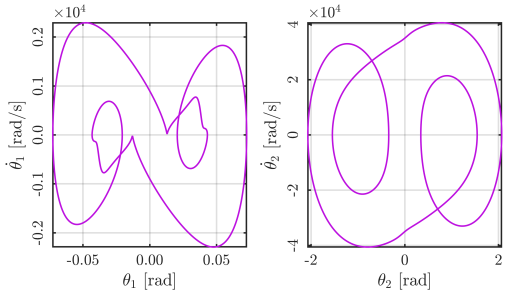

(d) Phase plots of θ_1 and θ_2, at when the device is placed at the point attractor $(-13.38\,\text{cm}, 0)$.

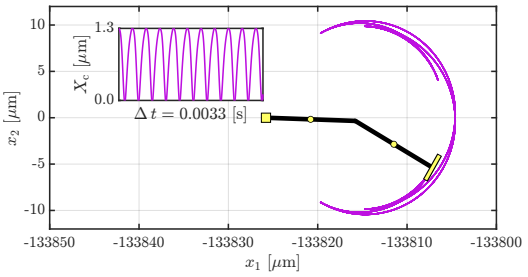

(e) Trace of the position of D alongside the cart oscillations (zoomed in section) at the point attractor $(-13.38\,\text{cm}, 0)$.

Figure 2.5: Time trend of X_c (a) and (b), picture of the 'attractor' and 'repeller' points (c), phase portraits of θ_1 and θ_2 (d), and trajectory of the point D (e) for the parametric study of Case II and representing the dynamic motion induced by flutter instability on a movable double pendulum with an electrically charged nonholonomic constraint, embedded in a magnetic field.

also present the phase portraits of the angles θ_1 and θ_2 when the cart is at the attractor, together with a zoomed-in view of the cart displacement and the trajectory of point D. The dynamical regime in which the device now operates, as observed from the phase portraits, appears to lead to stable limit cycles. This is further illustrated in the zoomed-in view of X_c, where no micro-oscillations are observed to disturb the motion. We believe that, in this case, the Lorentz force acting at the tip of the pendulum is the dominant contribution.

Analogous considerations apply to Figure 2.5b, although the opposite behavior is observed. For symmetry, we place the cart at two initial positions near the point $(13.38\,\text{cm}, 0)$, on the right-hand side of the solenoid: $X_{c0} = 13.36\,\text{cm}$ (corresponding to the curve marked with squares) and $X_{c0} = 13.41\,\text{cm}$ (corresponding to the curve marked with circles). The mean trajectories of the cart are now repelled from this point: the one with initial position $X_{c0} = 13.36\,\text{cm}$ moves back toward the solenoid, whereas the one with initial position $X_{c0} = 13.41\,\text{cm}$ moves away from it. Accordingly, we refer to the point $(+13.38\,\text{cm}, 0)$ as a 'repeller'.

Consistent with the discussion above, we emphasize that the device may also undergo backward motion in order to approach the 'attractor' or move away from the 'repeller', as shown in Figure 2.5. Such behavior is not achievable in the context of the problem studied by Cazzolli et al. [5].

2.5 Discussion and conclusions

A mechanical structural system has been proposed and analyzed that is capable of generating propulsion from an applied conservative force and a magnetic field by exploiting flutter instability and Hopf bifurcation. The system provides a simple model of a microrobot suitable for operating in magnetically controlled environments, without relying on conventional propulsion mechanisms. Note that, when viscosity is absent, the sole responsible for the variation of energy is the electric part of the Lorentz force. If the latter is switched off, the system becomes indeed conservative.

Our design has coupled a Ziegler double pendulum with a movable cart subject to a dead load and an electrically charged non holonomic constraint. Electromagnetic interactions provide a Lorentz force applied on the constraint, when placed inside or outside an ideal solenoid. Our setup differs from previously analyzed devices based on electric dipoles or magnetic torques [27].

A primary consequence of the theoretical framework underlying our work is the recognition that the Maxwell–Lodge effect [6, 23] may also be observed in systems such as the microrobot considered here. Owing to the significance of this effect in physics, from both theoretical and experimental perspectives—Rousseaux et al. [6] describe it as the *'classical equivalent'* of the *'Aharonov–Bohm effect [...] within quantum physics'*—we found it appropriate to revisit it within our framework (see Remark 3) and to assess its role in the dynamics of the device.

We have proposed two 'virtual' experimental configurations (Case I and Case II), formulated as dedicated Cauchy problems, which may serve as benchmarks for future investigations of the post-critical dynamics of systems similar to ours.

Although the device exhibits behaviors not reported in previous studies, and although the parameters adopted in our simulations are drawn from the literature (see Table 2.1), the intensity B_M of the magnetic induction field may be relatively high. In particular, we selected $B_M = 1,\text{T}$—a value achievable in MRI-based and electron-beam experiments [42]—in order to ensure that the Lorentz force is comparable in magnitude to the dead load

F typically considered in Ziegler's double pendulum models in microrobotics, as well as to the follower force.

A systematic analysis for smaller values of B_{M} would be desirable to further delineate the range of validity of the present results. Notwithstanding this limitation, the findings summarized in Figures 2.4a–2.4e and 2.5a–2.5b provide a basis for further discussion on the interplay between flutter instability and Hopf bifurcation in devices controlled through additional forces such as the Lorentz force (see Remark 7).

As shown in Figures 2.5a and 2.5b, the Lorentz force outside the solenoid—arising solely from the induced electric field—can either attract or repel the microrobot (through its action on the cart), depending on whether the cart is initially positioned below or above a critical distance from the left or right boundary of the solenoid.

The present study contributes to the analysis of the stability of microrobots and related structures inspired by Ziegler's double pendulum, particularly when interactions beyond purely mechanical effects are taken into account. The results may provide a reference framework for future investigations based on alternative experimental configurations and may stimulate the design of new experimental studies in this area.

Chapter 3

Double pendulum interacting with a moving plate

In this chapter, the constrained Zeigler's double pendulum is considered to be interacting with a plate that is restricted to axial motion and possesses a concentrated mass. The equations of motion are derived using a constrained form of D'Alembert's principle. A stability analysis around a chosen equilibrium is performed, followed by an investigation of changes in the Hopf bifurcation and the resulting post-critical dynamics, which reveal a self-induced resonant interaction between the pendulum and the plate. The text and equations consolidating this chapter are taken from [2]

3.1 Introduction

First observed in aeroelastic and rotor-dynamic systems about a century ago, flutter instability –an oscillatory motion of blowing-up amplitude– has been the focus of a thorough research effort in structural mechanics [15, 24, 46]. Recently it has regained prominence due to expanding applications of non-conservative elasticity across scales [47], from nanomechanics [48, 49] to space structures [50, 51, 52] and biomechanical systems [53]. In structural mechanics, the prototype model was introduced by Ziegler [4], who demonstrated that a double pendulum with viscoelastic joints may become dynamically unstable under the action of a follower (nonconservative) force. This instability exhibits several counterintuitive features—emphasized by prominent researchers such as Vladimir Bolotin and Warner Koiter—and was long regarded as mechanically unrealistic, being attributed solely to the nonconservative nature of the loading. A turning point in this line of research was the experimental demonstration that follower forces can be generated by friction [8], which opened new experimental avenues, together with the theoretical prediction of flutter in structures subject to nonholonomic constraints and conservative forces [5, 54]. The latter framework is adopted in the present article to design a structure in which self-induced oscillations arising from flutter and Hopf bifurcation interact with a resonant elastic system. This interaction creates a dynamical framework in which linear modal amplification and nonlinear self-excitation coexist, leading to novel instability mechanisms and altered stability thresholds. In fact, when the Hopf frequency approaches a plate resonance, the limit-cycle amplitude and the mean structural velocity diverge. In addition, subcriticality sets in, creating instability regions characterized by multistability or chaotic motion.

Our results highlight two major consequences. When the nonlinear dynamics triggered by instability is regarded as detrimental, the interaction between flutter and resonance markedly reduces stability margins and accelerates fatigue, thereby increasing structural vulnerability. Conversely, when nonlinear dynamics is treated as a resource rather than a liability, the same interaction can be deliberately harnessed for controlled amplification and advanced nonlinear sensing applications.

3.2 Double pendulum interacting with a moving plate

The dynamics of a structure involving a nonholonomic constraint is analyzed. This mechanical device is composed of a cart, a double pendulum, and a movable plate, connected through springs and dampers as described below and illustrated in Figure 3.1. An external force is applied to the cart, and a nonholonomic constraint restricts the end-point velocities of one bar in the double pendulum, joining this point with the plate, as explained in the following. The device is an extension of the system analyzed by Cazzolli et al. [5].

A set of Cartesian coordinates (X_1, X_2) is introduced, Figure 3.1, associated with the horizontal and the vertical axes of a global reference frame with origin in the point $O \equiv (0, 0)$, and unit vectors $\boldsymbol{e}_1$ and $\boldsymbol{e}_2$. A double pendulum is linked on its left end to a cart of mass $m_\mathrm{c} > 0$, capable of frictionless horizontal motion, and subject to a dead load $\boldsymbol{F} \equiv F\boldsymbol{e}_1$ ($F \geq 0$), applied on its left.

The cart is identified with the point A. The double pendulum consists of two rigid bars denoted by $\mathcal{B}_1$ and $\mathcal{B}_2$, both of length $\ell > 0$ and mass $m > 0$. Each bar has a point mass at its midpoint: labeled as B for $\mathcal{B}_1$ and C for $\mathcal{B}_2$. The hinge connecting the cart to the bar and the hinge linking the two bars toether are both viscoelastic and characterized by the same elastic stiffness $k > 0$ and viscous damping $c > 0$.

In a generic configuration of the device, the orientations of the bars $\mathcal{B}_1$ and $\mathcal{B}_2$ are determined by the angles $\theta_1 \in [-\pi/2, +\pi/2]$ and $\theta_2 \in [-\pi/2, +\pi/2]$, respectively, both measured from the horizontal axis $\boldsymbol{e}_1$ of the chosen reference frame.

The right endpoint D of the double pendulum, is subject to a *nonholonomic constraint*. This can be visualized as a massless perfect skate, or non-slipping wheel, mounted as to impose that the *velocity of D relative to the point E of the supporting plate*, Figure 3.1, remains orthogonal to the bar $\mathcal{B}_2$ at all times.

The key difference between the structure under consideration and that analyzed by Cazzolli et al. [5] is the restriction on the velocity operated by the nonholonomic constraint, which is relative in the former case and absolute in the latter. In both cases the reaction force $\boldsymbol{p}$ associated to the constraint is a *follower force*, remaining always coaxial with the bar to which it acts.

The mass m_p of the plate is concentrated at point E, Figure 3.1, where it is grounded within the reference frame through a viscoelastic spring of elastic stiffness $k_\mathrm{p} > 0$ and damping $c_\mathrm{p} > 0$. The spring is assumed to be unloaded when E coincides with the point $E_0 = (X_0, 0)$.

3.2.1 The kinematics of the structure

The configuration of the considered structure is defined at each instant of time t through four Lagrangian parameters. The latter are collected in the array $q \equiv (X_\mathrm{c}, \theta_1, \theta_2, X_\mathrm{p})$. Accordingly, the Cartesian coordinates of the points of interest for the system can be expressed

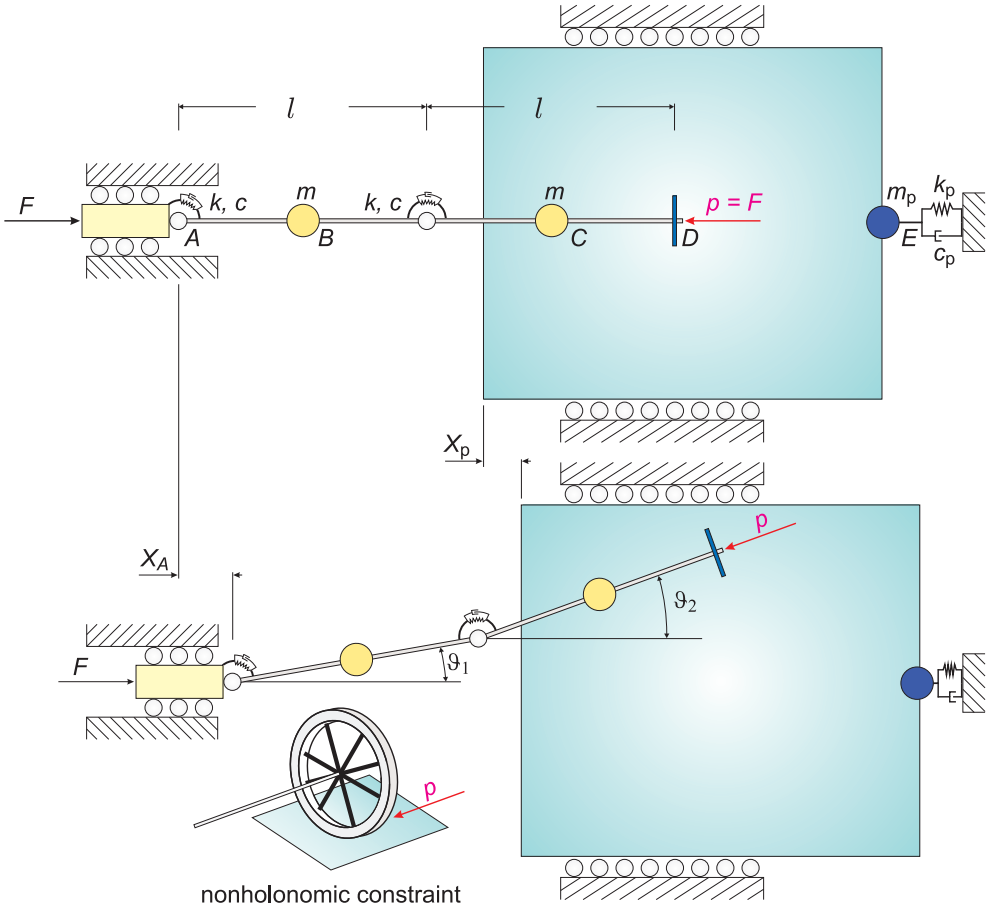

Figure 3.1: The viscoelastic structure under analysis in the straight (upper part) and deformed (lower part) configuration. At the right end of a double pendulum, point D, a nonholonomic constraint such as a non-slipping wheel, is applied. The double pendulum has concentrated masses m attached at points B and C and viscoelastic hinges connecting the bars to each other and the bar on the left to a card (point A of mass m_c), which can only move horizontally without friction. The applied load F is dead, while the reaction force applied by the nonholonomic constraint to a supporting plate is follower. The plate is characterized by a concentrated mass m_c and is linked to the fixed frame through a viscoelastic spring of coefficients k and c.

as

$$A = (X_\mathrm{c},\, 0), \tag{3.1a}$$

$$B = \left(X_\mathrm{c} + \frac{\ell}{2}\cos\theta_1,\, \frac{\ell}{2}\sin\theta_1\right), \tag{3.1b}$$

$$C = \left(X_\mathrm{c} + \ell\cos\theta_1 + \frac{\ell}{2}\cos\theta_2,\, \ell\sin\theta_1 + \frac{\ell}{2}\sin\theta_2\right), \tag{3.1c}$$

$$D = \left(X_\mathrm{c} + \ell\cos\theta_1 + \ell\cos\theta_2,\, \ell\sin\theta_1 + \ell\sin\theta_2\right), \tag{3.1d}$$

$$E = (X_\mathrm{p},\, 0). \tag{3.1e}$$

The 'skate' constraint imposes the velocity of the point E relative to the point D to remain orthogonal to the bar connecting points C and D, a condition leading to

$$(C - D) \cdot \dot{\overline{E - D}} = (C - D) \cdot (\dot{E} - \dot{D}) = 0, \tag{3.2}$$

where $E - D$ and $C - D$ are Euclidean vectors and a dot over a symbol denotes derivative with respect to time.

In terms of the Lagrangian parameters $q \equiv (X_\mathrm{c}, \theta_1, \theta_2, X_\mathrm{p})$ and of the generalized velocities $\dot{q} \equiv (\dot{X}_\mathrm{c}, \dot{\theta}_1, \dot{\theta}_2, \dot{X}_\mathrm{p})$, Equation (3.2) can be rewritten as

$$\hat{\mathcal{C}}(q, \dot{q}) \coloneqq \cos\theta_2(\dot{X}_\mathrm{p} - \dot{X}_\mathrm{c}) + \ell\sin(\theta_1 - \theta_2)\dot{\theta}_1 = 0, \tag{3.3}$$

where the *constraint function* $\hat{\mathcal{C}}(q, \dot{q})$ has been introduced. Note that Equation (3.3) classifies $\hat{\mathcal{C}}(q, \dot{q}) = 0$ as a *nonholonomic constraint*, because it shows that a scalar function $\hat{g}(q)$ does not exist, defined in the sole Lagrangian parameters q for which the time derivative would be equal to $\hat{\mathcal{C}}(q, \dot{q})$.

Introducing the generalized virtual displacements $\delta q \equiv (\delta X_\mathrm{c}, \delta\theta_1, \delta\theta_2, \delta X_\mathrm{p})$, associated with the Lagrangian parameters q, yields the relations with the virtual displacements of the points of interest as

$$\delta A = \delta X_\mathrm{c}\boldsymbol{e}_1, \tag{3.4a}$$

$$\delta B = \left(\delta X_\mathrm{c} - \frac{\ell}{2}\sin\theta_1\,\delta\theta_1\right)\boldsymbol{e}_1 + \frac{\ell}{2}\cos\theta_1\,\delta\theta_1\boldsymbol{e}_2, \tag{3.4b}$$

$$\delta C = \left(\delta X_\mathrm{c} - \ell\sin\theta_1\delta\theta_1 - \frac{\ell}{2}\sin\theta_2\delta\theta_2\right)\boldsymbol{e}_1 + \left(\ell\cos\theta_1\delta\theta_1 + \frac{\ell}{2}\cos\theta_2\delta\theta_2\right)\boldsymbol{e}_2, \tag{3.4c}$$

$$\delta D = \left(\delta X_\mathrm{c} - \ell\sin\theta_1\delta\theta_1 - \ell\sin\theta_2\delta\theta_2\right)\boldsymbol{e}_1 + \left(\ell\cos\theta_1\delta\theta_1 + \ell\cos\theta_2\delta\theta_2\right)\boldsymbol{e}_2, \tag{3.4d}$$

$$\delta E = \delta X_\mathrm{p}\boldsymbol{e}_1. \tag{3.4e}$$

In terms of the virtual displacements, the constraint (3.2) becomes

$$\boldsymbol{p} \cdot (\delta E - \delta D) = 0, \tag{3.5}$$

where

$$\boldsymbol{p} \coloneqq \mu \frac{C-D}{\|C-D\|}, \tag{3.6}$$

and represents the *reaction force* associated with the constraint, which is *follower*, although not of constant modulus as the forces considered in [24, 46]. Note that $\boldsymbol{p}$ admits the representation $\boldsymbol{p} = -\mu(\cos\theta_2\,\boldsymbol{e}_1 + \sin\theta_2\,\boldsymbol{e}_2)$. By employing Equations (3.4c) and (3.4d), the ideality of the constraint expressed in Equation (3.5) can equivalently be recast in the form [9, 18, 20, 55, 56]

$$\hat{\mathcal{A}}(q,\delta q) \coloneqq \cos\theta_2(\delta X_\mathrm{p} - \delta X_\mathrm{c}) + \ell\sin(\theta_1-\theta_2)\delta\theta_1 = 0, \tag{3.7}$$

known as *Chetaev's condition* (see, among others, [35, 57, 58, 59]).

By introducing the 4×1 array q of the Lagrangian parameters, and the 4×1 array $\delta\mathsf{q}$ of the generalized virtual displacements, Equation (3.7) can be written in matrix form as [60]

$$\hat{\mathsf{A}}(\mathsf{q})\delta\mathsf{q} = 0, \qquad \mathsf{A} \equiv \hat{\mathsf{A}}(\mathsf{q}) \coloneqq [-\cos\theta_2, \ell\sin(\theta_1-\theta_2), 0, \cos\theta_2], \tag{3.8}$$

where $\hat{\mathsf{A}}(\mathsf{q})$ is the 1×4 matrix representing the constraint at q. Note that $\hat{\mathsf{A}}(\mathsf{q})$ has maximal rank equal to 1 if and only if $\theta_1 \neq \pm\pi/2$ and $\theta_2 \neq \pm\pi/2$ and that the subset of the configuration space in which $\hat{\mathsf{A}}(\mathsf{q})$ has null rank is a set of null Lebesgue measure [59]. This set is given by $\{X_\mathrm{c}, -\frac{\pi}{2}, -\frac{\pi}{2}, X_\mathrm{p}\} \cup \{X_\mathrm{c}, \frac{\pi}{2}, \frac{\pi}{2}, X_\mathrm{p}\}$ and is defined for arbitrary values of X_c and X_p, thereby identifying two disjoint hyperplanes in the configuration space.

Equation (3.7), or (3.8), *determines* the number of degrees of freedom of the system for any of its configurations. In fact, for any $q = (X_\mathrm{c}, \theta_1, \theta_2, X_\mathrm{p})$ for which $\hat{\mathsf{A}}(\mathsf{q})$ has maximal rank, the number of degrees of freedom coincides with the number of linearly independent generalized virtual displacements that can be extracted from Equation (3.7) or (3.8). Clearly, any linear combination of such linearly independent virtual displacements complies with the nonholonomic constraint [18, 20, 56]. In our case, the degrees of freedom are three, so that the position of the mechanical system is determined by 4 entries $q = (X_\mathrm{c}, \theta_1, \theta_2, X_\mathrm{p})$, but the virtual displacements are determined by 3, because they are limited by the constraint. We refer to the latter as 'degrees of freedom', in the same vein the position of a non-slipping wheel in a plane is determined by 2 parameters, but the virtual displacement is determined by one, its degree of freedom in our nomenclature.

3.2.2 Principle of Virtual Work and structural dynamics

Following [8], the Principle of Virtual Work is enforced, by accounting for the virtual work done by: (i) the dead load $\boldsymbol{F}$ against its dual displacement δA; (ii) the inertial forces associated with the masses located at the points A, B, C, and E; (iii) the elastic and viscous forces generated by the all viscoelastic hinges; (iv) the elastic and viscous forces associated with the axial spring.

The Principle of Virtual Work (d'Alembert–Lagrange Principle) writes as

$$\begin{aligned}&(\boldsymbol{F} - m_\mathrm{c}\ddot{A})\cdot\delta A - m\ddot{B}\cdot\delta B - m\ddot{C}\cdot\delta C - m_\mathrm{p}\ddot{E}\cdot\delta E\\ &-(k\,\theta_1 + c\,\dot{\theta}_1)\,\delta\theta_1 - [k\,(\theta_2-\theta_1) + c\,(\dot{\theta}_2-\dot{\theta}_1)](\delta\theta_2-\delta\theta_1) - [c_\mathrm{p}\dot{E} + k_\mathrm{p}(E-E_0)]\cdot\delta E = 0.\end{aligned} \tag{3.9}$$

The virtual displacements δA, δB, δC, δE depend on the four generalized virtual displacements δq, restricted by Chetaev's condition (3.7). Based on expressions (3.4a)–(3.4e),

Equation (3.9) can be rewritten in terms of the generalized virtual displacements δq as

$$\mathcal{F}_{X_\mathrm{c}}\delta X_\mathrm{c} + \mathcal{F}_{\theta_1}\delta\theta_1 + \mathcal{F}_{\theta_2}\delta\theta_2 + \mathcal{F}_{X_\mathrm{p}}\delta X_\mathrm{p} = 0, \tag{3.10}$$

where $\mathcal{F}_{X_\mathrm{c}}$, $\mathcal{F}_{\theta_1}$, $\mathcal{F}_{\theta_2}$, and $\mathcal{F}_{X_\mathrm{p}}$ are the active parts of the Lagrange generalized forces

$$\mathcal{F}_{X_\mathrm{c}} \coloneqq F - (m_\mathrm{c}+2m)\ddot{X}_\mathrm{c} + \frac{3}{2}m\ell\,\dot{\theta}_1^2\cos\theta_1 + \frac{3}{2}m\ell\,\ddot{\theta}_1\sin\theta_1 + \frac{1}{2}m\ell\,\dot{\theta}_2^2\cos\theta_2 + \frac{1}{2}m\ell\,\ddot{\theta}_2\sin\theta_2, \tag{3.11a}$$

$$\mathcal{F}_{\theta_1} \coloneqq -\frac{1}{2}m\ell^2\sin(\theta_1-\theta_2)\dot{\theta}_2^2 - k(2\theta_1-\theta_2) - c(2\dot{\theta}_1-\dot{\theta}_2) + \frac{3}{2}m\ell\sin\theta_1\,\ddot{X}_\mathrm{c} - \frac{5}{4}m\ell^2\ddot{\theta}_1 - \frac{1}{2}m\ell^2\cos(\theta_1-\theta_2)\ddot{\theta}_2, \tag{3.11b}$$

$$\mathcal{F}_{\theta_2} \coloneqq \frac{1}{2}m\ell^2\sin(\theta_1-\theta_2)\dot{\theta}_1^2 - k(\theta_2-\theta_1) - c(\dot{\theta}_2-\dot{\theta}_1) + \frac{1}{2}m\ell\sin\theta_2\,\ddot{X}_\mathrm{c} - \frac{1}{2}m\ell^2\cos(\theta_1-\theta_2)\ddot{\theta}_1 - \frac{1}{4}m\ell^2\ddot{\theta}_2, \tag{3.11c}$$

$$\mathcal{F}_{X_\mathrm{p}} \coloneqq -k_\mathrm{p}(X_\mathrm{p}-X_0) - c_\mathrm{p}\dot{X}_\mathrm{p} - m_\mathrm{p}\ddot{X}_\mathrm{p}. \tag{3.11d}$$

The Lagrange generalized forces can be gathered in the vector $\mathcal{F} \coloneqq (\mathcal{F}_{X_\mathrm{c}}, \mathcal{F}_{\theta_1}, \mathcal{F}_{\theta_2}, \mathcal{F}_{X_\mathrm{p}})$ and are dual to the virtual displacements $\delta q = (\delta X_\mathrm{c}, \delta\theta_1, \delta\theta_2, \delta X_\mathrm{p})$, so that Equation (3.10) admits the reduced expression $\mathcal{F}\delta q = 0$.

Remark 9 (A prelude to the 'dynamic condensation' approach)**.** *It is worth noticing that, since the elements of δq must comply with Chetaev's condition (3.7), they are not linearly independent. Consequently, the expression (3.10) of the Principle of Virtual Work cannot be converted into a set of four linearly independent equations requiring the vanishing of each of the Lagrange generalized forces $\mathcal{F}_{X_\mathrm{c}}$, $\mathcal{F}_{\theta_1}$, $\mathcal{F}_{\theta_2}$, and $\mathcal{F}_{X_\mathrm{p}}$. Use of Equation (3.7) to express one of the virtual displacements, for instance, δX_c, as a function of the others, leads*

$$\delta X_\mathrm{c} = \delta X_\mathrm{p} + \hat{g}(\theta_1,\theta_2)\delta\theta_1, \qquad \textit{with} \qquad \hat{g}(\theta_1,\theta_2) \coloneqq \frac{\ell\sin(\theta_1-\theta_2)}{\cos\theta_2}, \tag{3.12}$$

and Equation (3.10) becomes

$$[\mathcal{F}_{X_\mathrm{c}} + \mathcal{F}_{X_\mathrm{p}}]\delta X_\mathrm{c} + [\mathcal{F}_{\theta_1} + \hat{g}(\theta_1,\theta_2)\mathcal{F}_{X_\mathrm{c}}]\delta\theta_1 + \mathcal{F}_{\theta_2}\delta\theta_2 = 0. \tag{3.13}$$

In Equation (3.13), the virtual displacements δX_c, $\delta\theta_1$, and $\delta\theta_2$ are linearly independent, which leads to the vanishing of the following combinations of generalized forces:

$$\mathcal{F}_{X_\mathrm{c}} + \mathcal{F}_{X_\mathrm{p}} = 0, \tag{3.14a}$$

$$\mathcal{F}_{\theta_1} + \hat{g}(\theta_1,\theta_2)\mathcal{F}_{X_\mathrm{c}} = 0, \tag{3.14b}$$

$$\mathcal{F}_{\theta_2} = 0. \tag{3.14c}$$

Equations (3.14a)–(3.14c) set the stage for the reduction procedure outlined in Section 3.3.1. The set of the three Equations (3.14a)–(3.14c) is not sufficient to determine the evolution of the four Lagrangian parameters X_c, θ_1, θ_2, and X_p, so that the constraint (3.7) is also needed, which allows the determination of the Lagrange multiplier μ.

For computational convenience the technique introduced in [18], and later used in [38, 61, 62, 63, 64] is followed. In particular, it is expedient to introduce a 'fictitious' virtual displacement $\delta\mu$ associated with the Lagrange multiplier μ, to yield

$$\mu\,\hat{\mathcal{A}}(q,\delta q) = -\mu\cos\theta_2\,\delta X_\mathrm{c} + \mu\ell\sin(\theta_1-\theta_2)\delta\theta_1 + \mu\cos\theta_2\,\delta X_\mathrm{p} = 0, \tag{3.15a}$$

$$\tau_\mathrm{c}\,\hat{\mathcal{C}}(q,\dot{q})\,\delta\mu = [-\cos\theta_2\,(\dot{X}_\mathrm{c}\tau_\mathrm{c}) + \ell\sin(\theta_1-\theta_2)(\dot{\theta}_1\tau_\mathrm{c}) + \cos\theta_2(\dot{X}_\mathrm{p}\tau_\mathrm{c})]\delta\mu = 0. \tag{3.15b}$$

Note the introduction of the characteristic time τ_c, so that Equation (3.15b) has physical dimensions consistent with Equation (3.9) [62].

Hence, by summing the constraint contributions in Equations (3.15a) and (3.15b) to Equation (3.10), we obtain the *constrained* version of the Principle of Virtual Work

$$[\mathcal{F}_{X_c}-\mu\cos\theta_2]\delta X_c+[\mathcal{F}_{\theta_1}+\mu\ell\sin(\theta_1-\theta_2)]\delta\theta_1+\mathcal{F}_{\theta_2}\delta\theta_2+[\mathcal{F}_{X_p}+\mu\cos\theta_2]\delta X_p+\tau_c\,\hat{\mathcal{C}}(q,\dot{q})\,\delta\mu=0. \tag{3.16}$$

Invoking arbitrariness of the entries of δq, as well as $\delta\mu$, the equations governing the dynamics of the structure are obtained

$$\mathcal{F}_{X_c}-\mu\cos\theta_2=0, \tag{3.17a}$$
$$\mathcal{F}_{\theta_1}+\mu\ell\sin(\theta_1-\theta_2)=0, \tag{3.17b}$$
$$\mathcal{F}_{\theta_2}=0, \tag{3.17c}$$
$$\mathcal{F}_{X_p}+\mu\cos\theta_2=0, \tag{3.17d}$$
$$\hat{\mathcal{C}}(q,\dot{q})=0. \tag{3.17e}$$

For computational purposes, Equation (3.17e) is differentiated with respect to time (as in [36]) and recast in the form

$$\ddot{X}_c\cos\theta_2-\ell\ddot{\theta}_1\sin(\theta_1-\theta_2)-\ddot{X}_p\cos\theta_2=\dot{\theta}_2(\dot{X}_c-\dot{X}_p)\sin\theta_2+\ell\dot{\theta}_1(\dot{\theta}_1-\dot{\theta}_2)\cos(\theta_1-\theta_2). \tag{3.18}$$

Equations (3.17a)–(3.17d) and (3.18) feature nine mechanical parameters, including the dead load F applied to the cart,

$$\mathcal{P}\coloneqq\{m_c;\ m,c,k,\ell;\ m_p,c_p,k_p;\ F\}, \tag{3.19}$$

and additionally depend on the referential position X_0 of the plate. However, the nondimensionalization procedure, performed via the mappings

$$X_c\mapsto\frac{X_c}{\ell},\qquad X_p\mapsto\frac{X_p}{\ell},\qquad \mu\mapsto\frac{\mu\ell}{k},\qquad t\mapsto\frac{t}{\sqrt{\frac{m\ell^2}{k}}}, \tag{3.20}$$

extracts the *six* dimensionless parameters [5]

$$\tilde{m}_c\coloneqq\frac{2m+m_c}{m}>2,\quad \tilde{c}\coloneqq\frac{c}{\ell\sqrt{mk}},\quad \tilde{F}\coloneqq\frac{F\ell}{k},\quad \tilde{m}_p\coloneqq\frac{m_p}{m},\quad \tilde{k}_p\coloneqq\frac{k_p\ell^2}{k},\quad \tilde{c}_p\coloneqq\frac{c_p\ell}{\sqrt{mk}}, \tag{3.21}$$

which can be regarded as functions of the *three* independent parameters m, k, and ℓ. In the following, additional notation is not introduced to indicate the dimensionless quantities X_c/ℓ, X_p/ℓ, $\mu\ell/k$, and $t/\sqrt{m\ell^2/k}$, rather, the variables are renamed as X_c, X_p, μ, and t, so that differentiation is performed with respect to the dimensionless time variable $t/\sqrt{m\ell^2/k}$. The equations of dynamic equilibrium are rewritten in dimensionless form as

$$\tilde{m}_c\ddot{X}_c-\frac{3}{2}(\sin\theta_1)\ddot{\theta}_1-\frac{1}{2}(\sin\theta_2)\ddot{\theta}_2-\frac{3}{2}(\cos\theta_1)\dot{\theta}_1^2-\frac{1}{2}(\cos\theta_2)\dot{\theta}_2^2=\tilde{F}-\mu\cos\theta_2, \tag{3.22a}$$
$$-\frac{3}{2}(\sin\theta_1)\ddot{X}_c+\frac{5}{4}\ddot{\theta}_1+\frac{1}{2}\cos(\theta_1-\theta_2)\ddot{\theta}_2+\frac{1}{2}\sin(\theta_1-\theta_2)\dot{\theta}_2^2=-\tilde{c}(2\dot{\theta}_1-\dot{\theta}_2)-(2\theta_1-\theta_2)+\mu\sin(\theta_1-\theta_2), \tag{3.22b}$$
$$-\frac{1}{2}(\sin\theta_2)\ddot{X}_c+\frac{1}{2}\cos(\theta_1-\theta_2)\ddot{\theta}_1+\frac{1}{4}\ddot{\theta}_2-\frac{1}{2}\sin(\theta_1-\theta_2)\dot{\theta}_1^2=-\tilde{c}(\dot{\theta}_2-\dot{\theta}_1)-(\theta_2-\theta_1), \tag{3.22c}$$
$$\tilde{m}_p\ddot{X}_p+\tilde{c}_p\dot{X}_p+\tilde{k}_p(X_p-X_0)=\mu\cos\theta_2, \tag{3.22d}$$
$$\ddot{X}_c\cos\theta_2-\ddot{\theta}_1\sin(\theta_1-\theta_2)-\ddot{X}_p\cos\theta_2=\dot{\theta}_2(\dot{X}_c-\dot{X}_p)\sin\theta_2+\dot{\theta}_1\cos(\theta_1-\theta_2)(\dot{\theta}_1-\dot{\theta}_2). \tag{3.22e}$$

3.3 Stability analysis: flutter instability and bifurcations

A stability analysis is to be developed of structure outlined in Figure 3.1, initiating from static equilibrium [5, 4, 9, 37]. To this end, all accelerations and velocities are set equal to zero in Equations (3.22a)–(3.22e), and the 'surviving' algebraic equations lead to

$$X_{\mathrm{c}} = X_{\mathrm{c0}}, \qquad \theta_1 = \theta_2 = 0, \qquad X_{\mathrm{p}} = X_0 + \tilde{F}/\tilde{k}_{\mathrm{p}}, \qquad \mu = \tilde{F}, \tag{3.23}$$

where X_{c0} and X_{c} are the dimensionless referential and current positions of the cart, respectively. When not fixed, X_{c0} may assume any value, so a *family* of equivalent equilibrium configurations $(X_{\mathrm{c0}}, 0, 0, X_0 + \tilde{F}/\tilde{k}_{\mathrm{p}})$ is found, all characterized by $\mu = \tilde{F}$. But fixing X_{c0} leads to a unique static equilibrium configuration, defined as

$$q_{\mathrm{e}} \coloneqq (X_{\mathrm{c0}}, 0, 0, X_0 + \tilde{F}/\tilde{k}_{\mathrm{p}}), \qquad \mu_{\mathrm{e}} \coloneqq \tilde{F}. \tag{3.24}$$

For the sake of simplicity, we choose $X_{\mathrm{c0}} = 0$. The resulting unique equilibrium is then achieved when: (i) the two bars forming the double pendulum are aligned horizontally; (ii) the axial spring attached to the plate is compressed enough to balance the dead load.

Before proceeding with the stability analysis, it is important to notice that, if the system (3.22a)–(3.22e) were to be studied as currently formulated, the Jacobian matrix resulting from linearizing Equations (3.22a)–(3.22e) around the values q_{e} and μ_{e} at equilibrium and for any value of $\tilde{F}$, would be singular. This is again a direct consequence of the linearization of the nonholonomic constraint. The same feature was unfolded in the previous chapter in Section 2.3.1, where there is the existence of a vanishing root in Equation (2.30) with algebraic multiplicity two. Once again, the reader can be referred to Neimark and Fufaev [9, Page 267], where it is stated that the resulting singular Jacobian does concern itself with a loss of stability for nonholonomic systems [9].

This singularity does however preclude the further analysis of limit-cycle stability, which is essential for the developments in Section 3.3.4. Additional details on the linearized behavior prior to the condensation are deferred to Appendix A.1.

The singularity in the jacobian matrix is removed by applying a dynamic condensation method to Equations (3.22a)–(3.22e), yielding a reduced system that is subsequently formulated in state-variable form using the Schur complement method [35, 36]. This is carried out in the next section and the linear stability analysis can then be performed on the resulting reduced set of equations.

3.3.1 The dynamic condensation procedure and Schur's complement method

The dynamic condensation of Equations (3.22a)–(3.22e) is carried out as follows. Equation (3.22a) is solved for $\ddot{X}_{\mathrm{c}}$,

$$\ddot{X}_{\mathrm{c}} = \frac{1}{\tilde{m}_{\mathrm{c}}}\left[\frac{3}{2}(\sin\theta_1)\ddot{\theta}_1 + \frac{1}{2}(\sin\theta_2)\ddot{\theta}_2 + \frac{3}{2}(\cos\theta_1)\dot{\theta}_1^2 + \frac{1}{2}(\cos\theta_2)\dot{\theta}_2^2 + \tilde{F} - \mu\cos\theta_2\right]. \tag{3.25}$$

Then, we substitute the resulting expression for $\ddot{X}_{\mathrm{c}}$ into Equations (3.22b)–(3.22e). The velocity $\dot{X}_{\mathrm{c}}$ is eliminated from Equation (3.22e) using the constraint (3.17e) in its dimensionless form,

$$\dot{X}_{\mathrm{c}} = \frac{\sin(\theta_1 - \theta_2)}{\cos\theta_2}\dot{\theta}_1 + \dot{X}_{\mathrm{p}}, \qquad \theta_2 \neq \frac{\pi}{2}. \tag{3.26}$$

Next, we insert Equation (3.26) into (3.22e), which amounts to rewriting the constraint in an equivalent form that depends on θ_1, θ_2, and X_p, on the derivatives of these functions up to the second order, and on μ.

The *condensation* procedure makes it possible to seek solutions of a reduced system comprising only four equations in the unknowns θ_1, θ_2, X_p, and μ, while X_c can be computed *a posteriori* by solving the second-order differential equation (3.25), in which the right-hand side is known once θ_1, θ_2, X_p and μ are computed.

In order to decouple the *condensed* system of equations from the computation of the Lagrange multiplier, a generalization of Schur's complement method is introduced.

On introducing the reduced 3×1 array $\mathsf{q}_\mathsf{r} \coloneqq \{\theta_1, \theta_2, X_\mathrm{p}\}^\mathrm{T}$ of unknown Lagrangian parameters, the *condensed* equations are rewritten in a block-wise form that generalizes the expression reported in [35, 36],

$$\begin{bmatrix} \hat{\mathsf{M}}_\mathsf{r}(\mathsf{q}_\mathsf{r}) & -[\hat{\mathsf{B}}_\mathsf{r}(\mathsf{q}_\mathsf{r})]^\mathrm{T} \\ -\hat{\mathsf{A}}_\mathsf{r}(\mathsf{q}_\mathsf{r}) & \hat{\mathsf{C}}_\mathsf{r}(\mathsf{q}_\mathsf{r}) \end{bmatrix} \begin{Bmatrix} \ddot{\mathsf{q}}_\mathsf{r} \\ \mu_\mathsf{r} \end{Bmatrix} = \begin{Bmatrix} \hat{\mathsf{b}}_{\mathsf{q}\,\mathsf{r}}(\mathsf{q}_\mathsf{r}, \dot{\mathsf{q}}_\mathsf{r}) \\ \hat{\mathsf{b}}_{\mathsf{c}\,\mathsf{r}}(\mathsf{q}_\mathsf{r}, \dot{\mathsf{q}}_\mathsf{r}) \end{Bmatrix}. \tag{3.27}$$

The analytical expressions of the matrices and of the arrays in Equation (3.27) are reported in Appendix A.2, where some further insights on the method are provided.

Following [35, 36, 38], the Schur complement characterizing the left-hand side of Equation (3.27) reads $\mathsf{S}_\mathsf{r} \coloneqq \mathsf{C}_\mathsf{r} - \mathsf{A}_\mathsf{r}\mathsf{M}_\mathsf{r}^{-1}\mathsf{B}_\mathsf{r}$, and the *condensed* system can be rewritten in normal form as

$$\ddot{\mathsf{q}}_\mathsf{r} = \mathsf{M}_\mathsf{r}^{-1}\mathsf{B}_\mathsf{r}\,\mathsf{S}_\mathsf{r}^{-1}\left(\mathsf{A}_\mathsf{r}\mathsf{M}_\mathsf{r}^{-1}\mathsf{b}_{\mathsf{q}\,\mathsf{r}} + \mathsf{b}_{\mathsf{c}\,\mathsf{r}}\right) + \mathsf{M}_\mathsf{r}^{-1}\mathsf{b}_{\mathsf{c}\,\mathsf{r}}, \tag{3.28a}$$

$$\mu_\mathsf{r} = -\mathsf{S}_\mathsf{r}^{-1}[\mathsf{A}_\mathsf{r}\mathsf{M}_\mathsf{r}^{-1}\mathsf{b}_{\mathsf{q}\,\mathsf{r}} + \mathsf{b}_{\mathsf{c}\,\mathsf{r}}]. \tag{3.28b}$$

Equation (3.28a) defines three coupled second-order ordinary differential equations for θ_1, θ_2, and X_p, with the Lagrange multiplier μ computed *a posteriori* from Equation (3.28b). When supplied with initial conditions for θ_1, θ_2, and X_p, Equation (3.28a) defines a well-posed Cauchy problem.

A further step is obtained by introducing the *state-variable formalism*, which allows Equation (3.28a) to be recast as six first-order ordinary differential equations. This procedure is not applied directly to the dynamic equations (3.22a)–(3.22e). Rather, it is applied *after* condensing the dynamic equation associated with X_c into the others and *after* decoupling the computation of the Lagrange multiplier from that of θ_1, θ_2, and X_p.

Some consequences of this strategy on the stability analysis are explored in Section 3.3.2. Hence, upon setting $Y_1 \coloneqq \theta_1$, $Y_2 \coloneqq \theta_2$, $Y_3 \coloneqq X_\mathrm{p}$, $Y_4 \coloneqq \dot{\theta}_1 \equiv \dot{Y}_1$, $Y_5 \coloneqq \dot{\theta}_2 \equiv \dot{Y}_2$, and $Y_6 \coloneqq \dot{X}_\mathrm{p} \equiv \dot{Y}_3$, and introducing the 6×1 arrays $\mathsf{Y} = \{Y_1, Y_2, Y_3, Y_4, Y_5, Y_6\}^\mathrm{T}$, Equation (3.28a) assumes the form

$$\dot{\mathsf{Y}} = \mathsf{h}(\mathsf{Y}; \tilde{F}) = \begin{Bmatrix} h_1(Y_1, \cdots, Y_6; \tilde{F}) \\ h_2(Y_1, \cdots, Y_6; \tilde{F}) \\ h_3(Y_1, \cdots, Y_6; \tilde{F}) \\ h_4(Y_1, \cdots, Y_6; \tilde{F}) \\ h_5(Y_1, \cdots, Y_6; \tilde{F}) \\ h_6(Y_1, \cdots, Y_6; \tilde{F}) \end{Bmatrix} = \begin{Bmatrix} Y_4 \\ Y_5 \\ Y_6 \\ h_4(Y_1, \cdots, Y_6; \tilde{F}) \\ h_5(Y_1, \cdots, Y_6; \tilde{F}) \\ h_6(Y_1, \cdots, Y_6; \tilde{F}) \end{Bmatrix}, \tag{3.29}$$

where h_4, h_5 and h_6 are the three components of the right-hand side of Equation (3.28a), written in the state variable formalism.

3.3.2 Dynamic linearized equations from the reduced formulation

Focusing on the stability of the equilibrium configuration q_e, Equation (3.24), the standard procedures can be followed for the dynamical system described by Equation (3.29). The first-order Taylor expansion of h at the equilibrium state Y_e, for any $\tilde{F}$ and $\|\mathsf{Y}-\mathsf{Y}_\mathrm{e}\|_2 \to 0$, is

$$[\mathsf{h}(\mathsf{Y};\tilde{F})]_j = \underbrace{[\mathsf{h}(\mathsf{Y}_\mathrm{e};\tilde{F})]_j}_{=0} + \sum_{k=1}^{6} \underbrace{\left[\frac{\partial h_j}{\partial Y_k}(\mathsf{Y}_\mathrm{e};\tilde{F})\right]}_{=:[\mathsf{H}_\mathrm{e}]_{jk}} [Y_k - (Y_\mathrm{e})_k] + o(\|\mathsf{Y}-\mathsf{Y}_\mathrm{e}\|_2), \tag{3.30}$$

where $\|\cdot\|_2$ denotes the norm Euclidean of the relevant argument.

The 6×6 Jacobian matrix at equilibrium $\mathsf{H}_\mathrm{e} \equiv \hat{\mathsf{H}}(\mathsf{Y}_\mathrm{e};\tilde{F})$ features six eigenvalues that are computed as the roots of the characteristic equation

$$P(\omega;\tilde{F}) = \det(\mathsf{H}_\mathrm{e} - \omega \mathsf{I}_6) = 0, \quad \Leftrightarrow \quad Q(\omega;\tilde{F})\,(\tilde{k}_\mathrm{p} + \tilde{c}_\mathrm{p}\,\omega + (\tilde{m}_\mathrm{p}+\tilde{m}_\mathrm{c})\,\omega^2) = 0, \tag{3.31}$$

defining the eigenvalues (roots) $\omega_1,\ldots,\omega_6$ as functions of $\tilde{F}$, which can be written compactly as $\omega_j = \hat{\omega}_j(\tilde{F})$, $j=1,\ldots,6$. The function $Q(\omega;\tilde{F})$ is the fourth-order polynomial

$$Q(\omega;\tilde{F}) \coloneqq a_0\omega^4 + a_1\omega^3 + a_2\omega^2 + a_3\omega + a_4, \tag{3.32}$$

where the coefficients a_0, a_1, a_2, a_3, a_4 are all real and given by

$$a_0 = 1, \qquad a_1 = 44\,\tilde{c}, \qquad a_2 = 44 + 16\,\tilde{c}^2 - 12\tilde{F}, \qquad a_3 = 32\,\tilde{c}, \qquad a_4 = 16. \tag{3.33}$$

Again, it can be emphasized here that the resulting polynomial in Equation (3.32), is exactly that which is shown in the first chapter under the review of Ziegler's double pendulum. Implying, ultimately, that the underlying stability of the system is the same. Here, $\tilde{F}$ now plays the role of the follower force shown in 1.1. Note that whin this procedure, we can single out the factors pertaining to Ziegler's double pendulum (represented by $Q(\omega;\tilde{F})$) and and the the plate-and-cart subsystem (represented by the term multiplying $\tilde{k}_\mathrm{p}+\tilde{c}_\mathrm{p}\,\omega+(\tilde{m}_\mathrm{p}+\tilde{m}_\mathrm{c})\,\omega^2$). This factorization/decoupling is further emphasized by the linearisation procedure shown in Appendix A.1, carried out prior to the dynamic condensation.

3.3.3 Coupling of a Hopf bifurcation with a damped harmonic oscillator

The four roots of $Q(\omega;\tilde{F})$, corresponding to the four eigenvalues of the double pendulum, are shown in Figure 1.2b. Note that in the diagram, and with a small abuse of notation, the four roots $\omega_{1\ldots4}$ are synonymous with $\lambda_{1\ldots4}$. At $\tilde{F} = \tilde{F}_\mathrm{flu}(\tilde{c})$, the coexistence of *a pair of purely imaginary complex conjugate eigenvalues* (triangles and squares) and *a pair of complex conjugate eigenvalues with negative real part* (diamonds and circles) in Figure 1.2b indicates the onset of a Hopf bifurcation [39]. However, Equation (3.31) indicates that also the roots of the polynomial multiplying $Q(\omega;\tilde{F})$ must be considered in order to ascertain whether a Hopf bifurcation occurs for the whole system, and whether such bifurcation is accompanied by phenomena associated with the remaining eigenvalues. One such phenomenon is *resonance*, which may arise when the imaginary parts of two or more eigenvalues are close, coincide, or stand in an integer ratio. This issue is discussed in Section 3.4.

When Equation (3.31) is evaluated at $\tilde{F} = \tilde{F}_\mathrm{flu}(\tilde{c})$, polynomial $Q(\omega;\tilde{F})$ simplifies to

$$(22 + 44\,\tilde{c}\,\omega + \omega^2)(8 + 11\omega^2) = 0, \tag{3.34}$$

and the eigenvalues of $\mathsf{H}_\mathrm{e} \equiv \hat{\mathsf{H}}(\mathsf{Y}_\mathrm{e}; \tilde{F}_\mathrm{flu}(\tilde{c}))$ are the roots of the characteristic equation

$$P(\omega; \tilde{F}_\mathrm{flu}(\tilde{c})) = \frac{(22 + 44\,\tilde{c}\,\omega + \omega^2)(8 + 11\omega^2)(\tilde{k}_\mathrm{p} + \tilde{c}_\mathrm{p}\omega + (\tilde{m}_\mathrm{c} + \tilde{m}_\mathrm{p})\,\omega^2)}{11(\tilde{m}_\mathrm{c} + \tilde{m}_\mathrm{p})} = 0, \tag{3.35}$$

which are

$$\underbrace{\omega_{1,4} = -22\tilde{c} \pm \sqrt{-22 + (22\tilde{c})^2}, \quad \omega_{2,3} = \pm i\sqrt{\frac{8}{11}},}_{\text{double pendulum}} \qquad \underbrace{\omega_{5,6} = -\,\delta_\mathrm{p} \pm i\tilde{\omega}_\mathrm{pc},}_{\text{plate-and-cart}} \tag{3.36}$$

where δ_p and $\tilde{\omega}_\mathrm{pc}$ are

$$\tilde{\omega}_\mathrm{pc} \coloneqq \sqrt{\tilde{\Omega}_\mathrm{pc}^2 - \delta_\mathrm{p}^2} > 0, \qquad \tilde{\Omega}_\mathrm{pc} \coloneqq \sqrt{\frac{\tilde{k}_\mathrm{p}}{\tilde{m}_\mathrm{p} + \tilde{m}_\mathrm{c}}} > 0, \qquad \delta_\mathrm{p} \coloneqq \frac{\tilde{c}_\mathrm{p}}{2(\tilde{m}_\mathrm{p} + \tilde{m}_\mathrm{c})} > 0, \tag{3.37}$$

holding under the assumption that $\tilde{\Omega}_\mathrm{pc}^2 - \delta_\mathrm{p}^2 > 0$, which is necessary to impose periodically damped oscillations for the plate.

The first four roots of Equation (3.36), $\omega_1, ..., \omega_4$, are also roots of Equation (3.34) and refer to the double pendulum, which experiences flutter instability.

The imaginary part of the fifth and of the sixth root ω_5 and ω_6 corresponds to the frequency of the damped linear oscillator represented by the plate-and-cart subsystem, which coincides with $\tilde{\omega}_\mathrm{pc}$ reported in Equation $(3.37)_1$. The real part of ω_5 and ω_6 is given by $-\delta_\mathrm{p}$, with $\delta_\mathrm{p} > 0$ being defined in Equation $(3.37)_3$. The presence of δ_p, which stems from the damping $\tilde{c}_\mathrm{p}$, makes the number of purely imaginary and complex conjugate roots of $P(\omega; \tilde{F}_\mathrm{flu}(\tilde{c}))$ equal to two, ω_2 and ω_3.

We can conclude that the structure as a whole experiences a Hopf bifurcation at $\tilde{F} = \tilde{F}_\mathrm{flu}(\tilde{c})$, allowing for the generation of periodic orbits.

Note that, when the damping applied to the plate is neglected, $\delta_\mathrm{p} = 0$, the eigenvalues ω_5 and ω_6 become purely imaginary and complex conjugate, $\omega_5 = -i\tilde{\Omega}_\mathrm{pc}$ and $\omega_6 = +i\tilde{\Omega}_\mathrm{pc}$. Hence, although the plate-and-cart subsystem behaves as a harmonic oscillator, the presence of another pair of purely imaginary and complex conjugate eigenvalues violates the Hopf condition, which requires that only one such pair of eigenvalues exists.

3.3.4 The computation of the first Lyapunov coefficient

Since the system under study fulfills the criterion for a Hopf bifurcation at $\tilde{F} = \tilde{F}_\mathrm{flu}(\tilde{c})$, we expect to find limit cycle solutions for values of $\tilde{F}$ exceeding $\tilde{F}_\mathrm{flu}(\tilde{c})$ but less than $\tilde{F}_\mathrm{div}(\tilde{c})$. Moreover, when limit cycles exist, it has to be ascertained whether the Hopf bifurcation which they originate from is supercritical or subcritical. It is *supercritical* when the limit cycles are *stable* and *subcritical* when they are *unstable*. In the former, the trajectories of the solution in the phase space will converge to these limit cycles, and, in the latter, the trajectories in the phase space will diverge from these limit cycles.

To distinguish between the sub- and supercritical Hopf bifurcation, the computation of the *first Lyapunov coefficient* is employed [39]. It determines the influence that higher order terms in the Taylor expansion of h have on the bifurcation (trajectories), and its sign provides an index into this behavior. In particular, the Hopf bifurcation is classified as supercritical if the sign is negative and subcritical when positive.

We compute the *first Lyapunov coefficient* $\ell_1(\mathsf{Y}_\mathrm{e})$ associated with the equilibrium state Y_e of the (reduced) dynamical system $\dot{\mathsf{Y}} = \mathsf{h}(\mathsf{Y}; \tilde{F})$, Equation (3.29), by following Kuznetsov [39, Equation (5.34), Page 197]. By denoting $\omega_0 \coloneqq \mathrm{Im}[\omega_3] > 0$, we obtain

$$\begin{aligned}\ell_1(\mathsf{Y}_\mathrm{e}) = \frac{1}{2\omega_0}\mathrm{Re}[\langle \mathsf{v}|\mathsf{C}_\mathrm{e}(\mathsf{u},\mathsf{u},\bar{\mathsf{u}})\rangle - 2\langle \mathsf{v}|\mathsf{B}_\mathrm{e}(\mathsf{u},\mathsf{H}_\mathrm{e}^{-1}\mathsf{B}_\mathrm{e}(\mathsf{u},\bar{\mathsf{u}}))\rangle \\ + \langle \mathsf{v}|\mathsf{B}_\mathrm{e}(\bar{\mathsf{u}},(2i\omega_0\mathsf{I}_6 - \mathsf{H}_\mathrm{e})^{-1}\mathsf{B}_\mathrm{e}(\mathsf{u},\mathsf{u}))\rangle],\end{aligned} \tag{3.38}$$

where $\mathsf{H}_\mathrm{e} \equiv \hat{\mathsf{H}}(\mathsf{Y}_\mathrm{e}; \tilde{F}_\mathrm{flu}(\tilde{c}))$ is the Jacobian matrix, Equation (3.30), evaluated at $\tilde{F}_\mathrm{flu}(\tilde{c})$, u and v are its the left and the right eigenvectors, $\mathsf{H}_\mathrm{e}\mathsf{u} = i\omega_0\mathsf{u}$ and $\mathsf{H}_\mathrm{e}^\mathrm{T}\mathsf{v} = -i\omega_0\mathsf{v}$, both are normalized as $\langle \mathsf{v}|\mathsf{u}\rangle = 1$. Finally, B_e and $Eq\mathsf{C}_\mathrm{e}$ are defined component-wise as [39]

$$[\mathsf{B}_\mathrm{e}]_{jlk} \coloneqq \frac{\partial^2 h_j}{\partial Y_l \partial Y_k}(\mathsf{Y}_\mathrm{e}; \tilde{F}_\mathrm{flu}(\tilde{c})), \quad [\mathsf{C}_\mathrm{e}]_{jlkp} \coloneqq \frac{\partial^3 h_j}{\partial Y_l \partial Y_k \partial Y_p}(\mathsf{Y}_\mathrm{e}; \tilde{F}_\mathrm{flu}(\tilde{c})), \quad j,l,k,p = 1,\ldots,6, \tag{3.39}$$

where h is assumed to be at least of class C^3 in Y. Note that B_e is symmetric in its second pair of indices, $[\mathsf{B}_\mathrm{e}]_{jlk} = [\mathsf{B}_\mathrm{e}]_{jkl}$, and C_e is symmetric in its second triad of indices, $[\mathsf{C}_\mathrm{e}]_{jlkp} = [\mathsf{C}_\mathrm{e}]_{jklp} = [\mathsf{C}_\mathrm{e}]_{jlpk} = [\mathsf{C}_\mathrm{e}]_{jpkl}$. When B_e and C_e operate on complex vectors of $\mathbb{C}^6$ (this is needed because the eigenvectors of H_e are complex, in general), they are defined as

$$\begin{aligned}&\mathsf{B}_\mathrm{e} : \mathbb{C}^6 \times \mathbb{C}^6 \to \mathbb{C}^6, \\ &\mathsf{B}_\mathrm{e}(\mathsf{U},\mathsf{V}) = [\mathsf{B}_\mathrm{e}(\mathsf{U}_\mathrm{R},\mathsf{V}_\mathrm{R}) - \mathsf{B}_\mathrm{e}(\mathsf{U}_\mathrm{I},\mathsf{V}_\mathrm{I})] + i\,[\mathsf{B}_\mathrm{e}(\mathsf{U}_\mathrm{R},\mathsf{V}_\mathrm{I}) + \mathsf{B}_\mathrm{e}(\mathsf{U}_\mathrm{I},\mathsf{V}_\mathrm{R})]\,,\end{aligned} \tag{3.40a}$$

$$\begin{aligned}&\mathsf{C}_\mathrm{e} : \mathbb{C}^6 \times \mathbb{C}^6 \times \mathbb{C}^6 \to \mathbb{C}^6, \\ &\mathsf{C}_\mathrm{e}(\mathsf{U},\mathsf{V},\mathsf{W}) = [\mathsf{C}_\mathrm{e}(\mathsf{U}_\mathrm{R},\mathsf{V}_\mathrm{R},\mathsf{W}_\mathrm{R}) - \mathsf{C}_\mathrm{e}(\mathsf{U}_\mathrm{R},\mathsf{V}_\mathrm{I},\mathsf{W}_\mathrm{I}) - \mathsf{C}_\mathrm{e}(\mathsf{U}_\mathrm{I},\mathsf{V}_\mathrm{R},\mathsf{W}_\mathrm{I}) - \mathsf{C}_\mathrm{e}(\mathsf{U}_\mathrm{I},\mathsf{V}_\mathrm{I},\mathsf{W}_\mathrm{R})] \\ &\qquad + i\,[\mathsf{C}_\mathrm{e}(\mathsf{U}_\mathrm{R},\mathsf{V}_\mathrm{R},\mathsf{W}_\mathrm{I}) + \mathsf{C}_\mathrm{e}(\mathsf{U}_\mathrm{R},\mathsf{V}_\mathrm{I},\mathsf{W}_\mathrm{R}) + \mathsf{C}_\mathrm{e}(\mathsf{U}_\mathrm{I},\mathsf{V}_\mathrm{R},\mathsf{W}_\mathrm{R}) - \mathsf{C}_\mathrm{e}(\mathsf{U}_\mathrm{I},\mathsf{V}_\mathrm{I},\mathsf{W}_\mathrm{I})]\,.\end{aligned} \tag{3.40b}$$

Here, U_R, V_R, W_R and U_I, V_I, W_I are the real parts and the imaginary parts of U, V, and W. Moreover, in index notation, the components of $\mathsf{B}_\mathrm{e}(\mathsf{U},\mathsf{V})$ and $\mathsf{C}_\mathrm{e}(\mathsf{U},\mathsf{V},\mathsf{W})$ are given as

$$[\mathsf{B}_\mathrm{e}(\mathsf{U},\mathsf{V})]_j \coloneqq \sum_{l=1}^{6}\sum_{k=1}^{6}[\mathsf{B}_\mathrm{e}]_{jlk}\mathsf{U}_l\mathsf{V}_k \qquad j = 1,\ldots,6, \tag{3.41a}$$

$$[\mathsf{C}_\mathrm{e}(\mathsf{U},\mathsf{V},\mathsf{W})]_j \coloneqq \sum_{l=1}^{6}\sum_{k=1}^{6}\sum_{p=1}^{6}[\mathsf{C}_\mathrm{e}]_{jlkp}\mathsf{U}_l\mathsf{V}_k\mathsf{W}_p \qquad j = 1,\ldots,6, \tag{3.41b}$$

for all complex vectors $\mathsf{U},\mathsf{V},\mathsf{W} \in \mathbb{C}^6$.

To compute the Lyapunov coefficient, the complex vectors U, V, and W must be taken as indicated in Equation (3.38), in which case Equations (3.40a) and (3.40b) reduce to [39, Page 598]

$$\mathsf{B}_\mathrm{e}(\mathsf{u},\mathsf{u}) = [\mathsf{B}_\mathrm{e}(\mathsf{u}_\mathrm{R},\mathsf{u}_\mathrm{R}) - \mathsf{B}_\mathrm{e}(\mathsf{u}_\mathrm{I},\mathsf{u}_\mathrm{I})] + i2\mathsf{B}_\mathrm{e}(\mathsf{u}_\mathrm{R},\mathsf{u}_\mathrm{I}), \tag{3.42a}$$

$$\mathsf{B}_\mathrm{e}(\mathsf{u},\bar{\mathsf{u}}) = \mathsf{B}_\mathrm{e}(\mathsf{u}_\mathrm{R},\mathsf{u}_\mathrm{R}) + \mathsf{B}_\mathrm{e}(\mathsf{u}_\mathrm{I},\mathsf{u}_\mathrm{I}), \tag{3.42b}$$

$$\mathsf{C}_\mathrm{e}(\mathsf{u},\mathsf{u},\bar{\mathsf{u}}) = [\mathsf{C}_\mathrm{e}(\mathsf{u}_\mathrm{R},\mathsf{u}_\mathrm{R},\mathsf{u}_\mathrm{R}) + \mathsf{C}_\mathrm{e}(\mathsf{u}_\mathrm{R},\mathsf{u}_\mathrm{I},\mathsf{u}_\mathrm{I})] + i\,[\mathsf{C}_\mathrm{e}(\mathsf{u}_\mathrm{R},\mathsf{u}_\mathrm{R},\mathsf{u}_\mathrm{I}) + \mathsf{C}_\mathrm{e}(\mathsf{u}_\mathrm{I},\mathsf{u}_\mathrm{I},\mathsf{u}_\mathrm{I})]\,. \tag{3.42c}$$

3.4 Post-critical behavior: formation of stable limit cycles and self-resonance

As shown in the last section, the structure under consideration undergoes a Hopf bifurcation when the dead load, $\tilde{F}$, matches the critical load of flutter $\tilde{F}_\mathrm{flu}(\tilde{c})$ for a fixed value of $\tilde{c} > 0$.

To provide a more insightful picture of the dynamics governing this system, we employ the Schur's complement method [1, 35] seen in section 3.3.1. Equations (3.22a)–(3.22e) are placed into state formalism, and the well posed Cauchy problem is solved in MATLAB using the package `Ode45` to simulate the dynamics of the system. The simulations unless stated otherwise are carried out with the introduction of a small perturbation within the angles, θ_1 and θ_2, from the equilibrium ($\mathsf{q} = \mathsf{q}_\mathrm{e} + [0, 0.1, 0.1]$). In turn, the fluttering behavior of the structure can be witnessed, and the interplay between the two subsystems revealed.

One main feature within this system, as we will show, is that of *self-induced resonance*. The occurrence of which, is influenced by the ratio of the masses between the cart and the plate, and also the visco-elastic spring which grounds the plate. The resonant effects are felt within the system, when the natural frequency of the oscillations of the fluttering device, $\mathrm{Im}(\omega_{3,4})$, falls close to, or is an integer multiple of that of the natural frequency of the plate, $\tilde{\omega}_\mathrm{pc}$.

With this in mind, this study focuses on the role played by the parameters $\tilde{m}_\mathrm{c}$, $\tilde{m}_\mathrm{p}$, $\tilde{k}_\mathrm{p}$, while keeping the others fixed. From here we separate two main cases which govern the resonant dynamics of the system.

3.4.1 Case 1: $\tilde{m}_\mathrm{c}/\tilde{m}_\mathrm{p} = 1/3$

We consider now the case in which the mass ratio between the cart and plate to be small, more specifically 1/3. Within the setting, the mass of the plate is three times that of the cart. The resonant effects are investigated by performing a parameter sweep for varying $\tilde{k}_p$, whilst the other parameters remain fixed. Introducing $\tilde{\mathcal{P}}$ to be the collection of the dimensionless parameters, this study is shown in Figure 3.2, where the parameter values are fixed as follows,

$$\tilde{\mathcal{P}} := \{\tilde{m}_\mathrm{c}, \tilde{m}_\mathrm{p}, \tilde{k}_\mathrm{p}, \tilde{c}_\mathrm{r}, \tilde{c}_\mathrm{p}, \tilde{F}\} = \{10,\ 30,\ \tilde{k}_\mathrm{p},\ 0.1,\ 1,\ 1.1 \times \tilde{F}_\mathrm{flu}\}. \tag{3.43}$$

In Figure 3.2, the leftmost diagram shows the maximum and minimum amplitudes of the angles θ_1 and θ_2, together with the evaluation of the First Lyapunov Coefficient (see section 3.3.4) for sweeping $\tilde{k}_\mathrm{p}$. Note that, the expression for the First Lyapunov Coefficient is multiplied by 5, this is done for increased readability as its sign is the defining attribute. Also highlighted within the figure are the $1:2$, and the $1:4$, resonant points for the frequencies $\mathsf{Im}(\omega_{3,4})$ and $\tilde{\omega}_\mathrm{pc}$. Focusing on the plot of the First Lyapunov Coefficient, it remains *negative* for all values of $\tilde{k}_\mathrm{p}$ indicating that at the critical point $\tilde{F}_\mathrm{flu}$, the structure always undergoes a supercritical Hopf bifurcation, resulting in *stable* fluttering behavior. Indeed, the right hand side of figure reveals the phase portraits of θ_1 and θ_2, for the last 20% of the simulated time. These show the convergence of the phase portraits to a single limit cycle for each value of $\tilde{k}_\mathrm{p}$, thus confirming that the dynamic instability arises from a supercritical Hopf bifurcation, marking the onset of flutter.

One of the more noticeable features of these diagrams is the asymptote at the $1:2$ resonant point within the First Lyapunov plot. This is the first indication of the self resonant effects within this structure, whereby before the asymptote we observe a steady growth in the amplitude and a change in topology of the limit cycles due to the interaction of the fluttering pendulum and the plate. Subsequently, at this point, we observe both the maximum amplitude of the limit cycles and just after a sudden 'rebirth' of limit cycles, which then maintain a more constant amplitude. This behavior remains steady until the $1:4$ resonant point is reached. Here there is now a small collapse in the amplitude of the limit cycles and a second 'rebirth' is experienced, which, no longer is coincident with

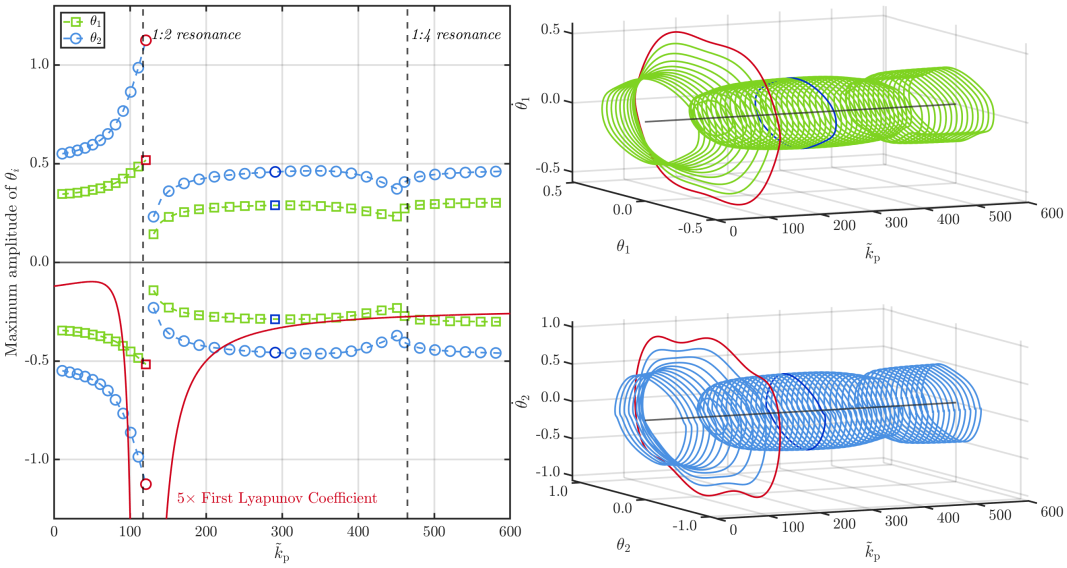

Figure 3.2: For the ratio of the masses $\tilde{m}_c/\tilde{m}_p = 1/3$, on the left, the maximum amplitudes of θ_1 and θ_2 are plotted alongside the First Lyapunov Coefficient. This is done for a sweep of $\tilde{k}_p$ values in the range of $[0, 600]$, by which the changes in the dynamic behavior of the structure can occur. On the right we show the phase plots of θ_1 and θ_2 for the final 20% of the simulation time. These highlight a self induced resonant phenomenon and the convergence of the limit cycles to a single trajectory for all values of $\tilde{k}_p$. Shown in all of the figures are 2 selected simulations, one red at $\tilde{k}_p = 120$, and one dark blue at $\tilde{k}_p = 290$, to investigate the self induced resonant effects

a detectable change in the curve of the First Lyapunov Coefficient. We note that, for ever increasing $\tilde{k}_p$, there are some cases where the $1:6$ resonance can be felt in the system but remains minimal. Further to this, for very large values of $\tilde{k}_p$, the results for Cazzoli et al. [5] are returned as to be expected.

Figure 3.3 contrasts the dynamics of the structure at the $1:2$ resonant point, shown in red at the point $\tilde{k}_p = 120$, and one which is away from resonance, shown in dark blue at the point $\tilde{k}_p = 290$. It can be seen that the average horizontal displacement of the cart at resonance is far greater than that when not at resonance (Figure 3.3a), leading to the double pendulum device encroaching along the plate at a faster rate, also with much smoother small scale oscillations. Furthermore, the amplitude of the vibrations experienced by the plate at resonance is almost $10\times$ than that away from resonance (Figure 3.3a). The change in morphology of the limit cycles is also evident as well as their apparent size (Figures 3.3e and 3.3f).

3.4.2 Case 2: $\tilde{m}_c/\tilde{m}_p = 3$

In contrast to the previous case, we now consider the mass ratio between the cart and plate to be large, more specifically 3. Within the setting, the mass of the cart is now three times that of the plate. The resonant effects are investigated by performing the same parameter sweep for varying $\tilde{k}_p$, where the parameter values are fixed as follows,

$$\tilde{\mathcal{P}} = \{30,\ 10,\ \tilde{k}_p,\ 0.1,\ 1,\ 1.1 \times \tilde{F}_{\text{flu}}\}. \tag{3.44}$$

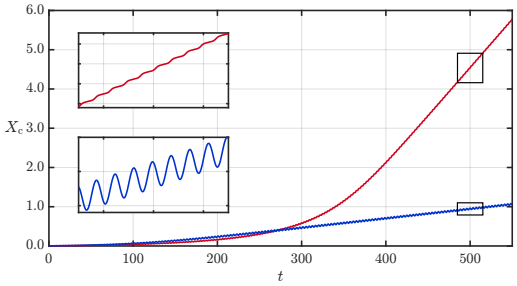

(a) Cart trajectories for $k_p = 120$ (red) and $k_p = 290$ (dark blue)

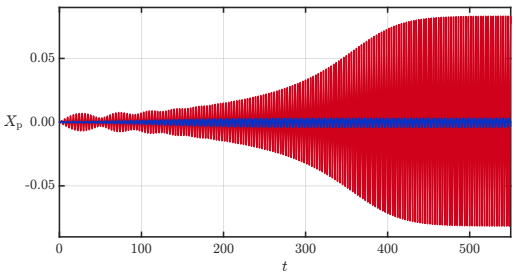

(b) Amplitude of the plate vibrations for $k_p = 120$ (red) and $k_p = 290$ (dark blue)

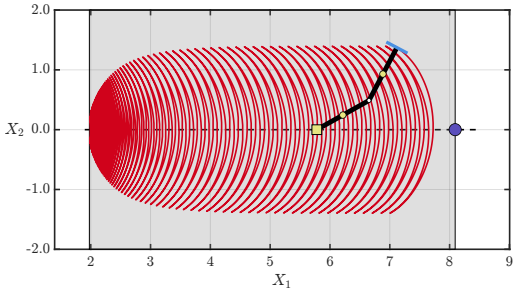

(c) Trajectory of the point D showing the carts motion for $k_p = 120$

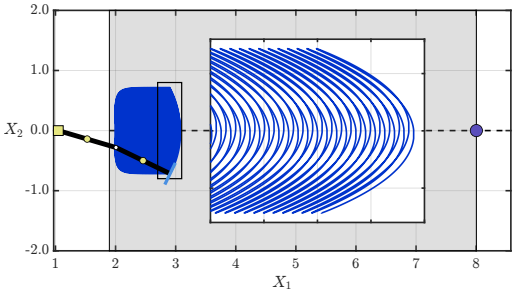

(d) Trajectory of the point D showing the carts motion for $k_p = 290$

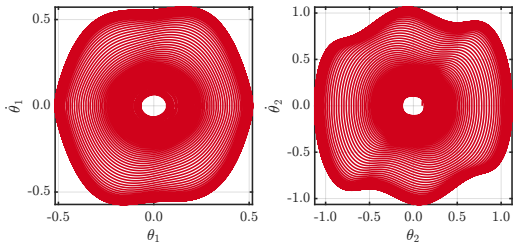

(e) Phase plots of the angles θ_1 and θ_2 for $k_p = 120$

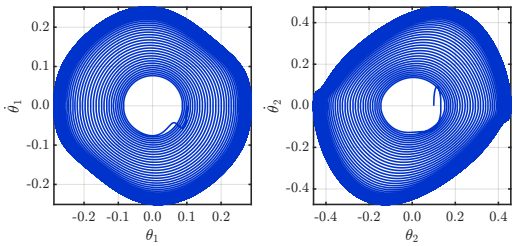

(f) Phase plots of the angles θ_1 and θ_2 for $k_p = 290$

Figure 3.3: selected simulations to show the self induce resonance, one red at $k_p = 120$ and one dark blue at $k_p = 290$.

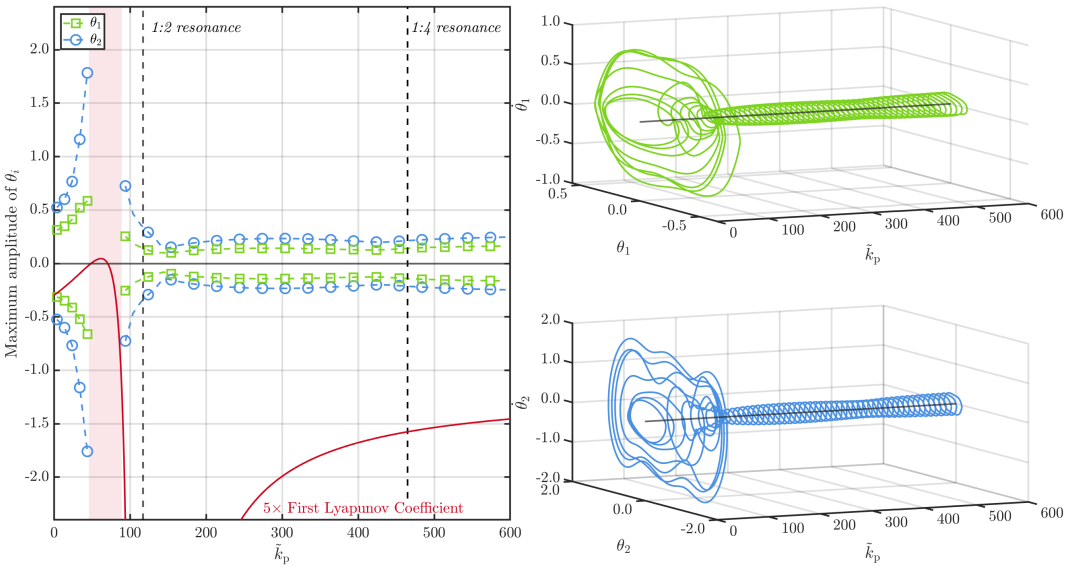

Figure 3.4: For the ratio of the masses $\tilde{m}_\mathrm{c}/\tilde{m}_\mathrm{p} = 3$, on the left, the maximum amplitudes of θ_1 and θ_2 are plotted alongside the First Lyapunov Coefficient. These are done for a sweep of $\tilde{k}_p$ values in the range of $[0, 600]$, by which the changes in behavior of the structure can occur. The red band highlights a subcritical bubble in which the type of Hopf bifurcation experienced by the system changes. Consequently the simulations in this region exhibit behavior which is focused on in a latter part of the study and for now they are omitted. On the right we show the phase plots of θ_1 and θ_2 for the final 20% of the simulation time. These highlight for the most part the convergence of the limit cycles to a single trajectory, however there are now some very evident self-induced resonant interactions present, shown by the phase plots close to the red band.

Similarly to the previous case, Figure 3.4 reveals a some resonant interplay at the $1:2$ and $1:4$ resonant points. This being a very muted collapse and rebirth of the limit cycles at a given $\tilde{k}_{\mathrm{p}}$, with the amplitudes of the resulting limit cycles to be approximately halved in comparison. The more prominent feature of this case is that the growth in the amplitude of the limit cycles shifts away from the $1:2$ resonant point, and more to the $1:1$ resonant point. The amplitudes exhibit a more extreme growth and lead to a region where the First Lyapunov Coefficient changes in its sign. In turn, the system at the critical point of flutter, $\tilde{F}_{\mathrm{flu}}$, no longer undergoes a supercritical Hopf bifurcation, but a subcritical Hopf bifurcation. The nature of the subcritical Hopf bifurcation leads to a *hard loss in stability* [65, 66]. As a consequence of this hard loss in stability, the solutions are divergent, and we see a violation of the configuration space within the simulations. The red band in Figure 3.4 highlights the region in which we see divergent behavior. Upon leaving this subcritical bubble, the First Lyapunov Coefficient sharply enters its asymptote, and we regain stable limit cycles from this point on.

3.4.3 Supercritical vs Subcritical: a more in depth investigation into the self-induced resonant effects.

In both of the aforementioned cases, self induced resonant effects are observed. Within the first case, the effects amount to an increase in the amplitudes of oscillations for θ_1 and θ_2 just before the $1:2$ resonant point. This behavior also changes the topology of the limit cycles produced, but within this regime the Hopf bifurcation remains supercritical. As well as expanding on the effects of the self induced resonance, we now focus on the latter case, and the behavior surrounding what we deem the subcritical bubble.

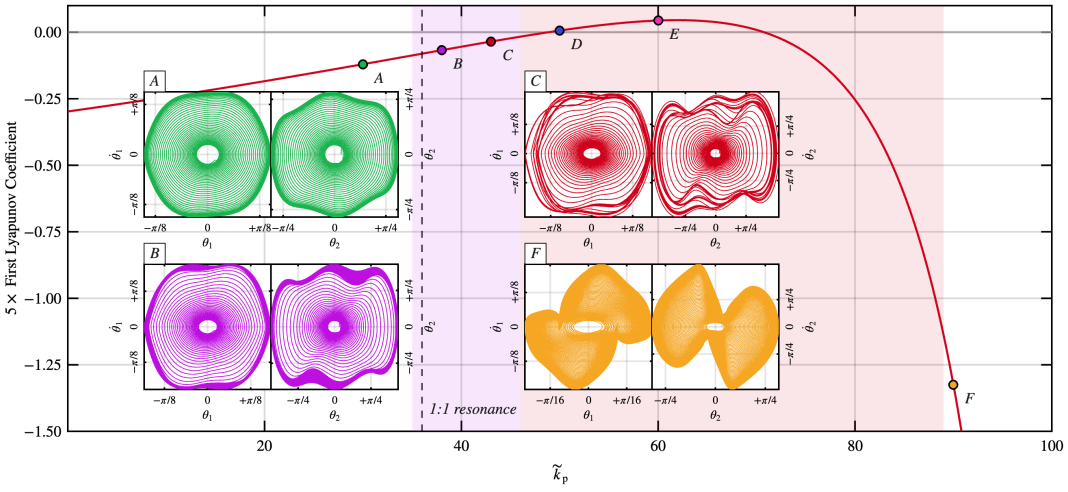

Figure 3.5: A zoomed in section of the Lyapunov curve surrounding the subcritical bubble at the $1:1$ resonant point. Along the curve, labeled in alphabetical order, are the selected simulations which show the behavior passing through this point region. Also highlighted are the limit cycles for the selected points A, B, C and F.

In Figure 3.5, the zoomed in section surrounding this subcritical bubble is presented, also shown are four chosen simulations which highlight the dynamics of the system around this area, with the points D and E to be commented on in the next section. Point A (green) exhibits a topology change of the limit cycle; however, in the context of dynamical

systems these limit cycles converge to a single trajectory and thus remain stable. Point B (purple) shows the initial effects of self resonance, resulting in limit cycles which are not to be considered stable but bound within a given region. Point C (red) sees the banding disappear, where the limit cycles formed converge but now with a winding number greater than one. It is worth noting that amplitude of this limit cycle is almost double that of the one shown at point A. Point F (orange) displays again convergent and stable limit cycles with no additional winding, however there is now an additional, significant change in its topology. These four points show a deterioration within stability of the limit cycles as the subcritical bubble is approached, then a re-emergence of stable limit cycles on the other side of the bubble with now an extreme change in their topologies. Within the background of the figure we highlight the areas in purple where we see the deterioration of the limit cycles, and in red the zone in which we see more divergent behavior. Complementary to Figure 3.5, for each of the cases, A, B, C and F, we show in Figure 3.6 the depictions of the paths that the nonholonomic constraint takes on the plate, and in Figure 3.7 the motion of the cart and the vibrational response of the plate. Similar to the limit cycles, in Figure 3.6 we see a deterioration in the path scribed by the non holonomic constraint. Point A (green) shows a clear and periodic pattern with sharp edges. Point B (purple) has a transient phase where we see some regular behavior, but as time increases, the irregularities in the path appear which is concurrent with the banding in the limit cycles. Point C (red) has a very small transient period, then the formation of a quasi periodic pattern with the sharp edges. Finally, point F (orange) sees the return of the periodic pattern, however the sharp edges are now replaced with knots. This knotting appears as the plate pulls as much on the device as it pushes. The follower force on the pendulum as a result is periodically changing in magnitude and sign, so the device is as much under compression as it is in tension. In Figure 3.7, the fact that all these points surround the subcritical bubble (are close to resonance), we see that the cart advances quickly, with subdued micro oscillations, and the plate vibrations to be amplified when compared to a case away from resonance. However, these effects are magnified in points B and C as they lie in positions closer to the subcritical bubble.

Within all of these simulations, the First Lyapunov coefficient remains negative, indicative of a supercritical Hopf bifurcation. Whilst this remains true for the simulations on the extremes, the inner simulations (Points B and C) when examined more closely appear to undergo subcritical Hopf bifurcation. This behavior is highlighted more clearly in Figure 3.8.

With reference to the colors which match those within the zoomed in plot of Figure 3.5, the maximum and minimum amplitudes of the limit cycles were plotted for an increasing force, which has been normalized by the critical load of flutter. In this manner, when $\tilde{F}/\tilde{F}_{\text{flu}} = 1$, a Hopf bifurcation occurs, and for larger values we are in the fluttering regime. Further to this, and defining the initial perturbation to be $\mathsf{q} = \mathsf{q}_{\text{e}} + [0, \delta\theta_1, \delta\theta_2]$, the left hand block of simulations were carried out for a value of $\delta\theta_1 = \delta\theta_2 = 0.1$ and the right hand block with $\delta\theta_1 = \delta\theta_2 = 0.4$.

Focusing first on the Left had side where the initial perturbation of the angles is $\delta\theta_i = 0.1, i = 1, 2$. The green and orange limit cycles (points A and F) representative of stable limit cycles, show *supercritical Hopf bifurcation*, and pass through the critical point of flutter with what can be described as a *soft loss of stability* [65]. This occurs when the bifurcation passes through its critical point, inducing a loss of stability in the equilibrium of the system. However, even when the system is unstable, it will remain near to its equilibrium birthing small amplitude limit cycles. When the bifurcation parameter is further increased, the amplitude of these limit cycles also increase, leading to a parabola-like growth in this amplitude.

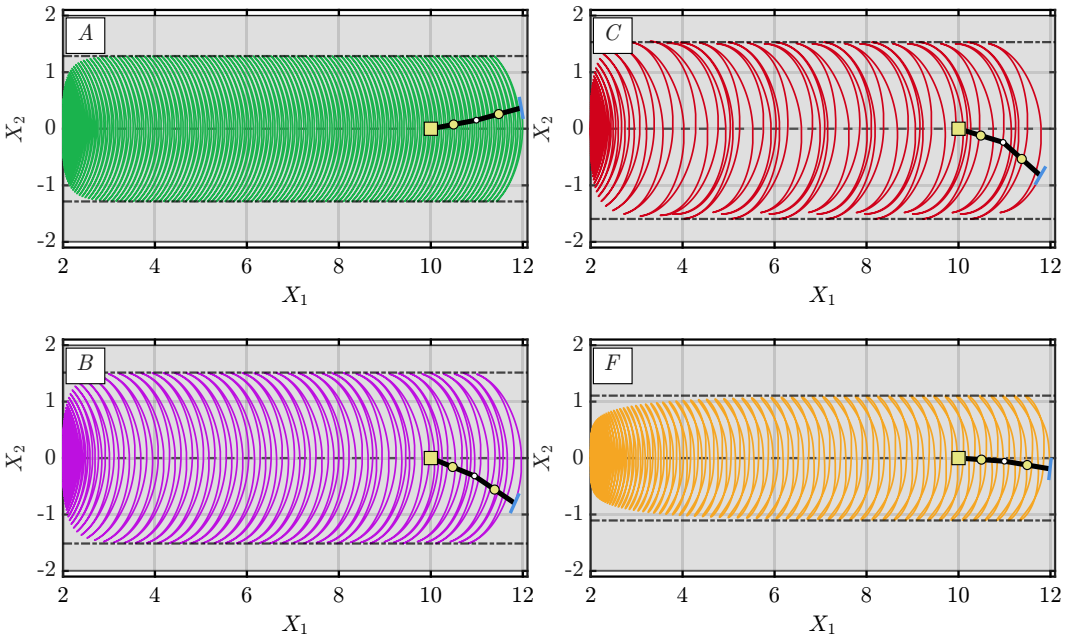

Figure 3.6: Device trajectory and trace of the pendulum tip for the points A,B,C and F.

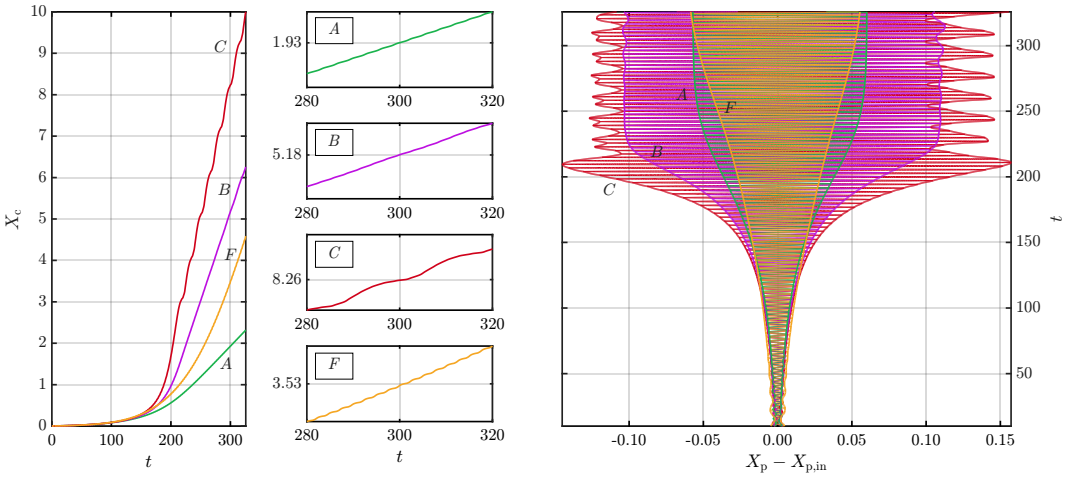

Figure 3.7: For points A, B, C, and F, the average motion of the cart is displayed on the left, together with magnified sections within the dimensionless time window $t = [280, 320]$. The corresponding plate vibrations for each case are shown on the right.

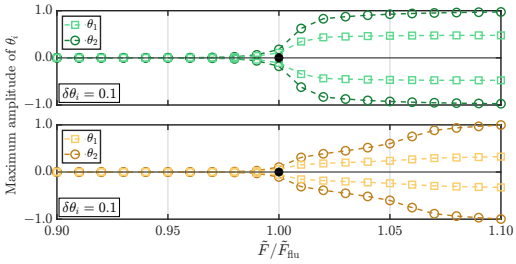

(a) Maximum and minimum amplitudes of the angles θ_1 and θ_2 for the points A and F, as the force passes through the critical point of flutter F_{flu}. The angles in this case have an initial perturbation of $\delta\theta_i = 0.1$.

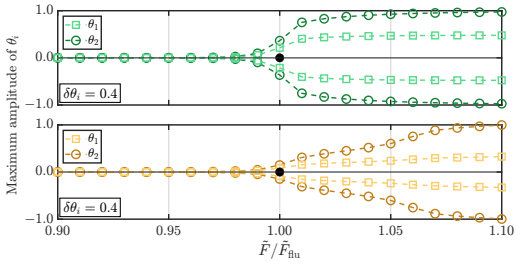

(b) Maximum and minimum amplitudes of the angles θ_1 and θ_2 for the points A and F, as the force passes through the critical point of flutter F_{flu}. The angles in this case have an initial perturbation of $\delta\theta_i = 0.4$.

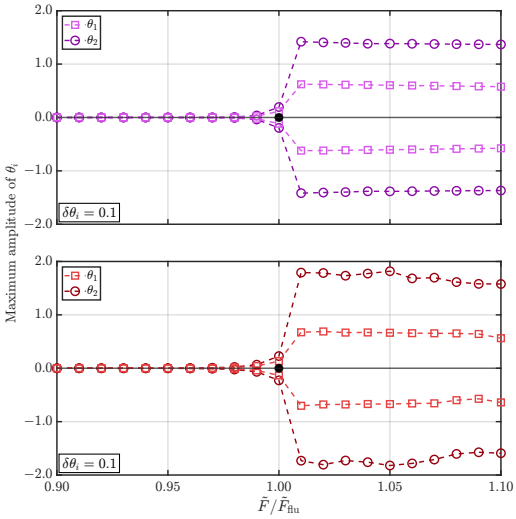

(c) Maximum and minimum amplitudes of the angles θ_1 and θ_2 for the points B and C, as the force passes through the critical point of flutter F_{flu}. The angles in this case have an initial perturbation of $\delta\theta_i = 0.1$.

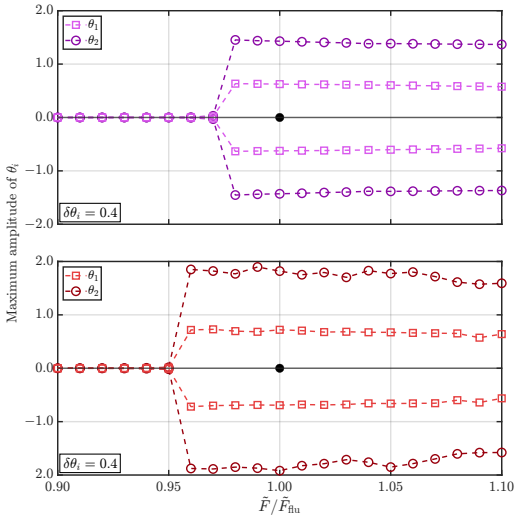

(d) Maximum and minimum amplitudes of the angles θ_1 and θ_2 for the points B and C, as the force passes through the critical point of flutter F_{flu}. The angles in this case have an initial perturbation of $\delta\theta_i = 0.4$.

Figure 3.8: Supercritical vs Subcritical Hopf bifurcation and the advanced loss of stability.

On the contrary, the purple and red (points B and C) limit cycles pass through this critical point with what is described as a *hard loss of stability* [65, 66]. This is typical of *subcritical Hopf bifurcation*, where there is a sudden, large jump following the crossing of this critical point. Here, neither the equilibrium or its neighborhood, remain attractive. One phenomenon this figure illustrates, and that is described in detail in Luongo et al. [66], is following a hard loss of stability, there can then be a *regain* of stability. This regain in stability gives rise to limit cycles of large amplitude, where its maximum and minimum is known as the *'jump amplitude'*. Indeed, contrasting the figures in green and orange, the critical point of flutter is surpassed with an immediate jump to large amplitude limit cycles, of size which is double than those enjoyed by supercritical Hopf bifurcation.

Focusing now on the right hand side where the initial perturbation of the angles is $\delta\theta_i = 0.4, i = 1, 2$. The increase in the perturbation has no effect on the supercritical Hopf bifurcation, however, in the subcritical case, we see that the hard loss of stability is induced before the bifurcation parameter reaches its critical point. This phenomenon is known in the literature as *advanced loss of stability* [65, 67]. The example shown in [67], references a weak noise which is always present in neurons, that is able to prematurely trigger the bifurcation. In our case, this weak noise is simulated by an increase in the perturbation from the equilibrium position, indeed triggering a premature loss in stability within the system. This is evidenced in Figure 3.8 (right), where the large amplitude limit cycles stemming from the hard loss in stability, are formed to the left of $\tilde{F}_{\text{flu}}$ when theoretically it is considered to be in its stable region.

3.4.4 A comment on chaos

Now we wish to comment on the weird and wonderful, to try and encompass the entire dynamic behavior of the device when passing through this post critical bubble. Focusing specifically on two different points within this post critical bubble labeled as points D and E (dark blue and pink). The first point we reference is at a value of $\tilde{k}_{\text{p}} = 50$ which is marked as Point D. This is highlighted in dark blue, where its dynamic motion and phase plots are seen in Figure 3.9a and Figure 3.9c. The device experiences an initial transitory phase where due to the resonant interplay the fluttering motion grows without bound. Highlighted in red, the device experiences a large and fast overshoot, shown clearly by its phase plots 3.9c, and for a brief moment the motion is rather chaotic. Shortly after however, the device recovers and enters a regime of quasi periodicity, where in this quasi periodic regime the limit cycles extracted exhibit both large amplitudes as well as heavy banding.

The second point we reference is at a value of $\tilde{k}_{\text{p}} = 60$ marked as Point E (pink), seen in Figure 3.9b with its phase plots shown in Figure 3.9d. We see again an initial transitory phase, with ever increasing fluttering motion due to the interplay between the two systems. However, after the overshoot, the device is no longer capable of recovery to some form of quasi periodic motion. Further to this, we see a breach of the point $\theta_1 = \pm\pi/2$ and $\theta_2 = \pm\pi/2$ in which $\hat{\mathsf{A}}(\mathsf{q})$ has null rank. This can call into question the validity of the results of this simulation due to the fact that the configurational space is violated. Nevertheless, this motion leads to the chaotic and sharp looking phase plots seen in Figure 3.9d.

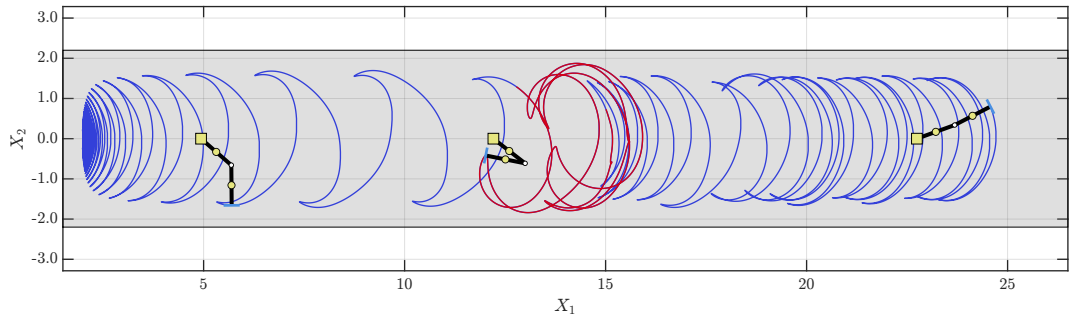

(a) The path that the nonholonomic constraint traces along the plate from left to right for $\tilde{k}_\mathrm{p} = 50$. Also shown are some selected configurations of the double pendulum as it traces this path.

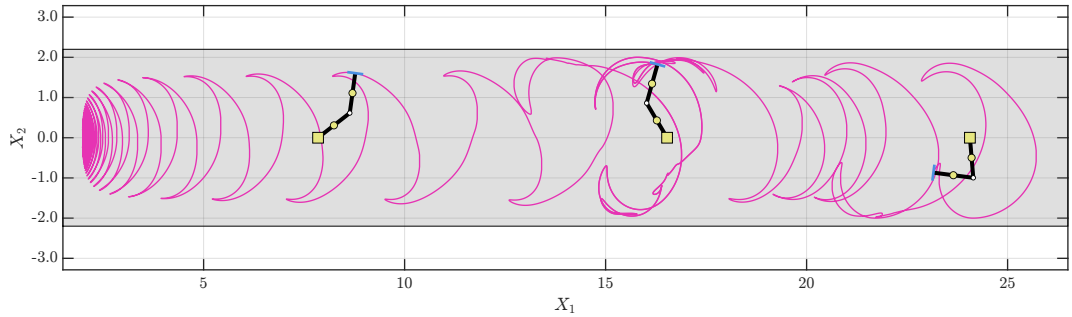

(b) The path that the nonholonomic constraint traces along the plate from left to right for $\tilde{k}_\mathrm{p} = 60$. Also shown are some selected configurations of the double pendulum as it traces this path.

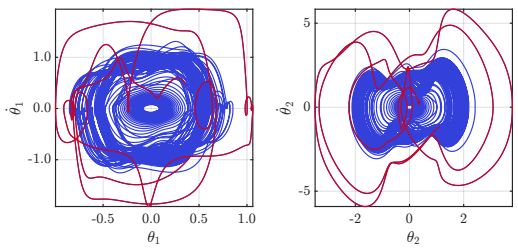

(c) Phase portraits of θ_1 and θ_2 for for $\tilde{k}_\mathrm{p} = 50$

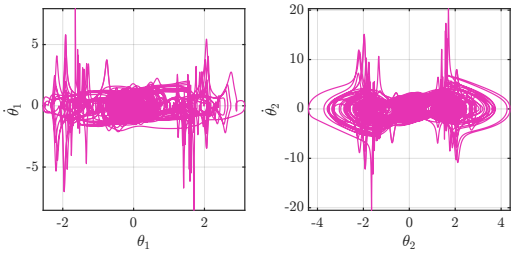

(d) Phase portraits of θ_1 and θ_2 for for $\tilde{k}_\mathrm{p} = 60$

Figure 3.9: Simulations as seen in the supercritical bubble with $\tilde{k}_\mathrm{p} = 50$ (blue) and $\tilde{k}_\mathrm{p} = 60$ (pink).

3.5 Conclusions

In this work we have studied the flutter instability for a structure which is comprised by a double pendulum, attached to a moving cart which interacts with an oscillating plate through a nonholonomic 'skate' constraint prescribed at the tip of the double pendulum. This interaction can lead, in certain regimes of the parameters, either to results similar to those of classical Ziegler's pendulum [4] (see e.g. Cazzolli et al. [5]) or to results that significantly deviate from them. To the best of our understanding, the results of Section 3.4 suggest that when the mass of the plate is higher than that of the cart (in the dimensionless setting), the interaction between the double pendulum and the plate is stable, thus, the results by Cazzolli et al. [5] can be retrieved for most cases albeit with increase amplitudes. Instead, when the two masses are either comparable or the mass of the plate is smaller than that of the cart, the interaction between the plate and the double pendulum is stronger and can lead to phenomena of divergence induced by resonance in the sense specified in Section 3.4.

We now summarize the main results of our work:

- The Kinematics of the device (a double pendulum interacting with a moving plate) were formalized through a *constrained* form of the principle of virtual work (see Equations (3.17a)–(3.17e)). Subsequently, these were made dimensionless, and, The Shur complement technique was exploited in order to aid in the numerical computation of the kinematical equations and also to to aid with a dynamic condensation of the problem used in the latter part of the study.

- We investigated the stability of the structure around the equilibrium configuration q_{e} in Equation (3.24), in which we set $X_{\mathrm{c0}} = 0$ (recall that our system allows for a 1-parameter family of equilibrium configurations for X_{c0} varying continuously). This configuration corresponds to the double pendulum being horizontal and the spring of the plate being deformed in order to balance the imposed (dimensionless) dead load $\tilde{F}$. In this respect, there exists two critical values $\tilde{F}_{\mathrm{flu}}(\tilde{c})$ and $\tilde{F}_{\mathrm{div}}(\tilde{c})$, both dependent on the dimensionless damping coefficient $\tilde{c}$, which separate stable, fluttering and the divergent regimes of the linearized, decoupled double pendulum subsystem.

- Next, bringing the focus on the behavior surrounding the critical point of flutter $\tilde{F}_{\mathrm{flu}}(\tilde{c})$. The stability of this point is examined inline with methods outlined in the book by Kuznetsov [39]. This revealed that the system was able to maintain the classification of undergoing a Hopf bifurcation provided that $\tilde{c}_{\mathrm{p}} > 0$. Thus giving rise to flutter and the possibility of resonant interactions in the structure.

- Finally, we simulate the dynamic behavior of the device revealing these resonant interactions, showing that the stability of aforementioned the Hopf bifurcation can change due to this resonant phenomena. We also highlighted two apparent phenomena which appear in this structure, which are: a regain in stability, following a hard loss of stability due to a subcritical Hopf bifurcation, and an advanced loss of stability, where apparent 'noise' is able to induce the onset of flutter before the bifurcation parameter reaches its critical point.

Appendix A

Supplementary Material

The text and equations consolidating this supplementary material are taken from [2].

A.1 Linearized equations for the dynamics of the structure

In this appendix we perform the linearization about the pair $(q_\mathrm{e}; \mu_\mathrm{e})$ of the full system (3.22a)–(3.22e) via a perturbative approach. Although the procedure employed here is rather standard, we deem it important to show the linear decoupling that occurs between the double pendulum and the plate-and-cart subsystems in the characteristic equation (3.31).

Upon introducing a smallness parameter ε, small *perturbations* around the equilibrium configuration q_e are considered, together with the corresponding Lagrange multiplier $\mu_\mathrm{e} = \tilde{F}$. This is achieved by the introduction of the homotopies $\tilde{q}$ and $\tilde{\mu}$, which define the perturbed configuration and Lagrange multiplier $\tilde{q}(t, \varepsilon)$ and $\tilde{\mu}(t, \varepsilon)$, and are required to comply with the conditions $\tilde{q}(t, 0) = q_\mathrm{e}$ and $\tilde{\mu}(t, 0) = \mu_\mathrm{e}$. Furthermore, $\tilde{q}$ and $\tilde{\mu}$ are assumed to be at least C^2 functions of their arguments.

The first-order expansions of $\tilde{q}$ and $\tilde{\mu}$ around $\varepsilon = 0$ and for all t can be written as $\tilde{q}(t, \varepsilon) = q_\mathrm{e} + \eta(t)\varepsilon + o(\varepsilon)$ and $\tilde{\mu}(t, \varepsilon) = \mu_\mathrm{e} + \varrho(t)\varepsilon + o(\varepsilon)$, with $\varepsilon \to 0$, where $\eta(t) \coloneqq \partial_\varepsilon \tilde{q}(t, 0)$ and $\varrho(t) \coloneqq \partial_\varepsilon \tilde{\mu}(t, 0)$ represent the first-order perturbations of q_e and μ_e. In the following, we denote the components of η by x_c, ϑ_1, ϑ_2, and x_p. By substituting $\tilde{q}(t, \varepsilon)$ and $\tilde{\mu}(t, \varepsilon)$ into Equations (3.22a)–(3.22e), and dropping all terms of order higher than the first in ε, the linearized dynamic equations are obtained and can be rearranged as

$$(\tilde{m}_\mathrm{p} + \tilde{m}_\mathrm{c})\ddot{x}_\mathrm{p} + \tilde{c}_\mathrm{p}\dot{x}_\mathrm{p} + \tilde{k}_\mathrm{p} x_\mathrm{p} = 0, \tag{A.1a}$$

$$\varrho = -\tilde{m}_\mathrm{c}\ddot{x}_\mathrm{c}, \tag{A.1b}$$

$$\ddot{x}_\mathrm{c} = \ddot{x}_\mathrm{p}, \tag{A.1c}$$

$$\frac{5}{4}\ddot{\vartheta}_1 + \frac{1}{2}\ddot{\vartheta}_2 + \tilde{c}\,(2\dot{\vartheta}_1 - \dot{\vartheta}_2) + (2\vartheta_1 - \vartheta_2) - \tilde{F}\,(\vartheta_1 - \vartheta_2) = 0, \tag{A.1d}$$

$$\frac{1}{2}\ddot{\vartheta}_1 + \frac{1}{4}\ddot{\vartheta}_2 - \tilde{c}\,(\dot{\vartheta}_1 - \dot{\vartheta}_2) - (\vartheta_1 - \vartheta_2) = 0. \tag{A.1e}$$

In accordance with the factorization of the characteristic polynomial in (3.31), in the linearized dynamic equations (A.1a)–(A.1e) the translational degrees of freedom, represented by the perturbed quantities x_c and x_p, are completely decoupled from the rotational degrees

of freedom, represented by the perturbed angular functions ϑ_1 and ϑ_2. In fact, x_p, x_c, and ϱ can be computed analytically and turn out to be

$$x_\mathrm{p}(t) = \mathrm{e}^{-\delta_\mathrm{p} t}\{a_\mathrm{p}\cos(\tilde{\omega}_\mathrm{pc} t) + b_\mathrm{p}\sin(\tilde{\omega}_\mathrm{pc} t)\}, \tag{A.2a}$$

$$x_\mathrm{c}(t) = x_\mathrm{p}(t) - L = \mathrm{e}^{-\delta_\mathrm{p} t}\{a_\mathrm{p}\cos(\tilde{\omega}_\mathrm{pc} t) + b_\mathrm{p}\sin(\tilde{\omega}_\mathrm{pc} t)\} - L, \tag{A.2b}$$

$$\varrho(t) = \tilde{m}_\mathrm{c}(\tilde{\omega}_\mathrm{pc}^2 - \delta_\mathrm{p}^2)x_\mathrm{p}(t) - 2\tilde{m}_\mathrm{c}\delta_\mathrm{p}\,\tilde{\omega}_\mathrm{pc}\mathrm{e}^{-\delta_\mathrm{p} t}\{a_\mathrm{p}\sin(\tilde{\omega}_\mathrm{pc} t) - b_\mathrm{p}\cos(\tilde{\omega}_\mathrm{pc} t)\}, \tag{A.2c}$$

where L is the initial distance between Point A and and Point E (see Figure 3.1), a_p and b_p are real constants, to be determined by prescribing initial conditions for x_p.

Note that, although Equation (A.1c) would imply that x_c and x_p differ additively by an affine function of time, they can actually differ only by a constant. This is because linearizing the original form of the constraint requires the perturbations of the velocities of the cart and of the plate to be equal to each other at all times, $\dot{x}_\mathrm{c}(t) - \dot{x}_\mathrm{p}(t) = 0$.

A.2 Matrices and arrays for the dynamic condensation

The explicit matrices and arrays featuring in Equation (3.27) are given as follows:

$$\hat{\mathsf{M}}_\mathsf{r}(\mathsf{q}_\mathsf{r}) \coloneqq \begin{bmatrix} \frac{5}{4} - \frac{9}{4\tilde{m}_\mathrm{c}}\sin^2\theta_1 & \frac{1}{2}\cos(\theta_1-\theta_2) - \frac{3}{4\tilde{m}_\mathrm{c}}\sin\theta_1\sin\theta_2 & 0 \\ \frac{1}{2}\cos(\theta_1-\theta_2) - \frac{3}{4\tilde{m}_\mathrm{c}}\sin\theta_1\sin\theta_2 & \frac{1}{4} - \frac{1}{4\tilde{m}_\mathrm{c}}\sin^2\theta_2 & 0 \\ 0 & 0 & \tilde{m}_\mathrm{p} \end{bmatrix}, \tag{A.3a}$$

$$\hat{\mathsf{B}}_\mathsf{r}(\mathsf{q}_\mathsf{r}) \coloneqq \left[\frac{3}{2\tilde{m}_\mathrm{c}}\cos\theta_2\sin\theta_1 - \sin(\theta_1-\theta_2),\ \frac{1}{2\tilde{m}_\mathrm{c}}\cos\theta_2\sin\theta_2,\ -\cos\theta_2\right], \tag{A.3b}$$

$$\hat{\mathsf{A}}_\mathsf{r}(\mathsf{q}_\mathsf{r}) \coloneqq \left[-\frac{3}{2\tilde{m}_\mathrm{c}}\sin\theta_1 + \sec\theta_2\sin(\theta_1-\theta_2),\ -\frac{1}{2\tilde{m}_\mathrm{c}}\sin\theta_2,\ 1\right], \tag{A.3c}$$

$$\hat{\mathsf{C}}_\mathsf{r}(\mathsf{q}_\mathsf{r}) \coloneqq \left[-\frac{1}{\tilde{m}_\mathrm{c}}\cos\theta_2\right], \tag{A.3d}$$

$$\hat{\mathsf{b}}_{\mathsf{q}\,\mathsf{r}}(\mathsf{q}_\mathsf{r},\dot{\mathsf{q}}_\mathsf{r}) \coloneqq \left\{\begin{array}{c} -\frac{3}{2\tilde{m}_\mathrm{c}}\tilde{F}\sin\theta_1 + 2\tilde{c}(\dot{\theta}_1-\dot{\theta}_2) + 2\theta_1 - \theta_2 + \frac{1}{2}\dot{\theta}_2^2\sin(\theta_1-\theta_2) + \alpha_{1,1} + \alpha_{1,2} \\ -\frac{1}{2\tilde{m}_\mathrm{c}}\tilde{F}\sin\theta_2 - \tilde{c}(\dot{\theta}_1+\dot{\theta}_2) - \theta_1 + \theta_2 - \frac{1}{2}\dot{\theta}_1^2\sin(\theta_1-\theta_2) + \alpha_{2,1} + \alpha_{2,2} \\ \tilde{c}_\mathrm{p}\dot{X}_\mathrm{p} + \tilde{k}_\mathrm{p}(X_\mathrm{p} - X_0) \end{array}\right\}, \tag{A.3e}$$

$$\hat{\mathsf{b}}_{\mathsf{c}\,\mathsf{r}}(\mathsf{q}_\mathsf{r},\dot{\mathsf{q}}_\mathsf{r}) \coloneqq \left\{-\frac{F}{\tilde{m}_\mathrm{c}} + (1 - \frac{3}{2\tilde{m}_\mathrm{c}})\dot{\theta}_1^2\cos\theta_1 + \dot{\theta}_1^2\sin\theta_1\tan\theta_2 - \frac{1}{2\tilde{m}_\mathrm{c}}\dot{\theta}_2^2\cos\theta_2 - \dot{\theta}_1\dot{\theta}_2\cos\theta_1\sec^2\theta_2\right\}, \tag{A.3f}$$

where, for formatting purposes, we introduced the auxiliary matrix

$$\alpha \coloneqq \begin{bmatrix} -\frac{9}{4\tilde{m}_\mathrm{c}}\dot{\theta}_1^2\cos\theta_1\sin\theta_1, & -\frac{3}{4\tilde{m}_\mathrm{c}}\dot{\theta}_2^2\cos\theta_2\sin\theta_1 \\ -\frac{3}{4\tilde{m}_\mathrm{c}}\dot{\theta}_1^2\cos\theta_1\sin\theta_2, & -\frac{1}{4\tilde{m}_\mathrm{c}}\dot{\theta}_2^2\cos\theta_2\sin\theta_2 \end{bmatrix}, \tag{A.4}$$

It is important to notice that $\mathsf{M}_\mathsf{r} = \hat{\mathsf{M}}_\mathsf{r}(\mathsf{q}_\mathrm{r})$ is not a "true" mass matrix, although it is symmetric and plays the role of the counterpart of the mass matrix. Indeed, there exist values of the kinematic descriptors for which $\hat{\mathsf{M}}_\mathsf{r}(\mathsf{q}_\mathrm{r})$ is not positive definite and not invertible. Since $\hat{\mathsf{M}}_\mathsf{r}(\mathsf{q}_\mathrm{r})$ must be invertible for the applicability of the procedure followed in Section 3.3.1, these values introduce further restrictions to the admissible configuration space characterizing the present formulation. This would require, in general, a dedicated study. However, since

$\hat{\mathsf{M}}_{\mathsf{r}}(\mathsf{q}_{\mathrm{r}})$ never happens to be singular in our calculations, this study has been omitted here and the inverse of $\hat{\mathsf{M}}_{\mathsf{r}}(\mathsf{q}_{\mathrm{r}})$ is well defined for all the values attained by θ_1 and θ_2 in our simulations.

We also emphasize two major differences between Equation (3.27) and the classical saddle-point form obtained, although for another mechanical system, in Equation (53) of [35]. The first is that the $(2,2)$-block of the block-wise matrix on the left-hand side of Equation (3.27) is not null. Rather, it corresponds to the 1×1 matrix $\mathsf{C}_{\mathsf{r}} = \hat{\mathsf{C}}_{\mathsf{r}}(\mathsf{q}_{\mathsf{r}}) = [-(1/\tilde{m}_{\mathrm{c}} \cos\theta_2)]$, which cannot be null because the value θ_2 must be different from $\pi/2$ in the present framework (instead, the $(2,2)$-block in Equation (53) of [35] is the 1×1 null matrix). The second difference is that the $(1,2)$-block and $(2,1)$-block of the block-wise matrix on the left-hand side of Equation (3.27) are not one the transpose of the other, $[\hat{\mathsf{B}}_{\mathsf{r}}(\mathsf{q}_{\mathsf{r}})]^{\mathrm{T}} \neq \hat{\mathsf{A}}_{\mathsf{r}}(\mathsf{q}_{\mathsf{r}})$.

In spite of the aforementioned differences, the Schur complement technique can be used, with slight modifications, to switch from Equation (3.27) to Equations (3.28a) and (3.28b). We refer the reader to [35, 36] for further details.

Bibliography

[1] A. Pastore et al. "Dynamics of a Charged Ziegler's Double Pendulum under the Joint Action of a Follower Force and Lorentz Force". Submitted. 2026.

[2] J. C. Harrop et al. "Coupling between Flutter Instability and Resonance in a Viscoelastic Structure with a Nonholonomic Constraint". Manuscript to be submitted. 2026.

[3] R.C. Hibbeler and K.S.V. Sekar. *Mechanics of Materials*. Always learning. Pearson Education South Asia Pte Limited, 2013. ISBN: 9789810694364. URL: https://books.google.it/books?id=Vu12ngEACAAJ.

[4] H. Ziegler. *Principles of Structural Stability*. Lehr- und Handbücher der Ingenieurwissenschaften. Birkhäuser Basel, 1977. ISBN: 9780720404326.

[5] Alessandro Cazzolli, Francesco Dal Corso, and Davide Bigoni. "Non-holonomic constraints inducing flutter instability in structures under conservative loadings". In: *Journal of the Mechanics and Physics of Solids* 138 (2020), p. 103919. DOI: https://doi.org/10.1016/j.jmps.2020.103919.

[6] G Rousseaux, R Kofman, and O Minazzoli. "The Maxwell-Lodge effect: significance of electromagnetic potentials in the classical theory". In: *The European Physical Journal D* 49.2 (2008), pp. 249–256.

[7] Xiaochen Wang et al. "Flutter instability characteristics and mechanisms of Ziegler double pendulum with arbitrary masses, stiffness and damping". In: *Nonlinear Dynamics* 112 (2024), pp. 20771–20792. DOI: 10.1007/s11071-024-10124-w. URL: https://doi.org/10.1007/s11071-024-10124-w.

[8] Davide Bigoni. *Flutter from Friction in Solids and Structures*. July 2018, pp. 1–61. DOI: 10.1007/978-3-319-93722-9_1. URL: https://doi.org/10.1007/978-3-319-93722-9_1.

[9] J. Neimark and N.A. Fufaev. *Dynamics of Nonholonomic Systems*. Rhode Island: American Mathematical Society, 1972.

[10] Benjamin C. Kuo. *Automatic Control Systems*. 3rd. Prentice Hall, 1975.

[11] B. Sturmfels. *Solving Systems of Polynomial Equations*. Conference Board of the Mathematical Sciences Regional Confe. Conference Board of the Mathematical Sciences, 2002. ISBN: 9780821832516. URL: https://books.google.it/books?id=WUAjMQAACAAJ.

[12] J.J. Sylvester. "XXIII. A method of determining by mere inspection the derivatives from two equations of any degree". In: *The London, Edinburgh, and Dublin Philosophical Magazine and Journal of Science* 16.101 (1840), pp. 132–135. DOI: 10.1080/14786444008649995. URL: https://doi.org/10.1080/14786444008649995.

[13] Henry Woody. "Polynomial Resultants". In: 2016. URL: https://api.semanticscholar.org/CorpusID:32054310.

[14] O.N. Kirillov and F. Verhulst. "Paradoxes of dissipation-induced destabilization or who opened Whitney's umbrella?" In: *ZAMM - Journal of Applied Mathematics and Mechanics / Zeitschrift für Angewandte Mathematik und Mechanik* 90.6 (May 2010), pp. 462–488. ISSN: 1521-4001. DOI: 10.1002/zamm.200900315. URL: http://dx.doi.org/10.1002/zamm.200900315.

[15] Oleg Kirillov. *Nonconservative stability problems of modern physics*. Vol. 14. De Gruyter Studies in Mathematical Physics. June 2013, p. 429. DOI: 10.1515/9783110270433. URL: https://hal.science/hal-01119742.

[16] Reza Mazrooei-Sebdani and Elham Hakimi. "Nondegenerate Hamiltonian Hopf bifurcations in $\omega : 3 : 6$ resonance ($\omega = 1$ or 2)". In: *Regular and Chaotic Dynamics* 25.6 (2020), pp. 522–536. DOI: 10.1134/S1560354720060027.

[17] Jan-Cees van der Meer. *The Hamiltonian Hopf Bifurcation*. Vol. 1160. Lecture Notes in Mathematics. Berlin, Heidelberg: Springer-Verlag, 1985, p. 115. ISBN: 978-3-540-16037-3. DOI: 10.1007/BFb0080357.

[18] C. Lanczos. *The Variational Principles of Mechanics*. Dover Publications, Inc. New York, 1970.

[19] F. Gantmacher. *Lectures in Analytical Mechanics*. MIR Publishers, Moscow, 1975.

[20] L. A. Pars. *A Treatise on Analytical Dynamics*. Heinemann, London, 1965.

[21] B. Felsager. *Geometry, particles, and fields*. Springer, Heidelberg, 1998.

[22] Kurt Haller. "Quantum electrodynamics in the temporal gauge". In: *Phys. Rev. D* 36 (6 1987), pp. 1830–1838. DOI: 10.1103/PhysRevD.36.1830. URL: https://link.aps.org/doi/10.1103/PhysRevD.36.1830.

[23] Oliver Lodge. "On an Electrostatic Field produced by varying Magnetic Induction". In: *Proceedings of the Physical Society of London* 10 (1889), pp. 116–128. DOI: 10.1088/1478-7814/10/1/320.

[24] Davide Bigoni and Giovanni Noselli. "Experimental evidence of flutter and divergence instabilities induced by dry friction". In: *Journal of the Mechanics and Physics of Solids* 59.10 (2011), pp. 2208–2226. DOI: 10.1016/j.jmps.2011.05.007.

[25] Oleg N. Kirillov. *Structural optimization of the Ziegler's pendulum: singularities and exact optimal solutions*. 2010. arXiv: 1101.0246 [math.OC]. URL: https://arxiv.org/abs/1101.0246.

[26] Francesco D'Annibale, Giuseppe Rosi, and Angelo Luongo. "Controlling the Limit-Cycle of the Ziegler Column via a Tuned Piezoelectric Damper". In: *Mathematical Problems in Engineering* 2015 (Sept. 2015), pp. 1–9. DOI: 10.1155/2015/942859.

[27] F. Alouges et al. "Can magnetic multilayers propel artificial microswimmers mimicking sperm cells?" In: *Soft Robotics* 2.3 (2015), pp. 117–128.

[28] A. T. Brown and W. C. K. Poon. "Ionic effects in self-propelled Pt-coated Janus swimmers". In: *Physical Chemistry Chemical Physics* 16.6 (2014), pp. 2446–2458. DOI: 10.1039/C3CP51333J.

[29] Yoonho Kim et al. "Ferromagnetic soft continuum robots". In: *Nature* 573.7772 (2019), pp. 82–87. DOI: 10.1038/s41586-019-1494-2. URL: https://doi.org/10.1038/s41586-019-1494-2.

[30] Honglin Shen et al. “Magnetically driven microrobots: Recent progress and future development”. In: *Materials & Design* 227 (2023), p. 111735. ISSN: 0264-1275. DOI: https://doi.org/10.1016/j.matdes.2023.111735.

[31] L. Zhang, K. E. Peyer, and B. J. Nelson. “Artificial Bacterial Flagella: Fabrication and Magnetic Control”. In: *Nano Letters* 9.10 (2009), pp. 3663–3667. DOI: 10.1021/nl901844w.

[32] Rémi Dreyfus et al. “Microscopic artificial swimmers”. In: *Nature* 437.7060 (2005), pp. 862–865. DOI: 10.1038/nature04090. URL: https://doi.org/10.1038/nature04090.

[33] Florian Katzmeier and Friedrich C. Simmel. “Microrobots powered by concentration polarization electrophoresis (CPEP)”. In: *Nature Communications* 14.6247 (2023). DOI: 10.1038/s41467-023-41923-1.

[34] J.M. Maruskin et al. “A fiber bundle approach to the transpositional relations in nonholonomic mechanics”. In: *J. Nonlinear Sci.* 22 (2012), pp. 431–461. DOI: https://doi.org/10.1007/s00332-012-9144-3.

[35] Andrea Pastore, Alessandro Giammarini, and Alfio Grillo. “Reconciling Kozlov’s vakonomic method with the traditional non-holonomic method: solution of two benchmark problems”. In: *Acta mechanica* (Jan. 2024). DOI: 10.1007/s00707-023-03811-z. URL: https://doi.org/10.1007/s00707-023-03811-z.

[36] G. Zampieri. “Nonholonomic versus Vakonomic Dynamics”. In: *J. Differ. Equ.* 163 (2000). https://doi.org/10.1006/jdeq.1999.3727, pp. 335–347.

[37] A.G. Agúndez, D. García-Vallejo, and E. Freire. “Linear stability analysis of nonholonomic multibody systems”. In: *International journal of mechanical sciences* 198 (May 2021), p. 106392. DOI: 10.1016/j.ijmecsci.2021.106392. URL: https://doi.org/10.1016/j.ijmecsci.2021.106392.

[38] A. Grillo, A. Pastore, and S. Di Stefano. “An Approach to Growth Mechanics based on the Analytical Mechanics of Nonholonomic Systems”. In: *J. Elast.* 157.3 (2025). URL: https://doi.org/10.1007/s10659-024-10092-7.

[39] Yuri A. Kuznetsov. *Elements of Applied Bifurcation Theory*. 4th ed. Vol. 112. Applied Mathematical Sciences. Springer Cham, 2023. ISBN: 978-3-031-22007-4. DOI: 10.1007/978-3-031-22007-4.

[40] Ruomeng Xu and Qingsong Xu. “A Survey of Recent Developments in Magnetic Microrobots for Micro-/Nano-Manipulation”. In: *Micromachines* 15.4 (2024), p. 468. DOI: 10.3390/mi15040468.

[41] D. Bruce Montgomery. *Solenoid Magnet Design: The Magnetic and Mechanical Aspects of Resistive and Superconducting Systems*. New York: Wiley-Interscience, 1969.

[42] T. Xu et al. “Focusing of relativistic electron beams with permanent magnetic solenoid”. In: *Phys. Rev. Accel. Beams* 28 (8 Aug. 2025), p. 082401. DOI: 10.1103/phhz-fgnl. URL: https://link.aps.org/doi/10.1103/phhz-fgnl.

[43] S. Martel and et al. “MRI-based medical nanorobotics: the modulation of magnetic gradients for propulsion and navigation of ferromagnetic core nanocapsules”. In: *Applied Physics Letters* 90.11 (2007), p. 114105. DOI: 10.1063/1.2752992.

[44] The MathWorks, Inc. *MATLAB*. Version R2024b. MathWorks. Natick, Massachusetts, 2024. URL: https://www.mathworks.com.

[45] L. F. Shampine and M. W. Reichelt. "The MATLAB ODE Suite". In: *SIAM Journal on Scientific Computing* 18 (1 1997).

[46] Davide Bigoni. "Structures loaded with a force acting along a fixed straight line, or the "Reut's column problem"". In: *Journal of the Mechanics and Physics of Solids* 134 (2019), p. 103741. DOI: 10.1016/j.jmps.2019.103741.

[47] Davide Bigoni et al. "Flutter instability in solids and structures, with a view on biomechanics and metamaterials". In: *Proceedings of the Royal Society A: Mathematical, Physical and Engineering Sciences* 479.2279 (Nov. 2023), p. 20230523. ISSN: 1364-5021. DOI: 10.1098/rspa.2023.0523.

[48] Xian-Fang Li et al. "Resonant frequency and flutter instability of a nanocantilever with the surface effects". In: *Composite Structures* 153 (2016), pp. 645–653. ISSN: 0263-8223. DOI: https://doi.org/10.1016/j.compstruct.2016.06.065. URL: https://www.sciencedirect.com/science/article/pii/S0263822316310601.

[49] Mohammad Sadegh Nematollahi, Hossein Mohammadi, and Sajjad Taghvaei. "Fluttering and divergence instability of functionally graded viscoelastic nanotubes conveying fluid based on nonlocal strain gradient theory". In: *Chaos* 29.3 (2019), p. 033108. DOI: 10.1063/1.5057738.

[50] Yi-Bo Wang et al. "Flutter analysis of a rigid-flexible coupled composite space structure with momentum wheels under thermal load". In: *Aerospace Science and Technology* 148 (2024), p. 109114. ISSN: 1270-9638. DOI: https://doi.org/10.1016/j.ast.2024.109114. URL: https://www.sciencedirect.com/science/article/pii/S1270963824002475.

[51] Laith K. Abbas et al. "Static/dynamic edge movability effect on non-linear aerothermoelastic behavior of geometrically imperfect curved skin panel: Flutter and post-flutter analysis". English. In: *Journal of Applied Mechanics, Transactions ASME* 79.4 (May 2012). ISSN: 0021-8936. DOI: 10.1115/1.4005537.

[52] Zhe-Xi Lu et al. "Flutter Analysis of Space Solar Power Satellite Under Thermal Loading". In: *AIAA Journal* 60.9 (2022), pp. 5589–5599. DOI: 10.2514/1.J061450. eprint: https://doi.org/10.2514/1.J061450. URL: https://doi.org/10.2514/1.J061450.

[53] Ariel Surya Boiardi and Giovanni Noselli. "Minimal actuation and control of a soft hydrogel swimmer from flutter instability". In: *Journal of the Mechanics and Physics of Solids* 191 (Oct. 2024), p. 105753. ISSN: 0022-5096. DOI: 10.1016/j.jmps.2024.105753. URL: http://dx.doi.org/10.1016/j.jmps.2024.105753.

[54] Alessandro Cazzolli, Francesco Dal Corso, and Davide Bigoni. "Flutter Instability and Ziegler Destabilization Paradox for Elastic Rods Subject to Non-Holonomic Constraints". In: *Journal of Applied Mechanics* 88.3 (Dec. 2020). ISSN: 1528-9036. DOI: 10.1115/1.4047132. URL: http://dx.doi.org/10.1115/1.4047132.

[55] A. M. Bloch. *Nonholonomic Mechanics and Control*. Springer, New York, 2003.

[56] F. Gantmakher. *Lectures in Analytical Mechanics*. MIR Publishers, Moscow, 1975.

[57] M. R. Flannery. "d'Alembert–Lagrange analytical dynamics for nonholonomic systems". In: *J. Math. Phys.* 52 (2011). https://doi.org/10.1063/1.3559128, p. 032705.

[58] M. R. Flannery. "The elusive d'Alembert-Lagrange dynamics of nonholonomic systems". In: *Am. J. Phys.* 79.9 (2011). https://doi.org/10.1119/1.3563538, pp. 932–944.

[59] J. Llibre, R. Ramírez, and N. Sadovskaia. "Nonlinear Dyn." In: *A new approach to the vakonomic mechanics* 78 (2014). https://doi.org/10.1007/s11071-014-1554-3, pp. 2219–2247.

[60] M. Favretti. "Equivalence of Dynamics for Nonholonomic Systems with Transverse Constraints". In: *J. Dyn. Differ. Equ.* 10.4 (1998). https://doi.org/10.1023/A:1022667307485, pp. 511–536.

[61] Javier Bonet and Richard D. Wood. *Nonlinear continuum mechanics for finite element analysis*. Cambridge university press, 1997.

[62] A. Grillo and S. Di Stefano. "A formulation of volumetric growth as a mechanical problem subjected to non-holonomic and rheonomic constraint". In: *Mathematics and Mechanics of Solids* 28.10 (2023), pp. 2215–2241. DOI: 10.1177/10812865231152228.

[63] A. Grillo and S. Di Stefano. "Addendum to "A formulation of volumetric growth as a mechanical problem subjected to non-holonomic and rheonomic constraint"". In: *Mathematics and Mechanics of Solids* 29.1 (2024), pp. 62–70.

[64] A. Pastore, A. Grillo, and E. Fried. "Internal constraints and gauge relations in the theory of uniaxial nematic elastomers". In: *J Elast* (2025). DOI: (Underrevision).

[65] Eugene M. Izhikevich. *Dynamical Systems in Neuroscience: The Geometry of Excitability and Bursting*. The MIT Press, 2006. ISBN: 9780262276078. DOI: 10.7551/mitpress/2526.001.0001. URL: https://doi.org/10.7551/mitpress/2526.001.0001.

[66] Angelo Luongo, Francesco D'Annibale, and Manuel Ferretti. "Hard loss of stability of Ziegler's column with nonlinear damping". In: *Meccanica* 51.11 (2016), pp. 2647–2663. DOI: 10.1007/s11012-016-0471-6. URL: https://doi.org/10.1007/s11012-016-0471-6.

[67] M. A. Shishkova. "Investigation of a system of differential equations with a small parameter in the highest derivatives". Russian. In: *Dokl. Akad. Nauk SSSR* 209.3 (1973). English transl. in *Sov. Math. Dokl.* **14**, 483–487, pp. 576–579.

This thesis investigates the dynamics of structures subject to velocity-dependent restrictions, known as nonholonomic constraints. These are applied to elastic structures, and their nonlinear dynamics are studied within bifurcation and stability theory. The stability of Ziegler's double pendulum is first examined to highlight its interesting dynamic behavior and ability to exhibit flutter via a Hopf bifurcation.

The main contribution is the development of models based on a double pendulum subject to a non-holonomic constraint, forming a variant of the Ziegler's system.

The first investigation considers a charge concentrated at the tip of the pendulum, where the constraint is located, giving the ‘charged Ziegler's double pendulum’. Placed inside an ideal solenoid, the system experiences a Lorentz force due to the magnetic field. Stability analysis shows that a Hopf bifurcation persists, allowing for a post-critical study of the interaction between Lorentz and other forces. The case outside the solenoid is also shown, where the magnetic field is null and the Lorentz force arises from the electric field alone, known as the ‘Maxwell–Lodge effect’.

The second investigation studies the constrained pendulum coupled with an oscillator, modelled as a plate attached to an axial spring. Linear analysis again predicts a Hopf bifurcation. In the dynamic regime, the pendulum interacts with the plate, producing a self-induced resonance. When the Hopf frequency approaches the plate’s natural frequency, the limit-cycle amplitude and mean velocity diverge. Regions also arise where the bifurcation becomes subcritical, leading to limit cycles which no not converge or chaotic behavior.

These instability mechanisms are of practical importance: resonance between Hopf-induced oscillations and structural modes can severely reduce stability margins and promote fatigue. Conversely, the same mechanisms may be harnessed for controlled amplification and nonlinear sensing applications.

Joel Christoper Harrop